Spring 2014

Computational Solutions of the Forward and Adjoint Euler Equations with Application to Duct Aeroacoustics

Ibrahim Kocaogul
Old Dominion University

COMPUTATIONAL SOLUTIONS OF THE FORWARD AND ADJOINT EULER EQUATIONS WITH APPLICATION TO DUCT AEROACOUSTICS

by

Ibrahim Kocaogul
B.S. June 2002, Fatih University, Turkey
M.S. June 2005, Fatih University, Turkey

A Dissertation Submitted to the Faculty of
Old Dominion University in Partial Fulfillment of the
Requirements for the Degree of

DOCTOR OF PHILOSOPHY

COMPUTATIONAL AND APPLIED MATHEMATICS

OLD DOMINION UNIVERSITY
May 2014

Approved by:

Fang Q. Hu (Director)

Hideaki Kaneko (Member)

Ruhai Zhou (Member)

Miltiadis D. Kotinis (Member)

ABSTRACT

COMPUTATIONAL SOLUTIONS OF THE FORWARD AND ADJOINT EULER EQUATIONS WITH APPLICATION TO DUCT AEROACOUSTICS

Ibrahim Kocaogul
Old Dominion University, 2014
Director: Dr. Fang Q. Hu

Traditionally, the acoustic source terms are modeled by single frequency sinusoidal functions. In the present study, the acoustic sources are modeled by a broadband wave packet. Radiation of acoustic waves at all frequencies can be obtained by Time Domain Wave Packet (TDWP) method in a single time domain computation. The TDWP method is also particularly useful for computations in the ducted or waveguide environments where incident wave modes can be imposed cleanly without a potentially long transient period. Theoretical analysis as well as numerical validation are performed in this study. In addition, the adjoint equations for the linearized Euler equations in the time domain are formulated for the Cartesian coordinates. Analytical solution for adjoint equations is derived by using Green's function in 2D and 3D. The derivation of reciprocal relations is presented for closed and open ducts. The adjoint equations are then solved numerically in reversed time by the TDWP method. Reciprocity between the duct modes in the closed duct is derived and numerically validated. For the open duct, reciprocal relation between the duct mode amplitudes and far field point sources in the presence of the exhaust shear flow is derived and confirmed numerically. Applications of the adjoint problem to closed and open ducts are also presented.

ACKNOWLEDGMENTS

First, I would like to express my deeply-felt thanks to my advisor, Professor Fang Q. Hu; for his warm encouragement and thoughtful guidance. This work would not have been possible without his wisdom and patience. He has been supportive since the days I began working on this thesis. He has been there, in front of my eyes for almost four years, motivating and inspiring me to accomplish my goal. His invaluable contributions and suggestions allowed me to overcome many difficulties.

I would like to thank my committee members, Dr. Hideaki Kaneko, Dr. Ruhai Zhou, and Miltiadis Kotinis for taking the time to review my work and offering helpful suggestions and comments for improvement.

I would like to acknowledge all the teachers I learnt from since childhood, I would not have been here without their guidance and support. A special thank you goes to my parents, Idris and Fatma Kocaogul, and my sister, Fatmana Akyol, for always believing me. My warm appreciation is due to all friends in Old Dominion University.

I am also very grateful for the support from NSF grant DMS-0810946, NASA Coorperative Agreement NNX11AI63A, and the ODU Modeling & Simulation Scholarship.

Finally, I would like to express my eternal gratitude to my wife, Fatmana Citisli Kocaogul, for supporting me and all of the sacrifices that you have made on my behalf.

TABLE OF CONTENTS

Page

LIST OF FIGURES x

Chapter

1. INTRODUCTION 1

2. LINEARIZED EULER SYSTEM 5
   - 2.1 FORMULATION OF GOVERNING EQUATIONS 5
   - 2.2 DISPERSION RELATION 9

3. TIME DOMAIN WAVE PACKET METHOD 17
   - 3.1 DEFINITION OF TIME DOMAIN WAVE PACKET METHOD 17
   - 3.2 DUCT MODE IMPOSITION 19
   - 3.3 ANALYTICAL SOLUTION FOR DUCT MODE IMPOSITION 20
   - 3.4 APPLICATION OF THE TDWP METHOD TO UNIFORM DUCT . 25
   - 3.5 MODAL DECOMPOSITION 26
   - 3.6 ANALYSIS AND SUGGESTION FOR THE WIDTH OF THE SOURCE TERM IN (26) 35

4. ADJOINT SYSTEM 43
   - 4.1 DERIVATION AND FORMULATION 43
   - 4.2 EIGENVALUES AND EIGENFUNCTIONS OF THE ADJOINT SYSTEM AND DISPERSION RELATION FOR A UNIFORM MEAN FLOW 45
   - 4.3 ORTHOGONALITY OF EIGENFUNCTIONS 46
   - 4.4 NUMERICAL RESULTS OF THE ADJOINT SYSTEM 49

5. APPLICATION OF THE TDWP METHOD TO NON-UNIFORM DUCTS 52
   - 5.1 THE AREA-MACH NUMBER RELATION 52
   - 5.2 NON-UNIFORM DUCT AND ITS COMPUTATIONAL DOMAIN... 55
   - 5.3 NUMERICAL RESULTS FOR A 2-D NON-UNIFORM DUCT 59
   - 5.4 NUMERICAL RESULTS FOR A 3-D NON-UNIFORM DUCT 66

6. A DISCUSSION ON THE ACOUSTIC ENERGY AND ADJOINT SOLUTIONS 72

7. RECIPROCITY 77
   - 7.1 RECIPROCITY BETWEEN DUCT MODES 77
   - 7.2 NUMERICAL VALIDATION OF RECIPROCITY BETWEEN DUCT MODES 80
   - 7.3 RECIPROCITY BETWEEN A POINT SOURCE AND DUCT MODES 83

7.4 INITIAL CONDITION FOR THE ADJOINT SYSTEM 87
7.5 NUMERICAL RESULTS FOR 2-D OPEN DUCT 94

8. CONCLUSIONS 105

REFERENCES 107

VITA 111

LIST OF FIGURES

Figure Page

1. Flow through a volume V with surface $\partial V \equiv S$. 6

2. A uniform duct with uniform cross section. 11

3. For the symmetric eigenfunctions, the dispersion relation shows 4 cut-on radial modes at ω_f when $M = 0$. 15

4. For the symmetric eigenfunctions, the dispersion relation shows 5 cut-on radial modes at ω_f when $M = 0.45$. 15

5. For the anti-symmetric eigenfunctions, the dispersion relation shows 4 cut-on radial modes at ω_f when $M = 0$. 16

6. For the anti-symmetric eigenfunctions, the dispersion relation shows 5 cut-on radial modes at ω_f when $M = 0.45$. 16

7. Schematic for a time signal of a sinusoidal wave (left) and a wave packet (right). 17

8. Illustration of Broadland Acoustic Test Pulse time function $\Psi(t)$ and its spectrum $\Psi(\omega)$. 18

9. Schematic of the computational domain for a rectangular duct. 25

10. A time sequence of instantaneous pressure contours of an acoustic wave packet by the symmetric eigenfunctions on the xy slice at $z = 0$ for the uniform duct. 27

11. A time sequence of instantaneous pressure contours of an acoustic wave packet by the symmetric eigenfunctions on the xz slice at $y = 0$ for the uniform duct. 28

12. A time sequence of instantaneous pressure contours of an acoustic wave packet by the anti-symmetric eigenfunctions on the xy slice at $z = 0$ for the uniform duct. 29

13. A time sequence of instantaneous pressure contours of an acoustic wave packet by the anti-symmetric eigenfunctions on the xz slice at $y = 0$ for the uniform duct. 30

14. Pressure time history at (100,10,10) with $M = 0.45$. 31

15. A comparison between the analytic and numerical FFTs of a point at $(100, 0, 0)$ (top) and its scaled version with $\omega = [0, 1.4]$ (bottom)..... 32

16. FFT of the time signal shown in the Fig. 14 and cutoff frequency..... 33

17. Illustration of the right-going and left-going duct wave modes..... 34

18. The mode $(2, 1)$ and $M = 0$ by the symmetric eigenfunction..... 36

19. The mode $(2, 1)$ and $M = 0.45$ by the symmetric eigenfunction..... 36

20. The mode $(2, 1)$ and $M = 0$ by the anti-symmetric eigenfunction..... 37

21. The mode $(2, 1)$ and $M = 0.45$ by the anti-symmetric eigenfunction..... 37

22. Solutions at four different frequencies are decomposed into cut-on duct modes at selected x locations..... 40

23. Three functions vs. frequency, Top: The spectrum of the wave packet; Middle: A function; Bottom: An exponential function..... 41

24. A plot from the equation (41) for $k = 0.05$ showing the relation $b_0 \Delta x$ vs. $\omega \Delta t$..... 42

25. A duct with uniform cross section and a rectangular prism inside..... 46

26. Shematic of the rectangular computational domain for adjoint system..... 50

27. The mode $(2, 1)$ and $M = 0$ for the adjoint system..... 50

28. The mode $(2, 1)$ and $M = 0.45$ for the adjoint system..... 51

29. A varying area channel..... 53

30. Left: A maximum area and incoming flow with a Mach number M. Right: A minimum area that is called throat and incoming flow with a Mach number M..... 54

31. Two cross-sectional areas A and A^*..... 54

32. Schematic diagram of a non-uniform duct..... 55

33. Top: Physical domain of the non-uniform duct; Bottom: Uniform computational domain and mesh for time domain simulation and some of grid lines are shown..... 56

34. Shematic sketch of the non-uniform duct with the velocity, normal vectors at the boundaries, lengths and cross-section areas..... 58

35. A 2-D non-uniform duct showing a source function location (dotted-line) and PML regions (dashed-line). 60

36. Time domain pressure contours of the Euler solution at $t = 20, 100, 300, 500$. 61

37. Frequency domain pressure contours at $\omega = 3\pi/50, 4\pi/50, 6\pi/50$ by FFT of the time domain solution given in Fig. 36. 62

38. Forward problem solution at $\omega = 20\pi/250$ for the forced mode $(0, 2)$ and $M = 0$. 64

39. Forward problem solution at $\omega = 30\pi/250$ for the forced mode $(0, 2)$ and $M = 0.45$. 64

40. Adjoint problem solution at $\omega = 30\pi/250$ for the forced mode $(0, 2)$ and $M = 0$. 65

41. Adjoint problem solution at $\omega = 20\pi/250$ for the forced mode $(0, 2)$ and $M = 0.45$. 65

42. A 3-D non-uniform duct and a plane source. 66

43. A time sequence of instantaneous pressure contours of an acoustic wave packet on the xy slice at $z = 0$. 68

44. A time sequence of instantaneous pressure contours of an acoustic wave packet on the xz slice at $y = 0$. 69

45. A time sequence of instantaneous pressure contours of an acoustic wave packet on the yz slice at $x = 25$. 70

46. Forward problem solution at $\omega = \pi/5$ for the forced mode $(3, 2)$ and $M = 0.3$. 70

47. Adjoint problem solution at $\omega = \pi/5$ for the forced mode $(3, 2)$ and $M = 0.3$. 71

48. An outlined volume of a non-uniform duct. 74

49. Schematic diagram showing a non-uniform duct and incident, reflected and transmitted waves for forward and adjoint problems. 78

50. The normalized amplitudes of right-going modes along the duct for the forced mode $(2, 3)$ in the forward problem and "i" is the station number from 0 to 9. 81

51. The normalized amplitudes of left-going modes along the duct for the forced modes $(2,1),(2,2),(2,3),(2,4)$ in the adjoint problem and "i" is the station number from 0 to 9. 82

52. Demonstration of reciprocity (95). 83

53. Schematic diagrams showing the forward (top) and adjoint (bottom) problem. 84

54. A schematic diagram of outlined volume. 86

55. Pressure contours at time $t = 28$ of the adjoint solution and the source point at $(130, 70)$. 92

56. Pressure (top) and u-velocity (bottom) at time $t = 28$ of the adjoint solution. 93

57. Computational domain and mesh for the time domain solution with PML at all non-reflecting boundaries. 94

58. Schematic diagram of shear layers. 95

59. A function $F(y)$ as an example of the distribution function for the shear layer. 96

60. Mean axial velocity distribution inside and outside of the duct. 96

61. Computational domain for the Euler and the adjoint system. 97

62. An example of the connected domains. 98

63. Instantaneous pressure contours at $t = 500\Delta t, 1000\Delta t, 1500\Delta t, 2000\Delta t$. .. 101

64. Contours of pressure at four chosen moments of the adjoint solution for a broadband point source. 102

65. Frequency domain pressure contours of forward (top) and adjoint (bottom) at frequency $(\pi/5)$ by FFT of the time domain solutions given in Figs. 63 and 64. 103

66. Demonstration of reciprocity between point sources and their corresponding duct modes. 104

CHAPTER 1

INTRODUCTION

The equations which govern sound propagation in flows are complicated that analytic solutions exist only for special cases. Because of this, computational acoustics is a significant tool for realistic acoustic problems. In this approach, the acoustic waves are computed directly from the governing equations of the compressible flows, namely, the Navier-Stokes equations or their non-viscous counterpart, the Euler equations. The latter is a special instance of the former. In Computational Aeroacoustics (CAA), the linearized Euler equations is widely used to study acoustic noise generation and propagation [32, 2]. This set of equations supports the propagation of three type of waves: acoustic, vorticity and entropy waves [28].

The development of the turbofan engine led to a reduction in jet noise and increase in fan-compressor noise. In turbofan engines, the fan dominates the inlet-related noise. The fan is enclosed within a duct system. To predict the radiated noise and to minimize this noise, we must consider acoustic propagation and radiation in the duct and outside of the duct. Sound radiation depends both on the characteristics of the sound source and also on the geometry of the duct. Works on the radiation of sound from ducts goes back to Rayleigh [41]. A review of duct acoustics in [39] is extremely enlightening. The theory of sound propagation in straight ducts with boundary conditions and a homogeneous stationary medium is classical and well established [38, 40]. In [43, 42] the sound transmission is described in slowly varying ducts with mean flow. In this thesis, we consider a compressible inviscid perfect isentropic gas flow inside the ducts, and study acoustic perturbations on a mean flow.

In most time domain calculations in CAA, the acoustic sources are often modeled by a sinusoidal function in time with a specified frequency of interest. Recently, a Time Domain Wave Packet (TDWP) method has been developed for linear aeroacoustics computations [24]. In this thesis, the TDWP method will be applied and extended to equations for the closed and open ducts. This new method differs from the more conventional approach in that the source time function is modeled by a temporally compact broadband pulse. The acoustic sources, such as point sources or

incoming wave modes, are often specified as sinusoidal functions in time with a fixed frequency of interest in conventional time domain linear aeroacoustics computations. In the TDWP method, the propagation properties of linear waves of all frequencies are embedded in the propagation of the wave packet. Therefore, the time domain simulation carried out by TDWP produces the results for all the frequencies within the numerical resolution. In the frequency domain, while one conventional method of simulation gives the result for a single frequency, in the TDWP method, solutions at all frequencies can be obtained by FFT of the one time domain simulation. For the conventional time domain solutions, the simulations are required to carry out to reach a time periodic state. Sometimes, this is very expensive. On the other hand, in the Time Domain Wave Packet method the acoustic source is modeled as a wave packet with a relatively short time duration. The numerical simulation just needs to last until the wave packet has exited from the computational domain. That makes it more efficient than the conventional time domain approach.

Another advantage of the TDWP method is the suppression of hydrodynamic instability waves in acoustic computations. Since the acoustic waves travel at the speed of sound and instability waves travel at the convective speed of the mean flow [7, 8], and a wave packet is temporally compact, the Time Domain Wave Packet method benefits the separation of acoustic and instability waves in the shear flow. Therefore, it gives a chance to suppress the instability waves. The acoustic wave packet would propagate through the shear flow in a short time period and before the growth of the instability wave becomes significant. After the wave packet has propagated through the shear layers, the instability wave suppression techniques, such as the Mean Flow Gradient Removal technique [4] or the Source Filtering technique [29, 24], may be applied. Therefore, effects of this modification on the acoustic waves would be limited.

In this thesis, the Time Domain Wave Packet method is also extended to adjoint problems for the closed and open duct environments. Previously, adjoint systems for the linearized Navier-Stokes equations for incompressible flows have been studied [16, 45, 19]. The adjoint-based optimization has been used in several flow control and design applications [14]. In [47], the adjoint equations for linearized Euler equations has been given in the frequency domain for an investigation of jet noise radiations. The great savings in computation is realized by using the reciprocity relation and the adjoint solutions. Reciprocal relations in nonuniform ducts (closed duct) and

reciprocity relation in radiation problem (open duct) that is between duct radiating modes and the far-field sound are well established in [6] for cases where no mean flow is present. In many branches of mechanics, the reciprocity principle applies. However, the existence of a reciprocity principle has not been extensively studied in duct acoustics. Notable exceptions are the works of [10, 20]. Reciprocal relations in acoustical fields in general flows have been studied in [13, 15, 35, 34] and many others, in particular in connection with the study in acoustic energy fields. Since analytic solutions exist only for the very simple examples for sound propagation, there is interest in finding more properties of sound waves which helps in the comprehension of the solutions and offers a check over numerical solutions. Therefore, in finding a relation between energy, adjoint solution and reciprocity is of interest.

In this thesis, the adjoint system for the linearized Euler equations with a general non-uniform mean flow is derived in the time domain for the closed and open ducts. Here some advantages afforded by the adjoint problem are considered. Due to reciprocity between Euler equations and adjoint system, solutions of the adjoint problem help to validate computational solutions of the Euler (forward) problem. There are also advantages for the open duct computations. In a forward problem, usually the duct propagating modes are defined as the acoustic source inside the duct and the radiated sound at the observation points in the far-field is computed. In the adjoint problem, instead, a source can be placed at the far-field, representing the receiver/microphone, and the waves propagated into the duct from the far-filed source is computed. The source point of the adjoint problem at the far-field is the same as an observation point of the forward problem. In this thesis, a reciprocity between the forward and adjoint problems is derived. When the number of observation points is smaller than the number of possible propagating duct modes, using the adjoint solution is more efficient. It will be demonstrated that combined with the Time Domain Wave Packet method, relative strengths of all duct modes of all frequencies to the acoustic pressure at a particular far-field location can be determined in a single time domain computation by the adjoint system. Moreover, due to reciprocity , solutions of the adjoint problem can serve to validate those of the forward problem.

The rest of the thesis is organized as follows. In Chapter 2, the linearized Euler equations are introduced in the Cartesian coordinates and then defined in the matrix form. Essential information about the dispersion relation will be discussed to understand the propagation characteristics of the acoustic waves. The Time Domain

Wave packet method and its extension to duct acoustics will be discussed in Chapter 3. The adjoint system for the linearized Euler equations with a general mean flow is derived and formulated in the time domain and orthogonality of eigenfunctions are presented in Chapter 4. Applications of Euler equations and adjoint system to non-uniform duct are presented in Chapter 5. Chapter 6 gives a discussion on the relation between energy conservation and adjoint solutions. Reciprocal relations are studied and some numerical results are given in Chapter 7. Chapter 8 contains conclusions.

CHAPTER 2

LINEARIZED EULER SYSTEM

2.1 FORMULATION OF GOVERNING EQUATIONS

Aeroacoustics is a branch of Fluid Mechanics studying the mechanism of generation of noise by fluid motions and its propagation. We also consider gas and liquids as a continuum: we assume that we can define a "fluid particle" which is large to molecular scales but small compared to the other length scales. The fluid motion can be described by using the laws applied to an elementary fluid particle. The following fundamental laws are used to derive the governing differential equations that are solved in a Computational Fluid Dynamics (CFD) study. These laws are conservation of mass(continuity), conservation of linear momentum (Newton's second law) and conservation of energy (First law of thermodynamics). In principle the propagation of acoustic waves could be directly studied using the equations of the fluid motion, i.e. the Navier Stokes equations. However, in order to obtain equations more suitable for aeroacoustics, it is possible to introduce some approximations in the Navier Stokes equations. Under the assumptions of absence of friction and thermal conduction, and the fluid being a perfect gas, the Euler equations for the propagation of the sound waves can be obtained.

We begin with some history about the wave theory of sound. The history of sound is intrinsically linked to the history of waves. Scientists from Aristotle (384-322 B.C.) to Isaac Newton (1642-1727) made observation and worked on theories of sound propagation, wave theory and their relationships. Substantial progress toward the development of a viable theory of sound propagation resting on more firm mathematical and physical concepts was made during the eighteenth century by Euler (1707-1783), Lagrange (1736-1813) and d'Alembert (1717-1783). During this era, continuum physics, or field theory, began to receive a definite mathematical structure. The wave equation emerged in a number of contexts, including the propagation of sound in air. The theory ultimately proposed for sound in the eighteenth century was incomplete. The Euler equations first appeared in Euler's works [11, 12]. At the time

of Euler published his work, the system of equations consisted of the momentum and continuity equations. These two equations, the conservation of mass equation and Euler's equation of motion for a fluid, came without alterations from the eighteenth century. However, fluid dynamics literature often refers to the full set including the energy equation together as "the Euler equations". The third, which relates to the conservation of energy, is a nineteenth-century development. The conservation form of equations are obtained by applying the underlying physical principles to a fixed (non-moving) volume V within a moving fluid in Fig. 1. Applying these laws to an infinitesimal volume element yields the equations in differential form, which assumes that the fluid properties are continuous and that derivatives exist.

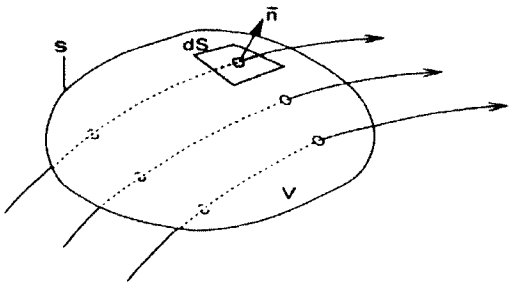

Fig. 1. Flow through a volume V with surface $\partial V \equiv S$.

In [40], the Euler equations for inviscid fluids are given

$$\text{Mass Conservation:} \qquad \frac{\partial \rho}{\partial t} + \nabla \cdot (\rho \boldsymbol{u}) = 0, \tag{1}$$

$$\text{Momentum Conservation:} \qquad \frac{\partial \boldsymbol{u}}{\partial t} + (\boldsymbol{u} \cdot \nabla)\boldsymbol{u} + \frac{1}{\rho}\nabla p = 0, \tag{2}$$

$$\text{Energy Conservation:} \qquad \frac{\partial E}{\partial t} + \nabla \cdot [(E + p)\,\boldsymbol{u}] = 0 \tag{3}$$

where ρ is the fluid mass density, $\boldsymbol{u}$ is the velocity vector with three components u_x, u_y and u_z, p is the pressure and E is the total energy. All of these conservation equations are derived assuming zero viscosity and holding the adiabatic condition. Viscosity is the quantity that describes a fluid's resistance to flow. Viscous effects are negligible in the acoustic field because the pressure represents a far greater stress

field than the viscous stresses. A fluid that has no resistance is known as an ideal fluid or inviscid fluid. In thermodynamics, an adiabatic process is one in which no heat is transferred to, or from, the working fluid.

In order to close the system of equations we need an equation of state for the pressure. To do that we assume that the medium is an ideal gas. Often this is also called a perfect fluid. For an ideal gas, the equation of state relating the pressure to the internal specific energy e is the following:

$$p = (\gamma - 1)\rho e$$

where γ is the adiabatic index.

Energy exists in many forms. Here we focus on the two most basic ones: the thermal (internal) specific energy e and the kinetic specific energy $e_{kin} = \boldsymbol{u}^2/2$. So the total energy, E, is $\rho(e + \boldsymbol{u}^2/2)$ per unit volume. By subtracting the product of the velocity and the momentum conservation equation (2) from the third equation, we can get

$$\frac{\partial \rho e}{\partial t} + \nabla \cdot (\rho e \boldsymbol{u}) + p \nabla \cdot \boldsymbol{u} = 0. \tag{4}$$

By plugging the equation of state into (4), the energy conservation equation can be expressed without "e" term as

$$\frac{\partial p}{\partial t} + \boldsymbol{u} \cdot \nabla p + \gamma p \nabla \cdot \boldsymbol{u} = 0. \tag{5}$$

Finally, we have five unknowns which can be obtained by solving the five Euler equations including (1), three components of (2) and (5) for inviscid fluids expressed as

$$\frac{\partial \rho}{\partial t} + \nabla \cdot (\rho \boldsymbol{u}) = 0,$$

$$\frac{\partial \boldsymbol{u}}{\partial t} + (\boldsymbol{u} \cdot \nabla)\boldsymbol{u} + \frac{1}{\rho}\nabla p = 0,$$

$$\frac{\partial p}{\partial t} + \boldsymbol{u} \cdot \nabla p + \gamma p \nabla \cdot \boldsymbol{u} = 0.$$

Acoustic disturbances can usually be regarded as small-amplitude perturbations to an ambient state (mean flow). For a fluid, the ambient state (mean flow) is characterized by those values $(\bar{\rho}, \bar{\boldsymbol{u}}, \bar{p})$ for the density, fluid velocity and pressure

when the perturbation is absent. Consider a small perturbation on a mean flow and let

$$\rho = \bar{\rho} + \rho',$$
$$\boldsymbol{u} = \bar{\boldsymbol{u}} + \boldsymbol{u}',$$
$$p = \bar{p} + p'$$

where a prime represents the acoustic contribution to the mean flow fields and an over bar indicates the time independent mean variable. The ambient state (mean flow) defines the medium through which sound propagates. Then we have

$$\frac{\partial(\bar{\rho} + \rho')}{\partial t} + \nabla \cdot ((\bar{\rho} + \rho')(\bar{\boldsymbol{u}} + \boldsymbol{u}') = 0,$$

$$\frac{\partial(\bar{\boldsymbol{u}} + \boldsymbol{u}')}{\partial t} + ((\bar{\boldsymbol{u}} + \boldsymbol{u}') \cdot \nabla)(\bar{\boldsymbol{u}} + \boldsymbol{u}') + \frac{1}{\bar{\rho} + \rho'}\nabla(\bar{p} + p') = 0,$$

$$\frac{(\bar{p} + p')}{\partial t} + (\bar{\boldsymbol{u}} + \boldsymbol{u}') \cdot \nabla(\bar{p} + p') + \gamma(\bar{p} + p')\nabla \cdot (\bar{\boldsymbol{u}} + \boldsymbol{u}') = 0.$$

Linearization leads to, for the first order,

$$\frac{\partial \rho'}{\partial t} + \nabla \cdot (\bar{\rho}\boldsymbol{u}' + \rho'\bar{\boldsymbol{u}}) = 0, \tag{6}$$

$$\frac{\partial \boldsymbol{u}'}{\partial t} + (\bar{\boldsymbol{u}} \cdot \nabla)\boldsymbol{u}' + (\boldsymbol{u}' \cdot \nabla)\bar{\boldsymbol{u}} + \frac{1}{\bar{\rho}}\nabla p' - \frac{1}{\bar{\rho}^2}\rho'\nabla\bar{p} = 0, \tag{7}$$

$$\frac{\partial p'}{\partial t} + \bar{\boldsymbol{u}} \cdot \nabla p' + \nabla\bar{p} \cdot \boldsymbol{u}' + \gamma\bar{p}(\nabla \cdot \boldsymbol{u}') + \gamma(\nabla \cdot \bar{\boldsymbol{u}})p' = 0. \tag{8}$$

We also assume that in the adiabatic process the entropy of the fluid remains constant. We call this process an isentropic process. In [26], for an isentropic flow of a perfect gas, the isentropic relationship between pressure and density fluctuations can be expressed as

$$c^2 = \frac{\gamma\bar{p}}{\bar{\rho}} \tag{9}$$

where c is the speed of sound.

Then, we write the linearized Euler equations in matrix form as

$$\frac{\partial \boldsymbol{w}}{\partial t} + \boldsymbol{A}\frac{\partial \boldsymbol{w}}{\partial x} + \boldsymbol{B}\frac{\partial \boldsymbol{w}}{\partial y} + \boldsymbol{C}\frac{\partial \boldsymbol{w}}{\partial z} + \boldsymbol{D}\boldsymbol{w} = 0 \tag{10}$$

where

$$\boldsymbol{w} = \begin{pmatrix} \rho' \\ u'_x \\ u'_y \\ u'_z \\ p' \end{pmatrix}, \boldsymbol{A} = \begin{pmatrix} \bar{u}_x & \bar{\rho} & 0 & 0 & 0 \\ 0 & \bar{u}_x & 0 & 0 & \frac{1}{\bar{\rho}} \\ 0 & 0 & \bar{u}_x & 0 & 0 \\ 0 & 0 & 0 & \bar{u}_x & 0 \\ 0 & \gamma\bar{p} & 0 & 0 & \bar{u}_x \end{pmatrix}, \boldsymbol{B} = \begin{pmatrix} \bar{u}_y & 0 & \bar{\rho} & 0 & 0 \\ 0 & \bar{u}_y & 0 & 0 & 0 \\ 0 & 0 & \bar{u}_y & 0 & \frac{1}{\bar{\rho}} \\ 0 & 0 & 0 & \bar{u}_y & 0 \\ 0 & 0 & \gamma\bar{p} & 0 & \bar{u}_y \end{pmatrix},$$

$$\boldsymbol{C} = \begin{pmatrix} \bar{u}_z & 0 & 0 & \bar{\rho} & 0 \\ 0 & \bar{u}_z & 0 & 0 & 0 \\ 0 & 0 & \bar{u}_z & 0 & 0 \\ 0 & 0 & 0 & \bar{u}_z & \frac{1}{\bar{\rho}} \\ 0 & 0 & 0 & \gamma\bar{p} & \bar{u}_z \end{pmatrix}, \boldsymbol{D} = \begin{pmatrix} \nabla\cdot\bar{\boldsymbol{u}} & \frac{\partial\bar{\rho}}{\partial x} & \frac{\partial\bar{\rho}}{\partial y} & \frac{\partial\bar{\rho}}{\partial z} & 0 \\ 0 & \frac{\partial\bar{u}_x}{\partial x} & \frac{\partial\bar{u}_x}{\partial y} & \frac{\partial\bar{u}_x}{\partial z} & -\frac{1}{\gamma\bar{\rho}\bar{p}}\frac{\partial\bar{p}}{\partial x} \\ 0 & \frac{\partial\bar{u}_y}{\partial x} & \frac{\partial\bar{u}_y}{\partial y} & \frac{\partial\bar{u}_y}{\partial z} & -\frac{1}{\gamma\bar{\rho}\bar{p}}\frac{\partial\bar{p}}{\partial y} \\ 0 & \frac{\partial\bar{u}_z}{\partial x} & \frac{\partial\bar{u}_z}{\partial y} & \frac{\partial\bar{u}_z}{\partial z} & -\frac{1}{\gamma\bar{\rho}\bar{p}}\frac{\partial\bar{p}}{\partial z} \\ 0 & \frac{\partial\bar{p}}{\partial x} & \frac{\partial\bar{p}}{\partial y} & \frac{\partial\bar{p}}{\partial z} & \gamma(\nabla\cdot\bar{\boldsymbol{u}}) \end{pmatrix}.$$

In the above, ρ is the density, u_x, u_y, u_z are the velocity components and p is the pressure. An over bar has been used to denote the mean state values and a prime indicates the small disturbances in the linearization.

For convenience in the rest of the paper, we denote (10) using a spatial operator $\boldsymbol{L}$ as

$$\frac{\partial \boldsymbol{w}}{\partial t} + \boldsymbol{L}(\boldsymbol{w}) = 0.$$

The Euler equation will be referred to as the forward problem in this thesis. The system of partial differential equations is supplemented with initial and boundary conditions.

2.2 DISPERSION RELATION

It is well known in wave propagation theory (e.g., [50]) that the dispersion relations help us understand the propagation characteristics of the waves of a system of partial differential equations. It is easy to manipulate equations once we know the dispersion relation. Conversely, we can construct the equation from the dispersion relation. The dispersion relation, i.e., $\omega = \omega(k)$, is a functional relation between the angular frequency ω of the waves and the wave numbers k of the spatial variables.

We can obtain this relation by applying space and time Fourier transforms to the governing equations. The group velocity, $d\omega/dk$, and the phase velocity, ω/k, are also both determined by the dispersion relation.

Understanding dispersive waves of the physical system is also very important to construct stable Perfectly Matched Layer (PML) [3, 22]. The PML is a vital subject for us since this technique is used for all numerical computations in this thesis. When deriving the PML equation for the Euler equation, all waves must have consistent phase and group velocities to avoid instability. The direction of wave propagation should be consistent with the sign of k/ω, or equivalently, the phase velocity ω/k in the PML domain [3, 22]. Since the direction of propagation of a dispersive wave is determined by the group velocity, the condition has been expressed in [3] as

$$\frac{k}{\omega}\frac{d\omega}{dk} > 0.$$

Conversely, in case they are in opposite directions, instability can be seen in the PML domain.

If the mean flow is nonuniform inside the duct, the duct mode dispersion relation would vary along the duct. For the nonuniform mean flows, there is no closed form dispersion relation. For the linearized Euler equations with a uniform mean flow in the direction of x, the duct dispersion relation for mode (m, n) in a rectangular duct can be determined.

After rewriting equations (6), (7) and (8) for a *uniform mean flow*, we have

$$\frac{\partial \rho'}{\partial t} + (\bar{\boldsymbol{u}} \cdot \nabla)\rho' + \bar{\rho}\nabla \cdot \boldsymbol{u}' = 0,$$

$$\frac{\partial \boldsymbol{u}'}{\partial t} + (\bar{\boldsymbol{u}} \cdot \nabla)\boldsymbol{u}' + \frac{1}{\bar{\rho}}\nabla p' = 0,$$

$$\frac{\partial p'}{\partial t} + (\bar{\boldsymbol{u}} \cdot \nabla)p' + \gamma\bar{p}(\nabla \cdot \bar{\boldsymbol{u}}') = 0.$$

In particular, consider a uniform duct with uniform cross section $D : [-L_y, L_y] \times [-L_z, L_z]$ as shown in Fig. 2 along (y, z) dimensions. In the direction of y and z there are wall boundaries. The mean flow is in the direction of x and denoted by $\bar{u}_x$. Then the linearized Euler equations are

$$\frac{\partial \rho'}{\partial t} + \bar{u}_x\frac{\partial \rho'}{\partial x} + \bar{\rho}\nabla \cdot \boldsymbol{u}' = 0, \tag{11}$$

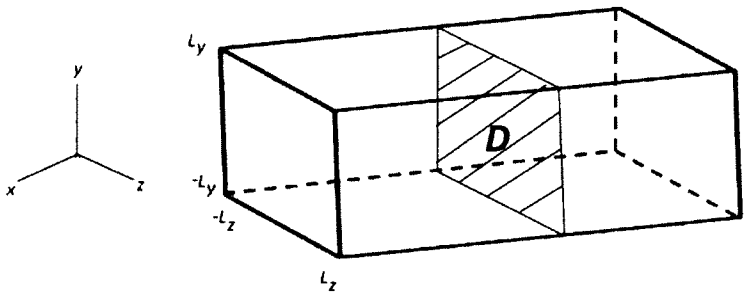

Fig. 2. A uniform duct with uniform cross section.

$$\frac{\partial \boldsymbol{u}'}{\partial t} + \bar{u}_x \frac{\partial \boldsymbol{u}'}{\partial x} + \frac{1}{\bar{\rho}} \nabla p' = 0, \tag{12}$$

$$\frac{\partial p'}{\partial t} + \bar{u}_x \frac{\partial p'}{\partial x} + \gamma \bar{p} (\nabla \cdot \boldsymbol{u}') = 0. \tag{13}$$

By eliminating $\boldsymbol{u}'$, we get

$$\left(\frac{\partial}{\partial t} + \bar{u}_x \frac{\partial}{\partial x} \right)^2 p' - c^2 \nabla^2 p' = 0 \tag{14}$$

where

$$c^2 = \frac{\gamma \bar{p}}{\bar{\rho}}.$$

The uniform mean flow has non-dimensionalized density and pressure: $\bar{\rho} = 1$ and $\bar{p} = 1/\gamma$ ($\gamma = 1.401$) respectively. Therefore,

$$c^2 = 1 \tag{15}$$

and also we compute density directly from pressure: $\rho = p$ since an isentropic relation is assumed.

A Fourier transform about x and t can be performed on the Euler equations (11)-(13). The duct modes are solutions of the form

$$\begin{pmatrix} u'_x(x,y,z,t) \\ u'_y(x,y,z,t) \\ u'_z(x,y,z,t) \\ p'(x,y,z,t) \end{pmatrix} = \begin{pmatrix} \hat{u}_x(y,z) \\ \hat{u}_y(y,z) \\ \hat{u}_z(y,z) \\ \hat{p}(y,z) \end{pmatrix} e^{ikx - i\omega t}. \tag{16}$$

Substituting equations (15) and (16) into (14), we get

$$(-i\omega + ik\bar{u}_x)^2 \hat{p} - (-k^2\hat{p} + \nabla^2\hat{p}) = 0 \tag{17}$$

where ∇^2 now denotes the Laplace operator in y and z dimensions. We write the equation (17) as the Helmholtz equation

$$\nabla^2\hat{p} + \lambda^2\hat{p} = 0 \tag{18}$$

where

$$\lambda^2 = (\omega - k\bar{u}_x)^2 - k^2. \tag{19}$$

The corresponding velocity components in (12) are

$$(\hat{u}_x, \hat{u}_y, \hat{u}_z) = \frac{-i}{(\omega - k\hat{u}_x)}(ik, \frac{\partial}{\partial y}, \frac{\partial}{\partial z})\hat{p}(y, z). \tag{20}$$

For a duct with a solid wall, the boundary condition for $\hat{p}(y, z)$ is

$$\boldsymbol{n} \cdot \nabla\hat{p} = 0, \quad \text{on } \partial D. \tag{21}$$

Equation (18) and boundary condition (21) form an eigenvalue problem. The eigenvalues and eigenfunctions will be denoted as

$$\lambda_{mn} \text{ and } \phi_{mn}(y, z). \tag{22}$$

For a rectangular duct with solid walls, the symmetric eigenfunctions can be defined

$$\phi_{mn}(y, z) = \cos\left(\frac{m\pi}{L_z}z\right)\cos\left(\frac{n\pi}{L_y}y\right)$$

with eigenvalues

$$\lambda_{mn} = \sqrt{\left(\frac{m\pi}{L_z}\right)^2 + \left(\frac{n\pi}{L_y}\right)^2}.$$

and the anti-symmetric eigenfunctions (in both y and z) can be defined

$$\phi_{mn}(y, z) = \sin\left(\frac{(2m+1)\pi}{2L_z}z\right)\sin\left(\frac{(2n+1)\pi}{2L_y}y\right)$$

with eigenvalues

$$\lambda_{mn} = \sqrt{\left(\frac{(2m+1)\pi}{2L_z}\right)^2 + \left(\frac{(2n+1)\pi}{2L_y}\right)^2}.$$

where $m = 0, 1, \ldots$, $n = 0, 1, \ldots$, are the mode numbers.

Equation (19) is the dispersion relation for mode (m, n). The corresponding eigenfunctions for the velocity component by (20) are

$$(\hat{u}_x, \hat{u}_y, \hat{u}_z) = \frac{-i}{(\omega - k\hat{u}_x)}(ik, \frac{\partial}{\partial y}, \frac{\partial}{\partial z})\phi_{mn}(y, z).$$

By solving equation (19) in terms of k, we get two roots for each eigenvalue λ_{mn} :

$$k_{mn}^{\pm} = \frac{\pm\sqrt{\omega^2 - (1 - M^2)\lambda_{mn}^2} - M\omega}{1 - M^2} \tag{23}$$

where ω is the wave frequency, k_{mn} is the wave number and $M = \bar{u}_x$.

Here, k_{mn}^{+} represents wave propagating in $+x$ direction and k_{mn}^{-} represents wave propagating in $-x$ direction. Note the condition for propagation of an acoustic mode is that the wave number k_{mn} must be real. Otherwise the wave will decay exponentially and is known as an evanescent wave. Another phenomena related to mode propagation is cutoff frequency that is the lowest frequency for which a mode will propagate. The cutoff frequency ω_c is the critical frequency between propagation and attenuation. Any frequency lower than the cutoff frequency will attenuate, rather than propagate.

For a uniform duct with a mean flow M, the cutoff frequency is for the symmetric eigenfunctions and anti-symmetric eigenfunctions, respectively,

$$\omega_c = \sqrt{\left(1 - M^2\right)\left(\left(\frac{m\pi}{L_z}\right)^2 + \left(\frac{n\pi}{L_y}\right)^2\right)}$$

and

$$\omega_c = \sqrt{\left(1 - M^2\right)\left(\left(\frac{(2m+1)\pi}{2L_z}\right)^2 + \left(\frac{(2n+1)\pi}{2L_y}\right)^2\right)}$$

where the integers $m, n \geq 0$ are the mode numbers, and L_y and L_z are the half-lengths of the sides of the rectangle.

All modes may be labeled by two integers (m, n). For a given frequency and in a given duct there will exist only a finite number of modes which are above cutoff. If the given frequency is greater than or equal to the cutoff frequency of a mode (m, n), the mode (m, n) is said to be cut-on. If it is not, the mode (m, n) is said to be cut-off. For a cut-on (propagating) mode,

$$\omega \geq \sqrt{1 - M^2}\lambda_{mn} \quad \text{and} \quad k_{mn} \text{ is real.}$$

For a cut-off (evanescent) mode,

$$\omega < \sqrt{1 - M^2}\lambda_{mn} \quad \text{and} \quad k_{mn} \text{ is complex.}$$

For the symmetric eigenfunctions, we report results in Figs. 3 and 4 for fixed m and arbitrary n as mode $(2, n)$ and mean flows with $M = 0$ and $M = 0.45$. A square duct is chosen with $L_y = 40$ and $L_z = 40$ for calculations (see Fig. 2).

For $M = 0$, the dispersion relation of the duct modes are plotted in Fig. 3. We choose a fixed frequency ω_f to explain the earlier subject better. At ω_f, the first four modes are cut-on. For $M = 0.45$, the dispersion relation of the duct modes are plotted in Fig. 4. At ω_f, the first five modes are cut-on.

For the anti-symmetric eigenfunctions, the dispersion relations are shown in Figs. 5 and 6 for arbitrary m and fixed n as mode $(m, 1)$ with $M = 0$ and $M = 0.45$. At ω_f, the first four modes are cut-on for $M = 0$ and the first five modes are cut-on for $M = 0.45$.

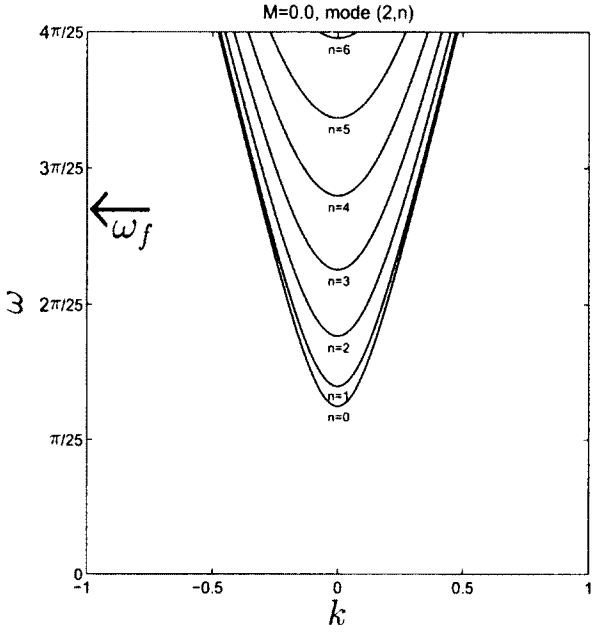

Fig. 3. For the symmetric eigenfunctions, the dispersion relation shows 4 cut-on radial modes at ω_f when $M = 0$.

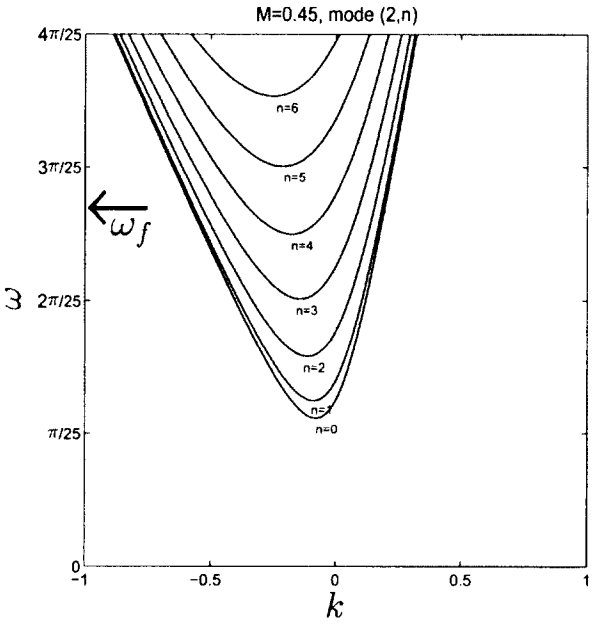

Fig. 4. For the symmetric eigenfunctions, the dispersion relation shows 5 cut-on radial modes at ω_f when $M = 0.45$.

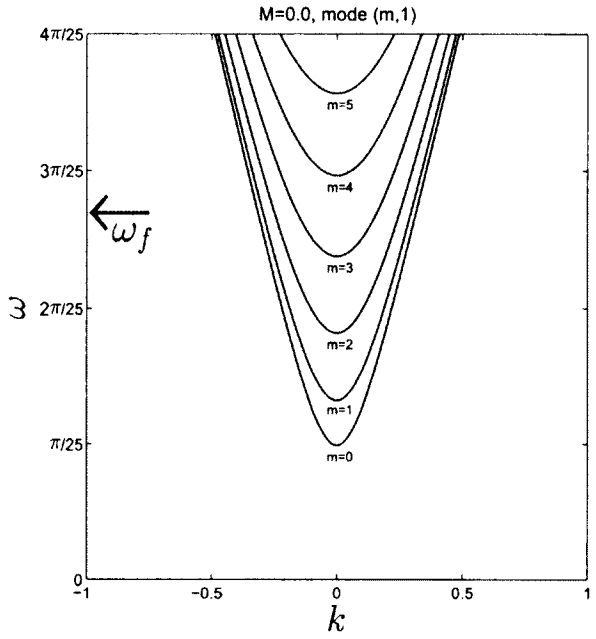

Fig. 5. For the anti-symmetric eigenfunctions, the dispersion relation shows 4 cut-on radial modes at ω_f when $M = 0$.

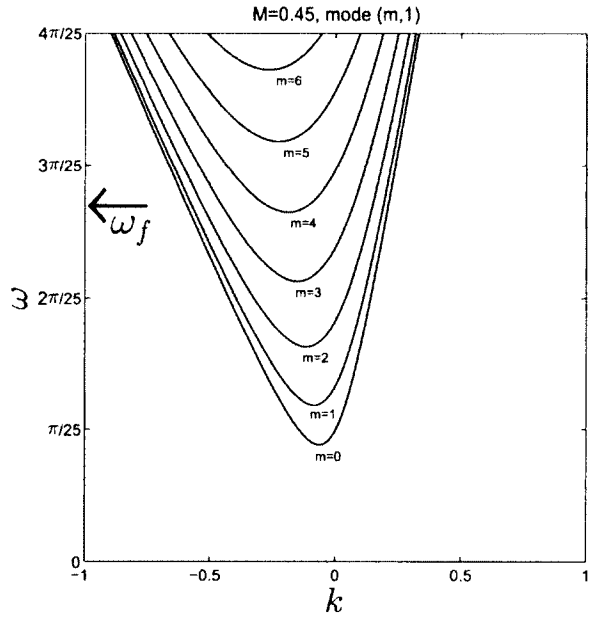

Fig. 6. For the anti-symmetric eigenfunctions, the dispersion relation shows 5 cut-on radial modes at ω_f when $M = 0.45$.

CHAPTER 3

TIME DOMAIN WAVE PACKET METHOD

3.1 DEFINITION OF TIME DOMAIN WAVE PACKET METHOD

In most conventional time domain linear aeroacoustics computations, sinusoidal functions are used to model acoustic sources such as point sources or incoming wave modes. These sinusoidal functions are defined in time with fixed frequencies of interest. Then, the numerical simulation is carried out until it reaches a time periodic state. In the Time domain wave packet method, the acoustic source is modeled as a wave packet with a relatively short time duration. In other words, the source time function is modeled by a temporally compact broadband pulse. Such a source generates a wave packet that contains a broad range of frequencies, as shown in Fig. 7. For linear problems, wave propagation characteristics at all frequencies within the numerical resolution are embedded in the propagation of the wave packet. In short, by an FFT, solutions at all frequencies can be obtained in a single time domain simulation. The numerical simulation just needs to last until the wave packet has propagated out of the computational domain. As a result, by obtaining all frequencies in a single time domain computation in a shorter time duration, the TDWP method is more efficient than the conventional method.

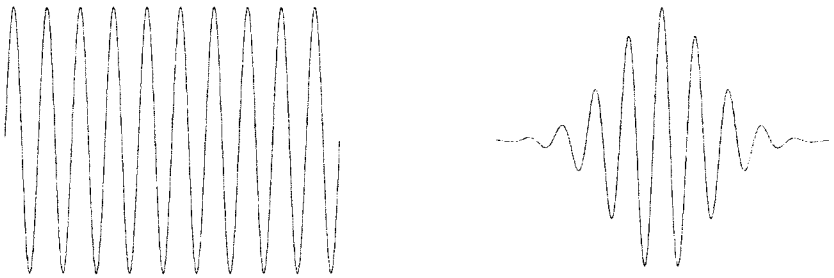

Fig. 7. Schematic for a time signal of a sinusoidal wave (left) and a wave packet (right).

The acoustic source can be modeled by a time function with a wide spectrum. In

order to generate a broadband wave packet, we use the following simple time function

$$\Psi(t) = \begin{cases} \frac{\Delta t \sin(\omega_0 t)}{\pi t} e^{(\ln \delta)(t/N\Delta t)^2} & |t| \leq N\Delta t \\ 0 & |t| > N\Delta t \end{cases} \tag{24}$$

where Δt is the time step in the time domain simulation, δ is a small number, and N and ω_0 are adjustable parameters of the function. This function is non-zero only for a limited time duration, $-N\Delta t \leq t \leq N\Delta t$, while its spectrum is broadband and covers frequencies up to slightly beyond ω_0. There are other time and frequency band-limited functions (see, e.g.,[27]).

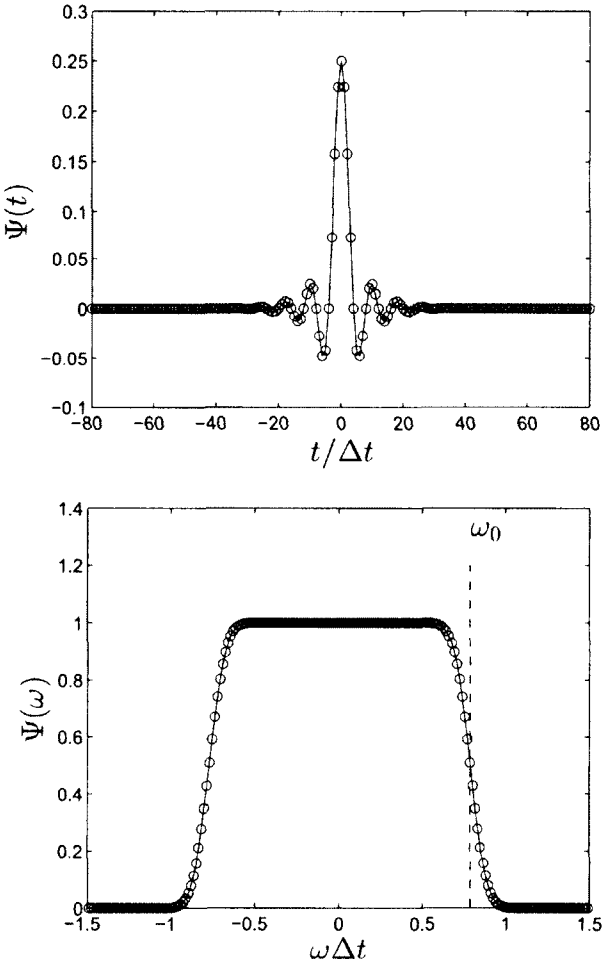

Fig. 8. Illustration of Broadland Acoustic Test Pulse time function $\Psi(t)$ and its spectrum $\Psi(\omega)$.

Fig. 8 gives an example of $\Psi(t)$ and its spectrum $\Psi(\omega)$ where the parameters are

$N = 40$, $\omega_0 \Delta t = \pi/4$ and $\delta = 0.01$. The width of the spectrum can be controlled by parameter ω_0. When using the above example of $\Psi(t)$ in expression of a source, the acoustic source will be non-zero for only 80 time steps. All waves with a period as small as $4\Delta t$, or a frequency as large as $1/4\Delta t$, will be included in the computation. Compared to a single frequency source functions, use of a wave packet has the following advantages: (1) One computation for all frequencies within numerical resolution; (2) A very short time duration at the source; (3) Possibility of separation of acoustic and instability waves; (4) Ability to synthesize broadband noise source.

Another benefit of the Time Domain Wave Packet method is that it makes possible to separate acoustic waves and instability waves in the shear flow, as these two kinds of waves travel at different speeds [7, 8]. After the separation of instability and acoustic waves, there are some instability suppression techniques such as the Mean Flow Gradient Removal (MFGR) method [4] and the Source Filtering (SF) technique [29, 24] that can be used. These methods suppress the instability waves and have as little effect as possible on the acoustic wave.

In this thesis, we develop the TDWP method for duct acoustics. Theoretical analysis and numerical issues related to the application of the TDWP method to duct acoustics will be studied.

3.2 DUCT MODE IMPOSITION

In this section, methods for the application of the Time Domain Wave Packet method to duct radiation problems in rectangular uniform duct with flow will be developed. Mathematical analysis of the method will also be presented. To generate the wave packet inside the duct, a forcing terms whose time function is given by (24) is to be introduced. A key point in TDWP method is the modeling of the source term. For the duct modes, it is proposed that the source term can be expressed as

$$S_{TDWP}(x, y, z, t) = \Psi(t)\phi_{mn}(y, z)e^{-\sigma(x-x_S)^2} \tag{25}$$

where $\phi_{mn}(y, z)$ is the eigenfunction (mode shape) of the mode (m, n) and $\sigma = \ln 2/b^2$. Here x_S denotes the location of the source plane inside the duct and b is the half-width of the source region. This source function is used to generate a wave packet for the mode (m, n) inside the duct. Of course a combination of multiple modes may also be used to express a desired source function. We first show an example of modeling the duct incoming waves in the TDWP method. To generate the duct

modes, the pressure equation given in matrix form of linearized Euler equations (10) is modified with source term S_{TDWP} given in (25) as

$$\frac{\partial p}{\partial t} + \bar{u}_x \frac{\partial p}{\partial x} + \gamma \bar{p} \left(\frac{\partial u_x}{\partial x} + \frac{\partial u_y}{\partial y} + \frac{\partial u_z}{\partial z} \right) = \Psi(t) \phi_{mn}(y, z) e^{-\sigma(x - x_s)^2}. \tag{26}$$

In the following section, an analytic solution for source term posed in (26) inside the rectangular duct with solid walls will be derived. Then, a simulation is carried out for a computational solution produced by using (26). Both analytic and computational solutions are examined and compared in the following sections.

3.3 ANALYTICAL SOLUTION FOR DUCT MODE IMPOSITION

In this section, the analytic solution is derived for the linearized Euler equations under mode forcing of (26). Since the eigenfunctions by (22) form a complete set of orthogonal basis functions in the (y, z) dimensions, the acoustic solution (where $p \neq 0$) inside the duct can be expressed as

$$p'(x, y, z, t) = \sum_{m,n} p_{mn}(x, t) \phi_{mn}(y, z). \tag{27}$$

To impose a particular duct mode (m_0, n_0) in a time domain simulation as formulated in (26), we solve the linearized Euler equations with the following forcing terms which are expressed with the source plane centered at x_0:

$$\frac{\partial \rho'}{\partial t} + \bar{u}_x \frac{\partial \rho'}{\partial x} + \bar{\rho} \nabla \cdot \boldsymbol{u}' = \phi_{m_0 n_0}(y, z) \Psi(t) e^{-\sigma(x - x_0)^2}, \tag{28}$$

$$\frac{\partial \boldsymbol{u}'}{\partial t} + \bar{u}_x \frac{\partial \boldsymbol{u}'}{\partial x} + \frac{1}{\bar{\rho}} \nabla p' = 0, \tag{29}$$

$$\frac{\partial p'}{\partial t} + \bar{u}_x \frac{\partial p'}{\partial x} + \gamma \bar{p} (\nabla \cdot \boldsymbol{u}') = \phi_{m_0 n_0}(y, z) \Psi(t) e^{-\sigma(x - x_0)^2}. \tag{30}$$

By eliminating $\boldsymbol{u}'$, we get

$$\left(\frac{\partial}{\partial t} + \bar{u}_x \frac{\partial}{\partial x} \right)^2 p' - c^2 \nabla^2 p' = \left(\frac{\partial}{\partial t} + \bar{u}_x \frac{\partial}{\partial x} \right) \phi_{m_0 n_0}(y, z) \Psi(t) e^{-\sigma(x - x_0)^2}.$$

By substituting (27) into the above, we have

$$\left(\frac{\partial}{\partial t} + \bar{u}_x \frac{\partial}{\partial x} \right)^2 \sum_{m,n} p_{mn}(x, t) \phi_{mn}(y, z) - c^2 \nabla^2 \sum_{m,n} p_{mn}(x, t) \phi_{mn}(y, z) = \left(\frac{\partial}{\partial t} + \bar{u}_x \frac{\partial}{\partial x} \right) \phi_{m_0 n_0}(y, z) \Psi(t) e^{-\sigma(x - x_0)^2}.$$

Due to orthogonality of the eigenfunctions, we easily find that $\hat{p}_{mn} = 0$, for $m \neq m_0$ and $n \neq n_0$. What turns out is the following equation

$$\left(\frac{\partial}{\partial t} + \bar{u}_x \frac{\partial}{\partial x}\right)^2 \hat{p}_{m_0 n_0}\phi_{m_0 n_0} - c^2\left(\frac{\partial^2 \hat{p}_{m_0 n_0}}{\partial x^2}\phi_{m_0 n_0} + \hat{p}_{m_0 n_0}\nabla^2\phi_{m_0 n_0}\right) = \left(\frac{\partial}{\partial t} + \bar{u}_x \frac{\partial}{\partial x}\right)\phi_{m_0 n_0}(y,z)\Psi(t)e^{-\sigma(x-x_0)^2}$$

which is, by (18) and (22),

$$\left(\frac{\partial}{\partial t} + \bar{u}_x \frac{\partial}{\partial x}\right)^2 \hat{p}_{m_0 n_0} - c^2\frac{\partial^2 \hat{p}_{m_0 n_0}}{\partial x^2} + \lambda^2_{m_0 n_0}\hat{p}_{m_0 n_0} = \left(\frac{\partial}{\partial t} + \bar{u}_x \frac{\partial}{\partial x}\right)\Psi(t)e^{-\sigma(x-x_0)^2}. \tag{31}$$

This is the inhomogeneous advection Klein-Gordon equation.
The Green's function for the Klein-Gordon equation

$$\frac{\partial^2 g}{\partial t^2} - c^2\frac{\partial^2 g}{\partial x^2} + k^2 g = \delta(x - x')\delta(t - t')$$

is given in [9] as

$$g(x,t;x',t') = \frac{1}{2c}J_0\left(k\sqrt{(t-t')^2 - (x-x')^2/c^2}\right) H(t - t' - |x - x'|/c)$$

where J_0 is Bessel function of the first kind for order 0 and H is the step function. The Heaviside unit step function is defined

$$H(\xi) = \begin{cases} 1 & \text{if} \quad \xi > 0 \\ 0 & \text{if} \quad \xi < 0. \end{cases}$$

The Heaviside step function has a value of unity when the argument of the function is positive and a value of zero when the argument of the function is negative.
In order to find the Green's function for the advection Klein-Gordon equation

$$\left(\frac{\partial}{\partial t} + \bar{u}_x \frac{\partial}{\partial x}\right)^2 G - c^2\frac{\partial^2 G}{\partial x^2} + \lambda^2 G = \delta(x - x')\delta(t - t')$$

consider the Prandtl-Gluert transformation [49]:

$$\bar{t} = t + \beta x$$

where

$$\beta = \frac{\bar{u}_x}{c^2 - \bar{u}_x^2}. \tag{32}$$

After applying this transformation, we get the following equation in variables x and $\bar{t}$

$$\left(\frac{\partial}{\partial \bar{t}} + \bar{u}_x \frac{\partial}{\partial x} + \bar{u}_x \beta \frac{\partial}{\partial \bar{t}}\right)^2 G - c^2 \left(\frac{\partial}{\partial x} + \beta \frac{\partial}{\partial \bar{t}}\right)^2 G + \lambda^2 G = \delta(x - x')\delta(\bar{t} - \beta x - t')$$

which can be simplified to

$$\left(1 + \bar{u}_x^2 \beta^2 + 2\bar{u}_x \beta - c^2 \beta^2\right) \frac{\partial^2 G}{\partial \bar{t}^2} - (c^2 - \bar{u}_x^2) \frac{\partial^2 G}{\partial x^2} + \lambda^2 G = \delta(x - x')\delta(\bar{t} - \beta x - t').$$

By using (32), we get

$$\frac{\partial^2 G}{\partial \bar{t}^2} - \frac{(c^2 - \bar{u}_x^2)^2}{c^2} \frac{\partial^2 G}{\partial x^2} + \frac{(c^2 - \bar{u}_x^2)}{c^2} \lambda^2 G = \frac{(c^2 - \bar{u}_x^2)}{c^2} \delta(x - x')\delta(\bar{t} - \beta x - t').$$

Let

$$\alpha = \sqrt{\frac{c^2 - \bar{u}_x^2}{c^2}}, \quad \bar{x} = x \frac{c^2}{c^2 - \bar{u}_x^2} = \frac{x}{\alpha^2}$$

then we have

$$\frac{\partial^2 G}{\partial \bar{t}^2} - c^2 \frac{\partial^2 G}{\partial \bar{x}^2} + \alpha^2 \lambda^2 G = \delta(\bar{x} - \bar{x}')\delta(\bar{t} - \beta x - t') \tag{33}$$

where we have used the fact that

$$\delta(x - x') = \delta(\alpha^2(\bar{x} - \bar{x}')) = \frac{1}{\alpha^2} \delta(\bar{x} - \bar{x}').$$

This gives the Green's function for equation (31) as

$$G(x - x', t - t') = \frac{1}{2c} \Bigg[J_0 \left(\alpha \lambda \sqrt{(t - t' + \beta(x - x'))^2 - (x - x')^2/\alpha^4 c^2} \right) \times H\left(t - t' + \beta(x - x') - |x - x'|/\alpha^2 c\right) \Bigg]. \tag{34}$$

Therefore, using this Green's function, we have

$$\hat{p}_{m_0 n_0}(x, t) = \int_{-\infty}^{\infty} \int_{-\infty}^{\infty} G(x - x', t - t') \left(\frac{\partial}{\partial t'} + \bar{u}_x \frac{\partial}{\partial x'}\right) \left[\Psi(t') e^{-\sigma(x' - x_0)^2}\right] dx' dt'$$

$$= \frac{1}{2c} \int_{-\infty}^{\infty} \int_{-\infty}^{\infty} \Bigg[J_0 \left(\alpha \lambda_{m_0 n_0} \sqrt{(t - t' + \beta(x - x'))^2 - (x - x')^2/\alpha^4 c^2} \right) \times H\left(-t' + \beta(x - x') - |x - x'|/\alpha^2 c\right) \left(\frac{\partial}{\partial t'} + \bar{u}_x \frac{\partial}{\partial x'}\right) \left[\Psi(t') e^{-\sigma(x' - x_0)^2}\right] \Bigg] dx' dt'$$

$$= \frac{1}{2c}\int_{-\infty}^{\infty}\int_{-\infty}^{t+\beta(x-x')-|x-x'|/\alpha^2 c}\left[J_0\left(\alpha\lambda_{m_0n_0}\sqrt{(t-t'+\beta(x-x'))^2-(x-x')^2/\alpha^4c^2}\right)\right.$$
$$\left.\times\frac{D}{Dt'}\left[\Psi(t')e^{-\sigma(x'-x_0)^2}\right]\right]dt'dx'$$

where

$$\frac{D}{Dt'} = \frac{\partial}{\partial t'} + \bar{u}_x\frac{\partial}{\partial x'}.$$

Denote

$$S(x,t) = \left(\frac{\partial}{\partial t} + \bar{u}_x\frac{\partial}{\partial x}\right)\Psi(t)e^{-\sigma(x-x_0)^2} = \left(\frac{\partial\Psi(t)}{\partial t} - 2\bar{u}_x\sigma(x-x_0)\Psi(t)\right)e^{-\sigma(x-x_0)^2},$$

$$K(x-x',t-t') = J_0\left(\alpha\lambda_{m_0n_0}\sqrt{(t-t'+\beta(x-x'))^2-(x-x')^2/\alpha^4c^2}\right),$$

and assume $S(x,t)$ is non-zero only in $[x_0-L, x_0+L]\times[-T,T]$, then we have

$$\hat{p}_{m_0n_0}(x,t) = \frac{1}{2c}\int_{x_0-L}^{x_0+L}\int_{-T}^{T'}K(x-x',t-t')S(x',t')dx'dt' \tag{35}$$

where

$$T' = min\{t+\beta(x-x') - \frac{|x-x'|}{\alpha^2 c}, T\}.$$

Equation (35) is the analytical solution for pressure to the linearized Euler equations (28)-(30).

For spectrum of the time domain solution (35), note that

$$\int_x^{\infty} J_0(\lambda\sqrt{t^2-x^2})sin(\omega t)dt = \begin{cases} 0 & 0<\omega<\lambda \\ \frac{cos(x\sqrt{\omega^2-\lambda^2})}{\sqrt{\omega^2-\lambda^2}} & 0<\lambda<\omega \end{cases}$$

and

$$\int_x^{\infty} J_0(\lambda\sqrt{t^2-x^2})cos(\omega t)dt = \begin{cases} \frac{e^{-x\sqrt{\lambda^2-\omega^2}}}{\sqrt{\lambda^2-\omega^2}} & 0<\omega<\lambda \\ \frac{-sin(x\sqrt{\omega^2-\lambda^2})}{\sqrt{\omega^2-\lambda^2}} & 0<\lambda<\omega \end{cases}$$

giving

$$\int_x^{\infty} J_0(\lambda\sqrt{t^2-x^2})e^{-i\omega t}dt = \begin{cases} \frac{e^{-x\sqrt{\lambda^2-\omega^2}}}{\sqrt{\lambda^2-\omega^2}} & 0<\omega<\lambda \\ \frac{-ie^{-ix\sqrt{\omega^2-\lambda^2}}}{\sqrt{\omega^2-\lambda^2}} & 0<\lambda<\omega \end{cases}$$

or

$$\int_{-\infty}^{\infty} J_0(\lambda\sqrt{t^2-x^2})H(t-x)e^{-i\omega t}dt = \begin{cases} \frac{e^{-x\sqrt{\lambda^2-\omega^2}}}{\sqrt{\lambda^2-\omega^2}} & 0<\omega<\lambda \\ \\ \frac{-ie^{-ix\sqrt{\omega^2-\lambda^2}}}{\sqrt{\omega^2-\lambda^2}} & 0<\lambda<\omega. \end{cases}$$

We can consider the following transformations

$$\bar{t} = t - t' + \beta(x-x')$$

and

$$\bar{x} = \frac{|x-x'|}{\alpha^2 c}. \tag{36}$$

Thus,

$$\int_{-\infty}^{\infty} \left[J_0\left(\alpha\lambda_{m_0n_0}\sqrt{(t-t'+\beta(x-x'))^2-(x-x')^2/\alpha^4c^2}\right) \right.$$
$$\left. \times H\left(t-t'+\beta(x-x')-\frac{|x-x'|}{\alpha^2c}\right)e^{-i\omega t}\right]dt$$

$$= e^{-i\omega[t'-\beta(x-x')]}\int_{-\infty}^{\infty} J_0\left(\alpha\lambda_{m_0n_0}\sqrt{\bar{t}^2-\bar{x}^2}\right)H(\bar{t}-\bar{x})e^{-i\omega\bar{t}}d\bar{t}$$

$$= \begin{cases} \frac{e^{\bar{x}\sqrt{\bar{\lambda}^2_{m_0n_0}-\omega^2}}}{\sqrt{\bar{\lambda}^2_{m_0n_0}-\omega^2}}e^{-i\omega[t'-\beta(x-x')]} & 0<\omega<\bar{\lambda}_{m_0n_0} \\ \\ \frac{-ie^{-i\bar{x}\sqrt{\omega^2-\bar{\lambda}^2_{m_0n_0}}}}{\sqrt{\omega^2-\bar{\lambda}^2_{m_0n_0}}}e^{-i\omega[t'-\beta(x-x')]} & 0<\bar{\lambda}_{m_0n_0}<\omega \end{cases}$$

where $\bar{\lambda}_{m_0n_0} = \alpha\lambda_{m_0n_0}$.

Therefore, the Fourier transform of $\hat{p}_{m_0n_0}(x,t)$ which is formulated as (35) is

$$\tilde{p}_{m_0n_0}(x,\omega) = \int_{-\infty}^{\infty}\hat{p}_{m_0n_0}(x,t)e^{-i\omega t}dt$$

$$= \begin{cases} \frac{1}{2c}\int_{-X}^{X}\int_{-T}^{T'}\frac{e^{-\bar{x}\sqrt{\bar{\lambda}^2_{mn}-\omega^2}}}{\sqrt{\bar{\lambda}^2_{mn}-\omega^2}}e^{-i\omega[t'-\beta(x-x')]}\frac{D}{Dt'}\left[\Psi(t')e^{-\sigma x'^2}\right]dx'dt' & 0<\omega<\bar{\lambda}_{mn} \\ \\ \frac{1}{2c}\int_{-X}^{X}\int_{-T}^{T'}\frac{-ie^{-i\bar{x}\sqrt{\omega^2-\bar{\lambda}^2_{mn}}}}{\sqrt{\omega^2-\bar{\lambda}^2_{mn}}}e^{-i\omega[t'-\beta(x-x')]}\frac{D}{Dt'}\left[\Psi(t')e^{-\sigma x'^2}\right]dx'dt' & 0<\bar{\lambda}_{mn}<\omega \end{cases} \tag{37}$$

where $[-X, X]$ is the source region in x and $[-T, T']$ is the time duration for the source term. Equation (37) indicates that the solution decays exponentially for cut-off frequencies.

3.4 APPLICATION OF THE TDWP METHOD TO UNIFORM DUCT

In this section, we present and examine numerical results of both the analytic and computational solutions.

For analytic solutions, the formula (35) can be used to calculate pressure at a point inside the duct. There are many numerical integration methods to evaluate the integrals in (35). We use Simpson's rule for these computations.

For computational solutions of (28)-(30), a time domain finite difference scheme is used. The spatial derivatives are approximated by a 7-point stencil as in the Dispersion Relation Preserving (DRP) scheme [48]. Time integration is carried using the Low Dissipation and Low Dispersion Runge-Kutta scheme (LDDRK 56) [23]. Both the spatial and temporal schemes are optimized for wave propagations. Perfectly Matched Layer (PML) absorbing boundary conditions [22, 21, 31] are applied at all the non-reflecting boundaries that are on the left and right hand sides of the duct along the x axis. Schematics of the computational domain for a rectangular duct is shown in Fig. 9.

A TDWP simulation can be carried out for each individual mode (m, n). This is done by specifying the source function given in (25) at a source plane located at $x_S = 0$. By using this source term, propagation and radiation of the chosen mode at

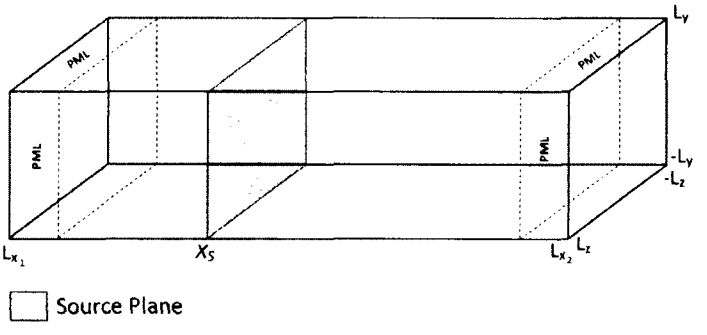

Fig. 9. Schematic of the computational domain for a rectangular duct.

all frequencies are computed at once. At the frequencies above the cutoff, the wave mode will be propagating in the duct. The numerical results for a implementation of the TDWP method to Euler equations by using symmetric and anti-symmetric eigenfunctions are shown on 2-D slices for the 3-D rectangular duct in Figs. 10-11 and 12-13, respectively. To get the time sequence of sample instantaneous pressure contours, the simulation is carried out with the forced mode $(2,1)$ and $M = 0.45$. The $(\diamond)$ on the contour plots represents the location of the source plane.

The waves that propagate toward the non-reflecting boundaries inside the duct are absorbed by the PML. There is no visible reflection. On the contour plots, the dashed lines indicate where the PML region starts.

Due to the dispersive nature of the duct modes, as shown in the dispersion relations in Figs. 3 and 4, the waves with a higher frequency have a larger group velocity (slope of the dispersion curve) and thus will arrive at an observer point inside the duct sooner than the waves with a lower frequency.

For an example, suppose mode $(2,1)$ and symmetric eigenfunctions are used to demonstrate an analytic solution and to simulate a computational solution. A comparison between them in pressure history at a fixed point located at $(100, 10, 10)$ is shown in Fig. 14. The Mach number of the mean flow is 0.45. The Gaussian window function is applied to both for a limited time duration. The Gaussian window function is applied from $t = 2000$ to the end. There is very little difference between the exact solution and the numerical solution.

A comparison between the FFTs of the analytic solution and the numerical solution at a fixed point $(100, 0, 0)$ is also given in Fig. 15 (top). The analytic solution is found by using a formula expressed as (37). We can find a FFT of the time signal at $(100, 0, 0)$ for the numerical solution. It is clear that they are in good agreement. The bottom of Fig. 15 is a scaled version of the top figure with ω in $[0, 1.4]$ to more easily compare the numerical and analytic results. On the graph, there are some notations as $\{\omega_1, \omega_2, \omega_3, \omega_4\}$ to indicate different frequency values for future reference.

A FFT of the time signal at a different point (100,10,10) is also given separately in Fig. 16. This graph is also scaled with ω in $[0, 1]$. In both Figs. 15 and 16, it is shown that no cutoff frequency is present at the fixed point. This is consistent with the dispersion relations given in Fig. 4 for the symmetric eigenfunctions.

By a single TDWP simulation, all cut-on frequencies can be obtained for the acoustic waves with or without mean flows.

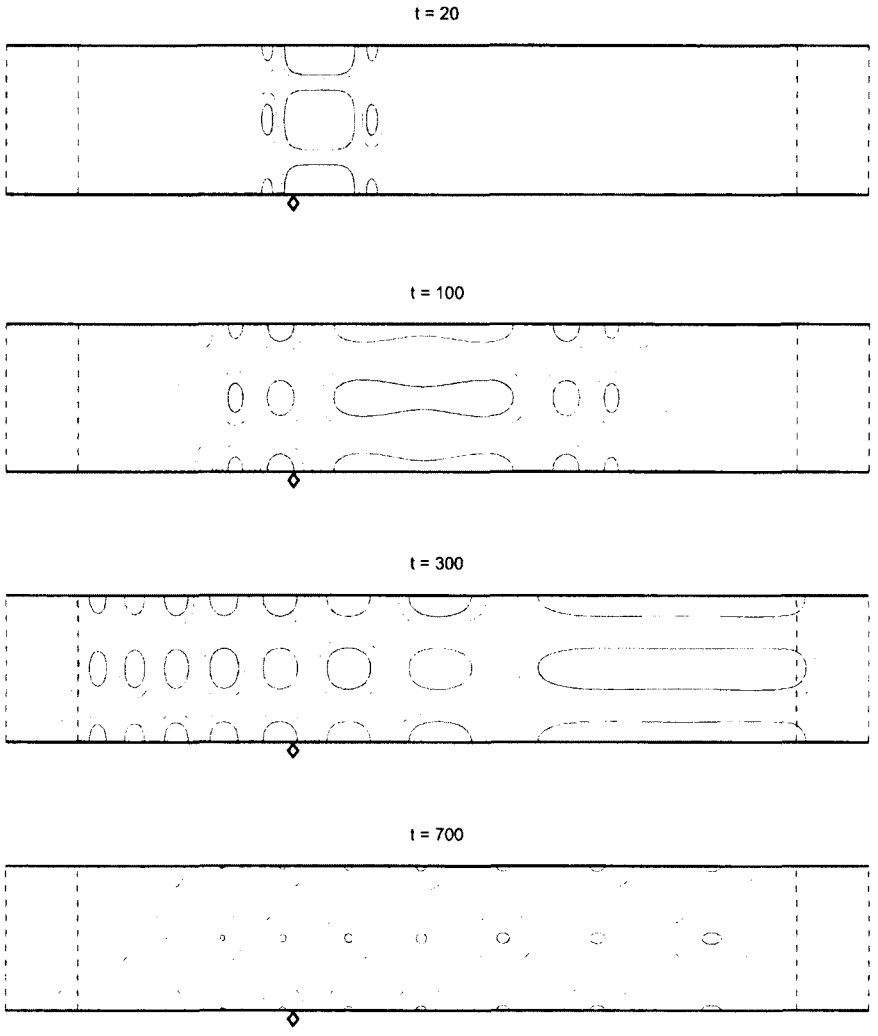

Fig. 10. A time sequence of instantaneous pressure contours of an acoustic wave packet by the symmetric eigenfunctions on the xy slice at $z = 0$ for the uniform duct.

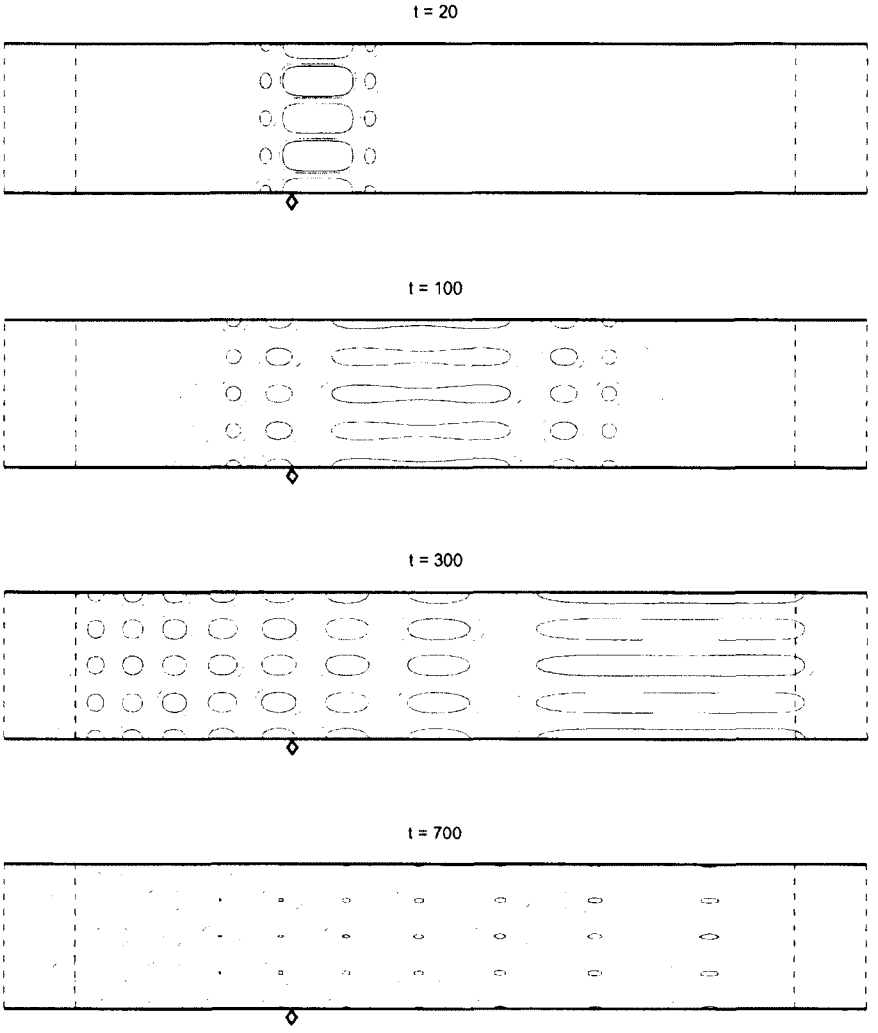

Fig. 11. A time sequence of instantaneous pressure contours of an acoustic wave packet by the symmetric eigenfunctions on the xz slice at $y = 0$ for the uniform duct.

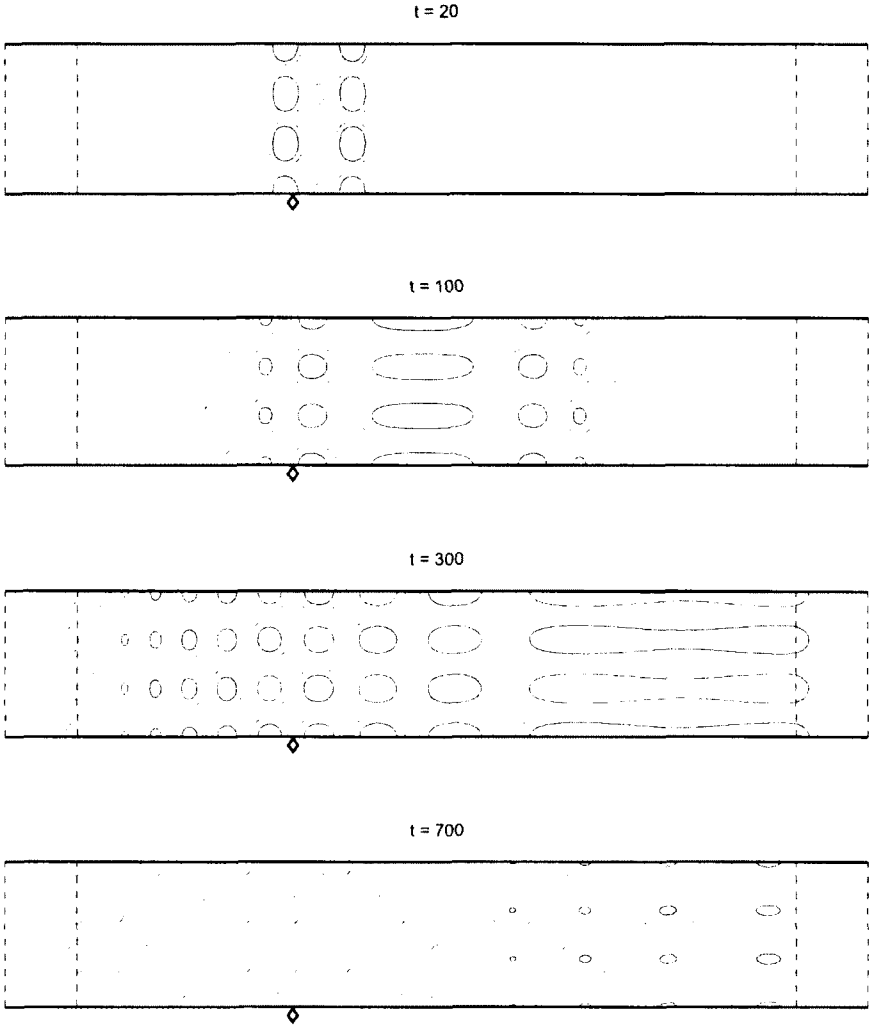

Fig. 12. A time sequence of instantaneous pressure contours of an acoustic wave packet by the anti-symmetric eigenfunctions on the xy slice at $z = 0$ for the uniform duct.

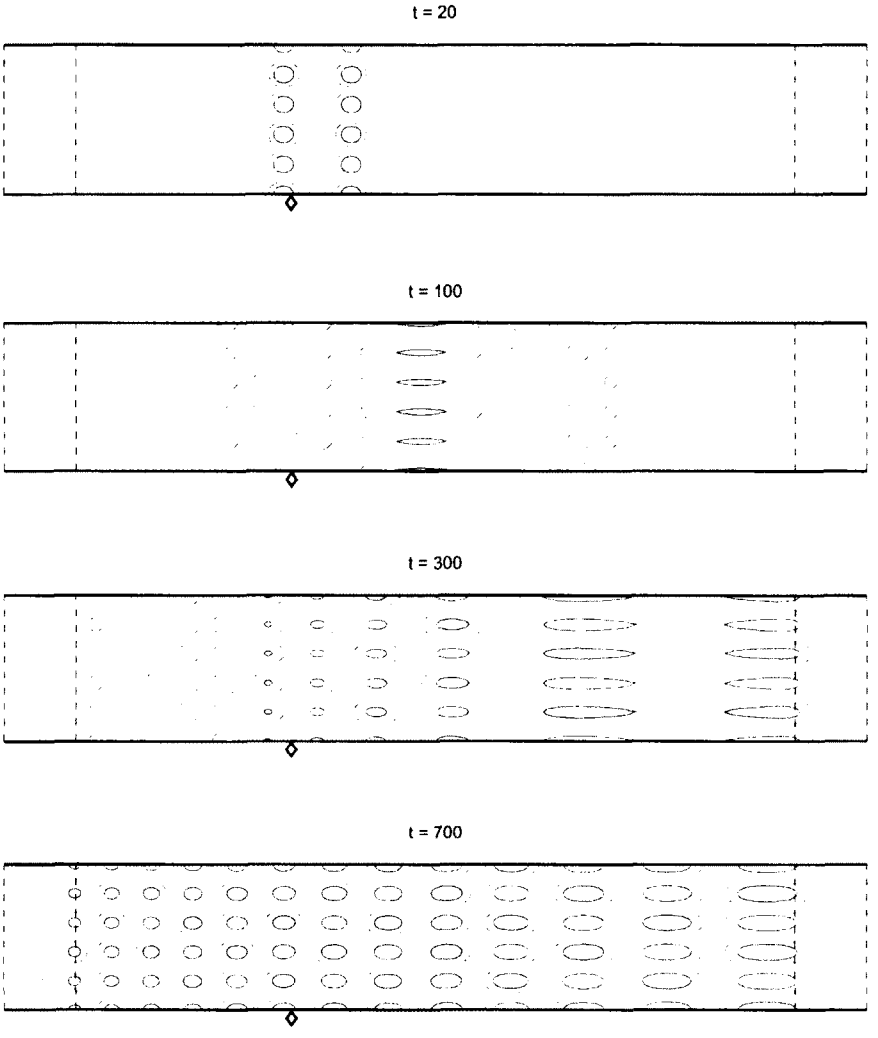

Fig. 13. A time sequence of instantaneous pressure contours of an acoustic wave packet by the anti-symmetric eigenfunctions on the xz slice at $y = 0$ for the uniform duct.

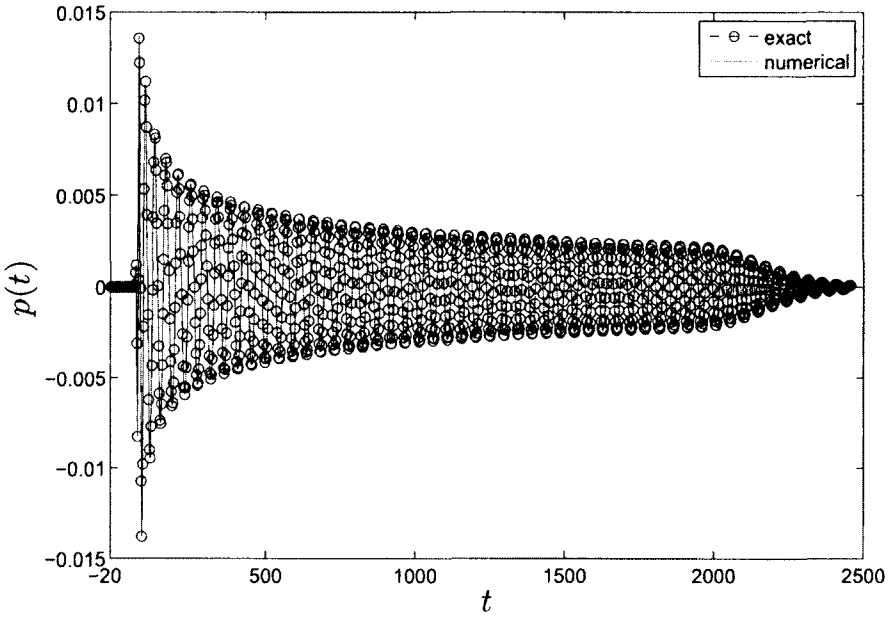

Fig. 14. Pressure time history at (100,10,10) with $M = 0.45$.

3.5 MODAL DECOMPOSITION

The modal decomposition method is of interest for sound propagation in ducts: At any x location, the numerical solution inside the duct is decomposed into right- and left-traveling modes as described below. The amplitudes of the acoustic modes propagating in a duct can be determined by the duct modal decomposition technique [44, 1, 46]. It makes possible to investigate and understand the propagation of sound in ducts. This means that the sound must be measured and analyzed in a such way that the results are meaningful in terms of the physics of the propagation process. In this procedure it is assumed that the duct eigenfunctions and eigenvalues are known. Here, we analyze the converted frequency domain solution by using the duct modal decomposition method.

First, the time domain solution inside the duct is converted to the frequency domain solution by FFT:

$$\text{Pressure:} \quad p_m(x,y,z,t) \rightarrow FFT \rightarrow \hat{p}_m(x,y,z,\omega).$$
$$\text{Axial velocity:} \quad u_m(x,y,z,t) \rightarrow FFT \rightarrow \hat{u}_m(x,y,z,\omega).$$

Second, at selected x locations, the frequency domain solutions are expanded in the

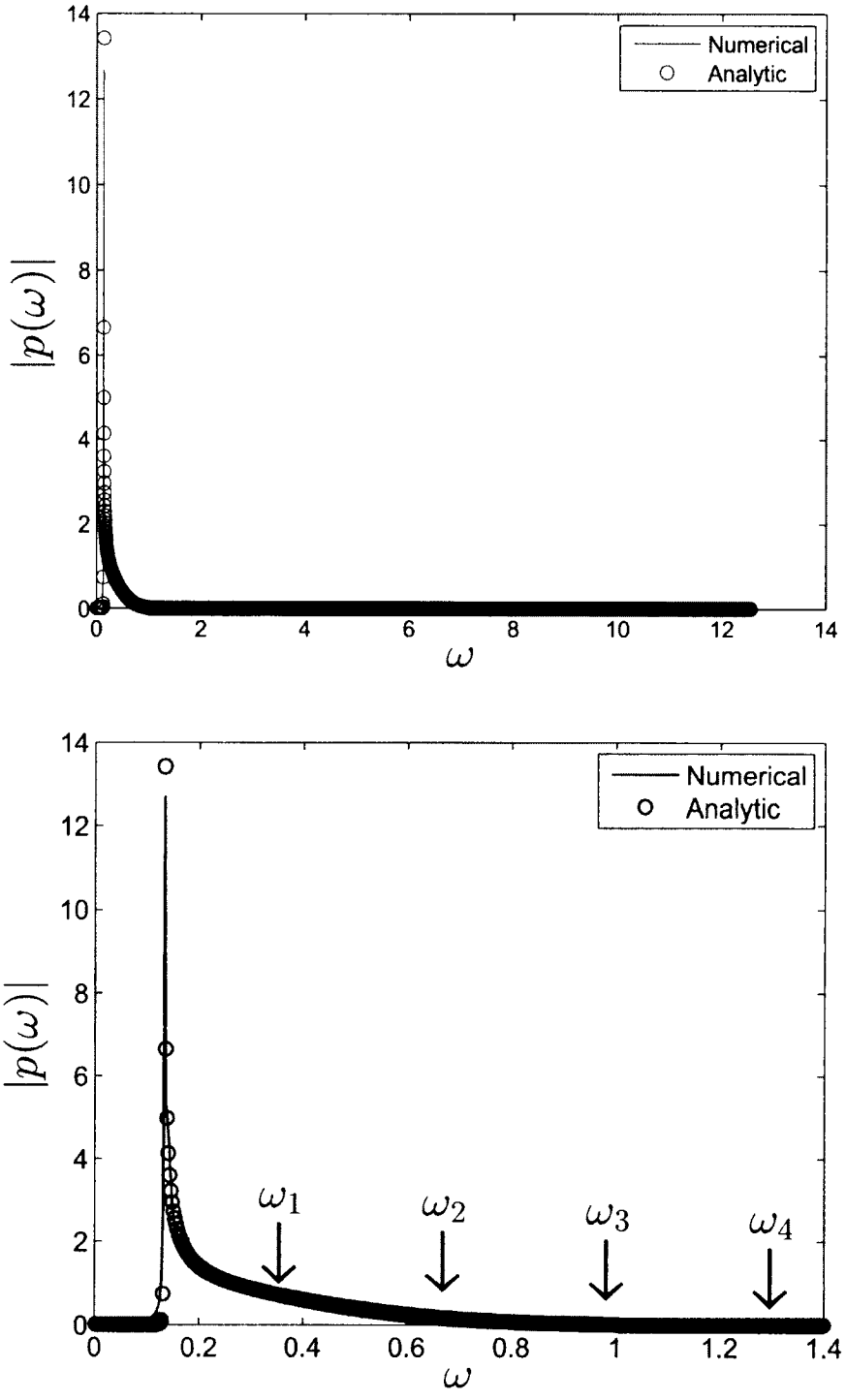

Fig. 15. A comparison between the analytic and numerical FFTs of a point at $(100, 0, 0)$ (top) and its scaled version with $\omega = [0, 1.4]$ (bottom).

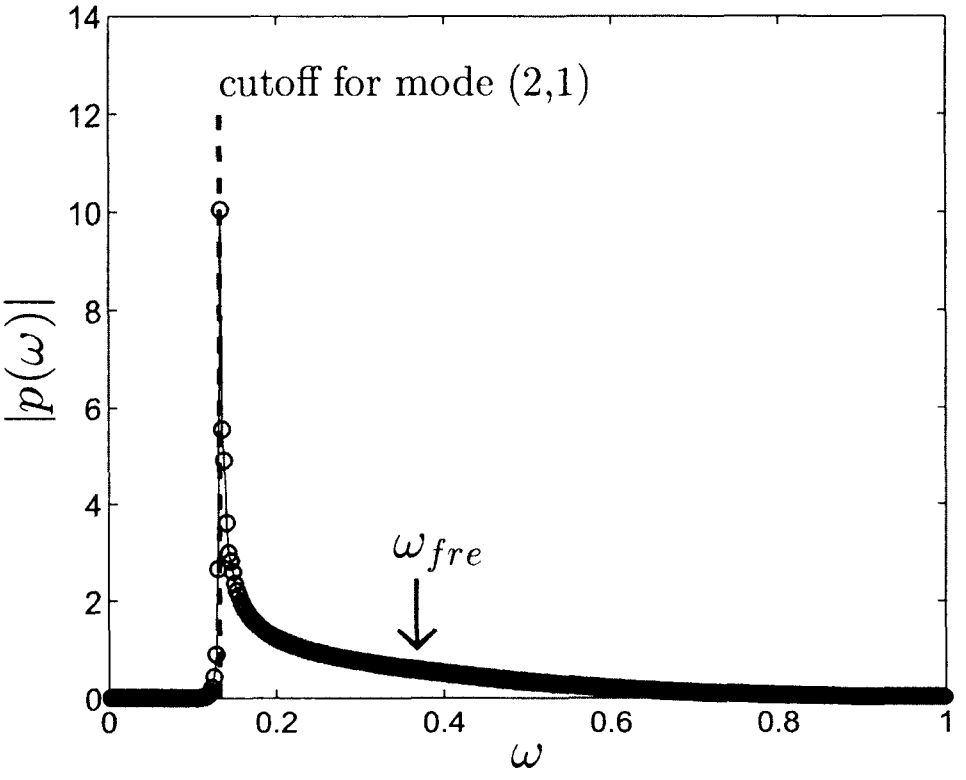

Fig. 16. FFT of the time signal shown in the Fig. 14 and cutoff frequency.

duct mode eigenfunction $\phi_{mn}(y,z)$:

$$\hat{p}_m(x,y,z,\omega) = \sum_{n=0}^{\infty} A_{mn}(x,\omega)\phi_{mn}(y,z) = \sum_{n=0}^{N_0} \left[A_{mn}^{+} e^{ik_{mn}^{+}x} + A_{mn}^{-} e^{ik_{mn}^{-}x} \right] \phi_{mn}(y,z),$$

$$\begin{aligned} \hat{u}_m(x,y,z,\omega) &= \sum_{n=0}^{\infty} B_{mn}(x,\omega)\phi_{mn}(y,z) \\ &= \sum_{n=0}^{N_0} \left[A_{mn}^{+} \frac{k_{mn}^{+}}{\omega - Mk_{mn}^{+}} e^{ik_{mn}^{+}x} + A_{mn}^{-} \frac{k_{mn}^{-}}{\omega - Mk_{mn}^{-}} e^{ik_{mn}^{-}x} \right] \phi_{mn}(y,z) \end{aligned}$$

where N_0 is the number of cut-on modes. By the orthogonality of $\phi_{mn}(y,z)$, we have

$$A_{mn}^{+} e^{ik_{mn}^{+}x} + A_{mn}^{-} e^{ik_{mn}x} = \frac{\int_{-L_z}^{L_z} \int_{-L_y}^{L_y} \hat{p}_m(x,y,z,\omega)\phi_{mn}(y,z)dydz}{\int_{-L_z}^{L_z} \int_{-L_y}^{L_y} \phi_{mn}^2(y,z)dydz}, \tag{38}$$

$$A^+_{mn}\frac{k^+_{mn}}{\omega - Mk^+_{mn}}e^{ik^+_{mn}x} + A^-_{mn}\frac{k^-_{mn}}{\omega - Mk^-_{mn}}e^{ik^-_{mn}x} = \frac{\int_{-L_z}^{L_z}\int_{-L_y}^{L_y}\hat{u}_m(x,y,z,\omega)\phi_{mn}(y,z)dydz}{\int_{-L_z}^{L_z}\int_{-L_y}^{L_y}\phi^2_{mn}(y,z)dydz}. \tag{39}$$

We can calculate double integrals in (38) and (39) over the computational grids in the y and z directions by numerical integration.

Finally, by solving (38) and (39), we can find A^+_{mn}, the amplitude of the duct mode (m,n) propagating in the direction of $+x$, and A^-_{mn}, the amplitude of the duct mode propagating in the direction of $-x$, as illustrated in Fig. 17.

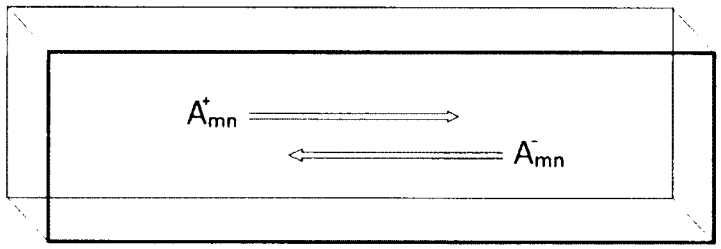

Fig. 17. Illustration of the right-going and left-going duct wave modes.

Simulations are carried out by the TDWP method with the symmetric eigenfunctions for the Mach numbers $M = 0$ and $M = 0.45$ inside a rectangular duct. One of these simulations is shown as the time history of the pressure at a point inside the duct in the numerical solution graph of Fig. 14. Solutions at $\omega_{fre} = 3\pi/25$ (shown in Fig. 16) are decomposed into cut-on duct modes at various x locations inside the duct. They are shown in Figs. 18 and 19 for $M = 0$ and $M = 0.45$, respectively. The top sub-figures show the amplitudes of right-going modes along the duct, the bottom sub-figures show the amplitudes of left-going modes. In these computations, mode $(2,1)$ is used and a source plane is located at $x_S = 0$. For Mach number $M = 0$, amplitudes of the right and left going modes are all equal. For an existing Mach number case $M = 0.45$, amplitudes of the right-going modes are equal to each other but greater than amplitudes of the left-going modes.

Modal decomposition results for the anti-symmetric eigenfunctions are also shown

in Figs. 20 and 21 for the same values of the parameters, the methods, and the domains that were used for the symmetric eigenfunctions. The same observations that were made with respect to the symmetric eigenfunctions can also be noticed in these figures.

The duct mode introduced at the source plane is not scattered into other modes as it travels through the uniform duct. These results confirm that the source function (25) is effective in forcing a wave packet that contains only the forced mode.

For the rest of the paper, we will use only the symmetric eigenfunctions for all computations and simulations.

3.6 ANALYSIS AND SUGGESTION FOR THE WIDTH OF THE SOURCE TERM IN (26)

As we make a modal decomposition at various x stations inside the duct, we see in Figs. 18 and 19 that the amplitudes of the cut-on duct modes at various stations inside the duct are at constant levels as expected. However, as frequency increases, it was found that the modal amplitudes reduced rapidly and became non-constant. In Fig. 22 at four different frequencies, we show A^{+}_{mn}, the amplitude of the right-going duct mode (m, n), at various stations. These frequencies are also implied at the bottom of the Fig. 15.

If we examine Figs. 15 and 16, it is seen that the $p(\omega)$ drops very fast. To understand reasons for this, the Fourier transform of $p_{mn}(x,t)$ can be examined below.

By (37), for $\lambda < \omega$ and $M = 0$, we get

$$\begin{aligned}
\tilde{p}(x,\omega) &= \int_{-\infty}^{\infty} \hat{p}(x,t) e^{-i\omega t} dt \\
&= \frac{1}{2c} \int_{-X}^{X} \int_{-T}^{T} \frac{-ie^{-i\bar{x}\sqrt{\omega^2-\lambda^2}}}{\sqrt{\omega^2-\lambda^2}} e^{-i\omega t'} \frac{D}{Dt'} \left[\Psi(t') e^{-\sigma x'^2} \right] dx' dt' \\
&= \frac{-i}{2c\sqrt{\omega^2-\lambda^2}} \int_{-\infty}^{\infty} \Psi'(t') e^{-i\omega t'} dt' \int_{-\infty}^{\infty} e^{-i\bar{x}\sqrt{\omega^2-\lambda^2}} e^{-\sigma x'^2} dx'.
\end{aligned}$$

By the transformation (36)

$$\bar{x} = \frac{|x - x'|}{\alpha^2 c} = x - x'$$

since now $x > x'$, $\alpha = 1$ and $c = 1$ for $M = 0$.

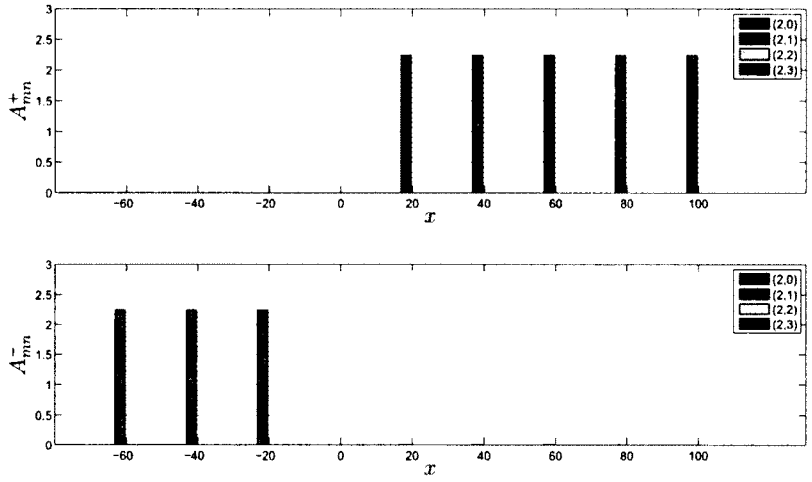

Fig. 18. The mode $(2, 1)$ and $M = 0$ by the symmetric eigenfunction.

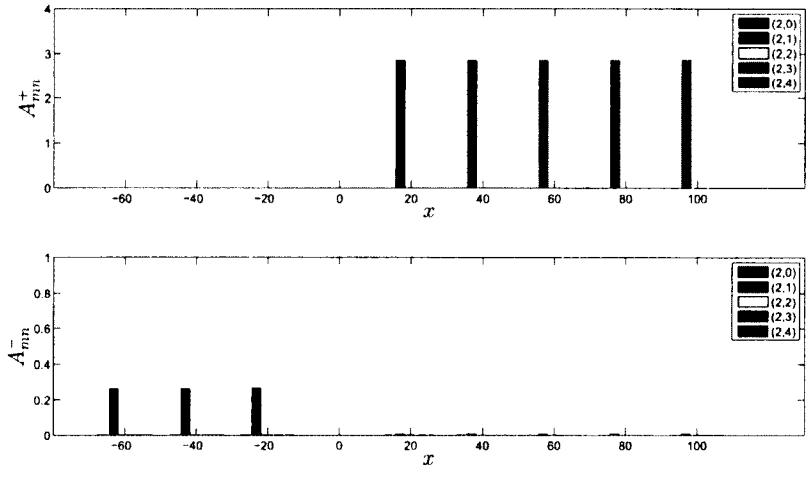

Fig. 19. The mode $(2, 1)$ and $M = 0.45$ by the symmetric eigenfunction.

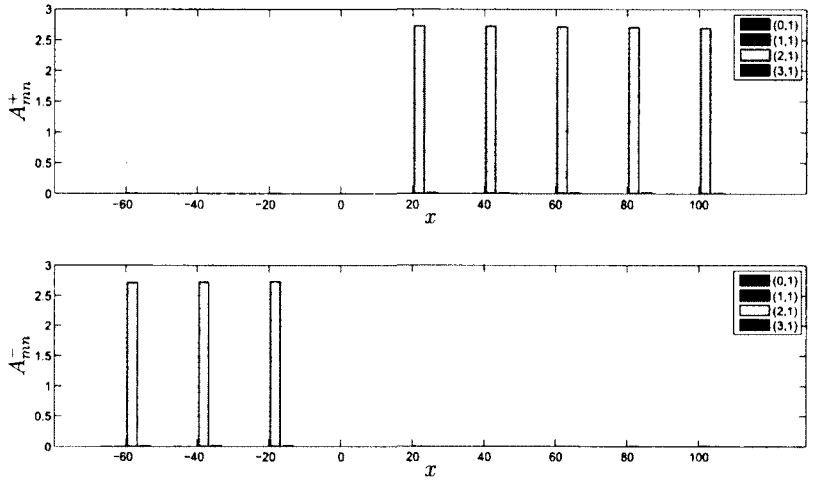

Fig. 20. The mode $(2,1)$ and $M = 0$ by the anti-symmetric eigenfunction.

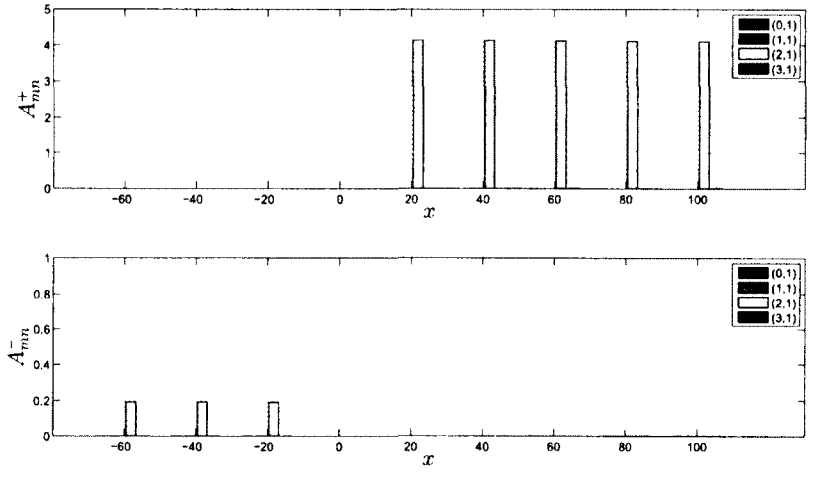

Fig. 21. The mode $(2,1)$ and $M = 0.45$ by the anti-symmetric eigenfunction.

We have

$$\tilde{p}(x,\omega) = \frac{-i}{2\sqrt{\omega^2-\lambda^2}}\mathcal{F}\left\{\Psi'(t')\right\}e^{-ix\sqrt{\omega^2-\lambda^2}}\int_{-\infty}^{\infty} e^{ix'\sqrt{\omega^2-\lambda^2}}e^{-\sigma x'^2}dx'$$
$$= \frac{-i}{2\sqrt{\omega^2-\lambda^2}}\mathcal{F}\left\{\Psi'(t')\right\}e^{-ix\sqrt{\omega^2-\lambda^2}}\mathcal{F}\left\{e^{-\sigma x'^2}\right\}_{(\sqrt{\omega^2-\lambda^2})}.$$

where $\mathcal{F}$ denotes the Fourier transform.
Since

$$\mathcal{F}\left\{\Psi'(t')\right\} = i\omega\Psi(\omega)$$

and

$$\mathcal{F}\left\{e^{-\sigma x'^2}\right\}_{(\sqrt{\omega^2-\lambda^2})} = \sqrt{\frac{\pi}{\sigma}}e^{-\frac{\omega^2-\lambda^2}{4\sigma}},$$

we have

$$\tilde{p}(x,\omega) = \frac{1}{2}\sqrt{\frac{\pi}{\sigma}}\frac{\omega}{\sqrt{\omega^2-\lambda^2}}\Psi(\omega)e^{-ix\sqrt{\omega^2-\lambda^2}}e^{-\frac{\omega^2-\lambda^2}{4\sigma}}.$$

If we take absolute of both sides, we have

$$|\tilde{p}(x,\omega)| = \frac{1}{2}\sqrt{\frac{\pi}{\sigma}}\frac{\omega}{\sqrt{\omega^2-\lambda^2}}\Psi(\omega)e^{-\frac{\omega^2-\lambda^2}{4\sigma}}.$$

It can be written as

$$|\tilde{p}(x,\omega)| = C\cdot\frac{\omega}{\sqrt{\omega^2-\lambda^2}}\cdot\Psi(\omega)\cdot e^{-\frac{\omega^2-\lambda^2}{4\sigma}} \tag{40}$$

where $C = \frac{1}{2}\sqrt{\frac{\pi}{\sigma}}$.
Equation (40) consists of three different functions and a constant. In Fig. 23, these functions are plotted separately.

The spectrum of the wave packet shown as $\Psi(\omega)$ equals one from the cutoff frequency (λ) and control parameter $\omega_0 = \pi/2$. The function $\frac{\omega}{\sqrt{\omega^2-\lambda^2}}$ approaches one as ω approaches ω_0. Therefore, the last exponential function is the reason for quick dropping. The σ is a key element in this function and given in (25) as

$$\sigma = \frac{\ln 2}{b^2}$$

where b is the half-width of the source function and $b = b_0\Delta x$ and $b_0 > 0$.
The results shown in Fig. 22 are obtained for $b = 5$. To show how the changes

in value of b effect the range of the useful frequency from cutoff frequency(λ) to $\omega_0 = \pi/2$, choose σ such that

$$e^{-\frac{\omega^2-\lambda^2}{4\sigma}} > k$$

where k is a positive real number. For accuracy in modal decomposition, k should not be a very small number for all frequencies of interest.
If we take the natural logarithmic function on both sides, we have

$$-\frac{\omega^2-\lambda^2}{4\sigma} > \ln k$$

then plug in $\sigma = \ln 2/b^2$, we get

$$b < \frac{2\sqrt{\ln 2 \ln(\frac{1}{k})}}{\sqrt{\omega^2-\lambda^2}}$$

or, equivalently

$$b_0\Delta x < \frac{2\sqrt{\ln 2 \ln(\frac{1}{k})}}{\sqrt{\omega^2-\lambda^2}}. \tag{41}$$

In Fig. 24, a graphic result of (41) for $k = 0.05$ is shown. Equation (41) and Fig. 24 shows the limit on the width of the source region.

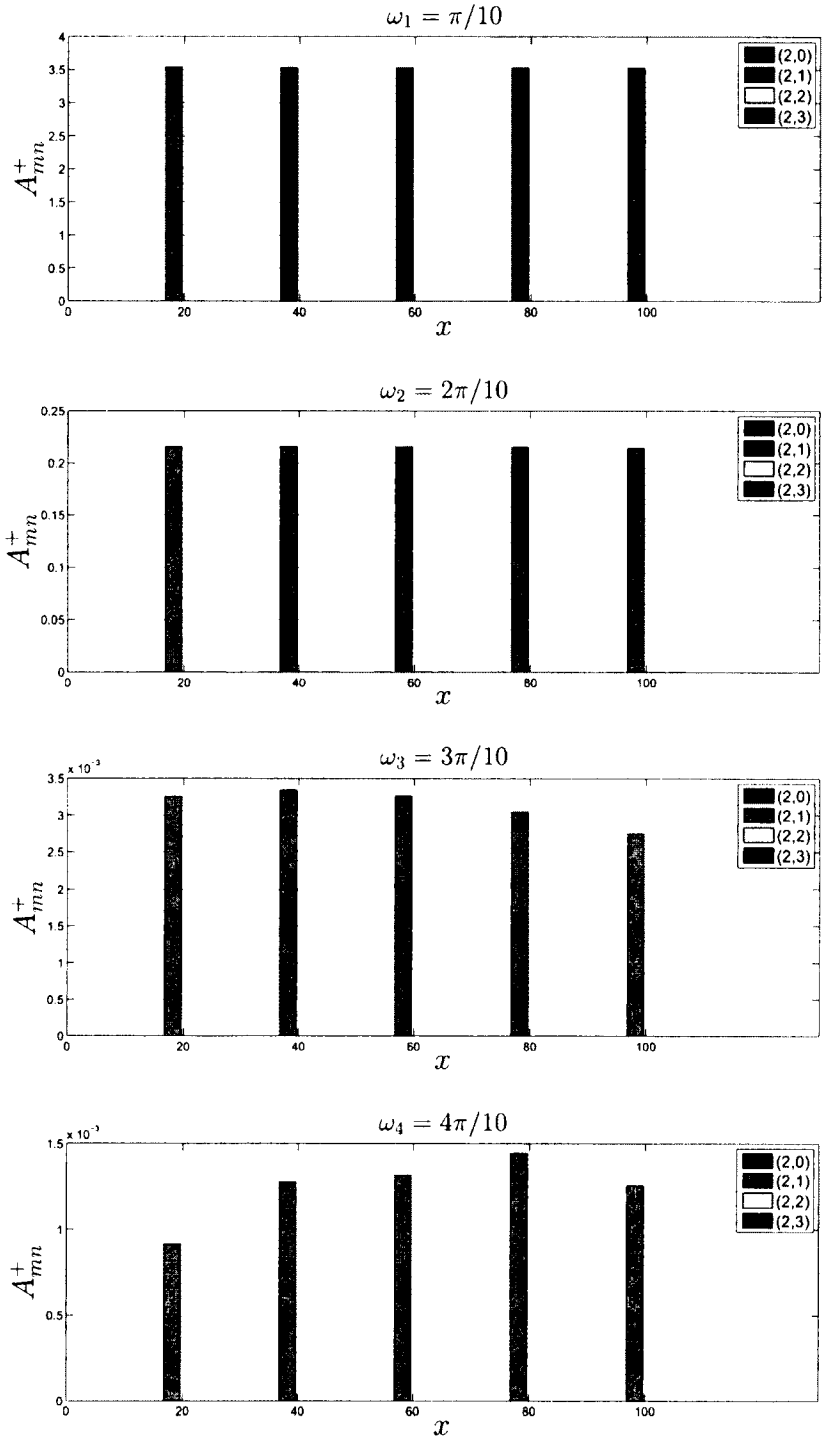

Fig. 22. Solutions at four different frequencies are decomposed into cut-on duct modes at selected x locations.

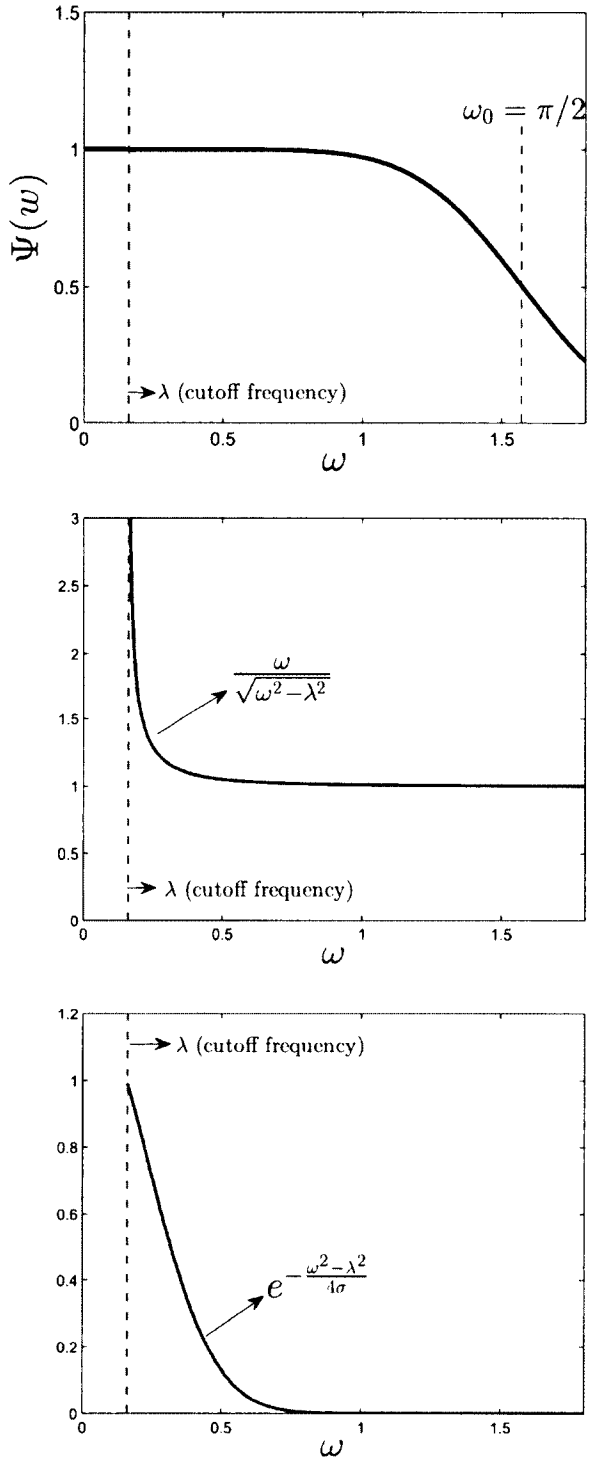

Fig. 23. Three functions vs. frequency, Top: The spectrum of the wave packet; Middle: A function; Bottom: An exponential function.

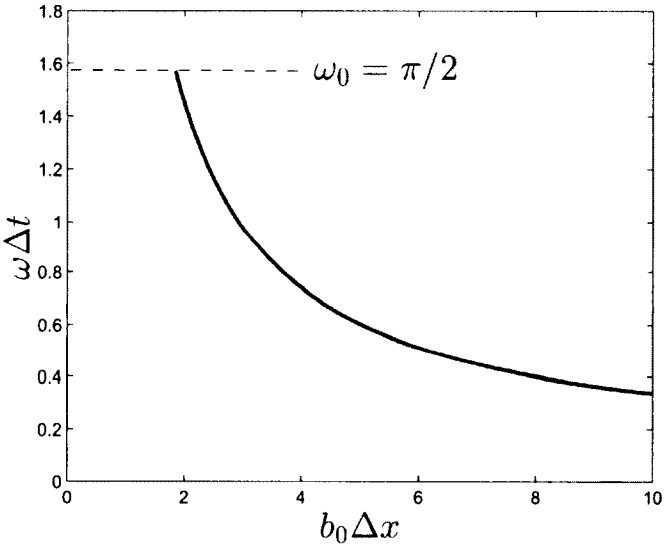

Fig. 24. A plot from the equation (41) for $k = 0.05$ showing the relation $b_0\Delta x$ vs. $\omega\Delta t$.

CHAPTER 4

ADJOINT SYSTEM

4.1 DERIVATION AND FORMULATION

In this section, we will construct the adjoint system for the time domain linearized Euler equations in the Cartesian coordinates in the presence of a non-uniform mean flow.

Let the adjoint system for (10) be written as

$$\frac{\partial \tilde{\boldsymbol{w}}}{\partial t} + \tilde{\boldsymbol{A}}\frac{\partial \tilde{\boldsymbol{w}}}{\partial x} + \tilde{\boldsymbol{B}}\frac{\partial \tilde{\boldsymbol{w}}}{\partial y} + \tilde{\boldsymbol{C}}\frac{\partial \tilde{\boldsymbol{w}}}{\partial z} + \tilde{\boldsymbol{D}}\tilde{\boldsymbol{w}} = 0 \tag{42}$$

and denoted as

$$\frac{\partial \tilde{\boldsymbol{w}}}{\partial t} + \tilde{\boldsymbol{L}}(\tilde{\boldsymbol{w}}) = 0.$$

A tilde " $\sim$ " will be used to indicate the variables associated with an adjoint system. Here, we define the adjoint system such that the following operation holds:

$$\begin{aligned} \tilde{\boldsymbol{w}}^T \left[\frac{\partial \boldsymbol{w}}{\partial t} + \boldsymbol{L}(\boldsymbol{w})\right] + \boldsymbol{w}^T \left[\frac{\partial \tilde{\boldsymbol{w}}}{\partial t} + \tilde{\boldsymbol{L}}(\tilde{\boldsymbol{w}})\right] &= \frac{\partial E}{\partial t} + \frac{\partial J_x}{\partial x} + \frac{\partial J_y}{\partial y} + \frac{\partial J_z}{\partial z} \\ &= \frac{\partial E}{\partial t} + \nabla \cdot \boldsymbol{J} \end{aligned} \tag{43}$$

where a superscript T denotes the vector transpose, and $E(\boldsymbol{w}, \tilde{\boldsymbol{w}})$ and $\boldsymbol{J}(\boldsymbol{w}, \tilde{\boldsymbol{w}}) = (J_x, J_y, J_z)$ are bi-linear functions of $\boldsymbol{w}$ and $\tilde{\boldsymbol{w}}$. For (43) to be valid, the adjoint system is obtained when

$$\tilde{\boldsymbol{A}} = \boldsymbol{A}^T,\ \tilde{\boldsymbol{B}} = \boldsymbol{B}^T,\ \tilde{\boldsymbol{C}} = \boldsymbol{C}^T,\ \tilde{\boldsymbol{D}} = \frac{\partial \boldsymbol{A}^T}{\partial x} + \frac{\partial \boldsymbol{B}^T}{\partial y} + \frac{\partial \boldsymbol{C}^T}{\partial z} - \boldsymbol{D}^T \tag{44}$$

with

$$E(\boldsymbol{w}, \tilde{\boldsymbol{w}}) = \tilde{\boldsymbol{w}}^T \boldsymbol{w} \tag{45}$$

and

$$\boldsymbol{J}(\boldsymbol{w}, \tilde{\boldsymbol{w}}) = \left(\tilde{\boldsymbol{w}}^T \boldsymbol{A}\boldsymbol{w}, \tilde{\boldsymbol{w}}^T \boldsymbol{B}\boldsymbol{w}, \tilde{\boldsymbol{w}}^T \boldsymbol{C}\boldsymbol{w}\right). \tag{46}$$

The flux vector $\boldsymbol{J}$ is also found easily, which is of the form

$$\boldsymbol{J} = (J_x, J_y, J_z) = \left(\tilde{\boldsymbol{w}}^T \cdot \boldsymbol{w}\right) \bar{\boldsymbol{u}} + \left(\bar{\rho}\tilde{\rho} + \gamma\bar{p}\tilde{p}\right) \boldsymbol{u}' + \frac{1}{\bar{\rho}} p' \tilde{\boldsymbol{u}}.$$

We can write matrix components of adjoint system (42) expressed in (44) as

$$\tilde{\boldsymbol{w}} = \begin{pmatrix} \tilde{\rho} \\ \tilde{u}_x \\ \tilde{u}_y \\ \tilde{u}_z \\ \tilde{p} \end{pmatrix}, \tilde{\boldsymbol{A}} = \begin{pmatrix} \bar{u}_x & 0 & 0 & 0 & 0 \\ \bar{\rho} & \bar{u}_x & 0 & 0 & \gamma\bar{p} \\ 0 & 0 & \bar{u}_x & 0 & 0 \\ 0 & 0 & 0 & \bar{u}_x & 0 \\ 0 & \frac{1}{\bar{\rho}} & 0 & 0 & \bar{u}_x \end{pmatrix}, \tilde{\boldsymbol{B}} = \begin{pmatrix} \bar{u}_y & 0 & 0 & 0 & 0 \\ 0 & \bar{u}_y & 0 & 0 & 0 \\ \bar{\rho} & 0 & \bar{u}_y & 0 & \gamma\bar{p} \\ 0 & 0 & 0 & \bar{u}_y & 0 \\ 0 & 0 & \frac{1}{\bar{\rho}} & 0 & \bar{u}_y \end{pmatrix}.$$

$$\tilde{\boldsymbol{C}} = \begin{pmatrix} \bar{u}_z & 0 & 0 & 0 & 0 \\ 0 & \bar{u}_z & 0 & 0 & 0 \\ 0 & 0 & \bar{u}_z & 0 & 0 \\ \bar{\rho} & 0 & 0 & \bar{u}_z & \gamma\bar{p} \\ 0 & 0 & 0 & \frac{1}{\bar{\rho}} & \bar{u}_z \end{pmatrix},$$

$$\tilde{\boldsymbol{D}} = \begin{pmatrix} 0 & 0 & 0 & 0 & 0 \\ 0 & \frac{\partial \bar{u}_y}{\partial y} + \frac{\partial \bar{u}_z}{\partial z} & -\frac{\partial \bar{u}_y}{\partial x} & -\frac{\partial \bar{u}_z}{\partial x} & (\gamma-1)\frac{\partial \bar{p}}{\partial x} \\ 0 & -\frac{\partial \bar{u}_x}{\partial y} & \frac{\partial \bar{u}_x}{\partial x} + \frac{\partial \bar{u}_z}{\partial z} & -\frac{\partial \bar{u}_z}{\partial y} & (\gamma-1)\frac{\partial \bar{p}}{\partial y} \\ 0 & -\frac{\partial \bar{u}_x}{\partial z} & \frac{\partial \bar{u}_y}{\partial z} & \frac{\partial \bar{u}_x}{\partial x} + \frac{\partial \bar{u}_y}{\partial y} & (\gamma-1)\frac{\partial \bar{p}}{\partial z} \\ 0 & \frac{\partial(\frac{1}{\bar{\rho}})}{\partial x} + \frac{1}{\gamma\bar{\rho}\bar{p}}\frac{\partial \bar{p}}{\partial x} & \frac{\partial(\frac{1}{\bar{\rho}})}{\partial y} + \frac{1}{\gamma\bar{\rho}\bar{p}}\frac{\partial \bar{p}}{\partial y} & \frac{\partial(\frac{1}{\bar{\rho}})}{\partial z} + \frac{1}{\gamma\bar{\rho}\bar{p}}\frac{\partial \bar{p}}{\partial z} & (1-\gamma)(\nabla \cdot \bar{\boldsymbol{u}}) \end{pmatrix}.$$

Note that the adjoint system as defined in (42) is assumed to be non-zero for $t < t'$ where t' is a bound for the time of interest in the Euler forward problem. The numerical solution of the adjoint system may be computed in a time marching fashion in a reversed time variable $\tau = t' - t$. It leads to

$$\frac{\partial \tilde{\boldsymbol{w}}}{\partial \tau} - \tilde{\boldsymbol{L}}(\tilde{\boldsymbol{w}}) = 0. \tag{47}$$

The adjoint system will also be referred to as the backward problem in this thesis.

4.2 EIGENVALUES AND EIGENFUNCTIONS OF THE ADJOINT SYSTEM AND DISPERSION RELATION FOR A UNIFORM MEAN FLOW

We first analyze the eigenvalues and eigenfunctions associated with the adjoint system and the dispersion relations of the linear waves for the uniform mean flow. The adjoint system can be simplified for the uniform mean flow. The complete simplified adjoint equations are

$$\frac{\partial \tilde{\rho}}{\partial t} + \bar{u}_x \frac{\partial \tilde{\rho}}{\partial x} + \bar{u}_y \frac{\partial \tilde{\rho}}{\partial y} + \bar{u}_z \frac{\partial \tilde{\rho}}{\partial z} = 0, \tag{48}$$

$$\frac{\partial \tilde{u}_x}{\partial t} + \bar{u}_x \frac{\partial \tilde{u}_x}{\partial x} + \bar{u}_y \frac{\partial \tilde{u}_x}{\partial y} + \bar{u}_z \frac{\partial \tilde{u}_x}{\partial z} + \bar{\rho} \frac{\partial \tilde{\rho}}{\partial x} + \gamma \bar{p} \frac{\partial \tilde{p}}{\partial x} = 0, \tag{49}$$

$$\frac{\partial \tilde{u}_y}{\partial t} + \bar{u}_x \frac{\partial \tilde{u}_y}{\partial x} + \bar{u}_y \frac{\partial \tilde{u}_y}{\partial y} + \bar{u}_z \frac{\partial \tilde{u}_y}{\partial z} + \bar{\rho} \frac{\partial \tilde{\rho}}{\partial y} + \gamma \bar{p} \frac{\partial \tilde{p}}{\partial y} = 0, \tag{50}$$

$$\frac{\partial \tilde{u}_z}{\partial t} + \bar{u}_x \frac{\partial \tilde{u}_z}{\partial x} + \bar{u}_y \frac{\partial \tilde{u}_z}{\partial y} + \bar{u}_z \frac{\partial \tilde{u}_z}{\partial z} + \bar{\rho} \frac{\partial \tilde{\rho}}{\partial z} + \gamma \bar{p} \frac{\partial \tilde{p}}{\partial z} = 0, \tag{51}$$

$$\frac{\partial \tilde{p}}{\partial t} + \bar{u}_x \frac{\partial \tilde{p}}{\partial x} + \bar{u}_y \frac{\partial \tilde{p}}{\partial y} + \bar{u}_z \frac{\partial \tilde{p}}{\partial z} + \frac{1}{\bar{\rho}} \left(\frac{\partial \tilde{u}_x}{\partial x} + \frac{\partial \tilde{u}_y}{\partial y} + \frac{\partial \tilde{u}_z}{\partial z} \right) = 0. \tag{52}$$

It is obvious that this system is not the same as the linearized Euler equations given in (10). However, the eigen-solutions of the two formulations are closely related. In order to express this relation, we can define $\tilde{\rho}', \tilde{u}'_x, \tilde{u}'_y, \tilde{u}_z, \tilde{p}'$ that satisfy the Euler equation as

$$\tilde{\rho}' = \bar{\rho}\tilde{p} + \tilde{\rho},\ \tilde{u}'_x = \frac{1}{\bar{\rho}}\tilde{u}_x,\ \tilde{u}'_y = \frac{1}{\bar{\rho}}\tilde{u}_y,\ \tilde{u}'_z = \frac{1}{\bar{\rho}}\tilde{u}_z,\ \tilde{p}' = \gamma\bar{p}\tilde{p} + \bar{\rho}\tilde{\rho}.$$

In particular, there is a simple relation for the acoustic solutions. If u_a, v_a, w_a and p_a represent an acoustic solution of the Euler system, then the corresponding adjoint solution for (48)-(52) is given by

$$(\tilde{\rho}, \tilde{u}_x, \tilde{u}_y, \tilde{u}_z, \tilde{p}) = (0, \bar{\rho}u_a, \bar{\rho}v_a, \bar{\rho}w_a, \frac{1}{\gamma\bar{p}}p_a). \tag{53}$$

This solution will be referred to as the adjoint acoustic wave. For the adjoint acoustic waves, with $\tilde{\rho} = 0$, the equations for $\tilde{p}$ by (48)-(52) is

$$\left(\frac{\partial}{\partial t} + \bar{u}_x \frac{\partial}{\partial x} + \bar{u}_y \frac{\partial}{\partial y} + \bar{u}_z \frac{\partial}{\partial z} \right)^2 \tilde{p} - \bar{a}^2 \nabla^2 \tilde{p} = 0$$

where

$$\bar{a}^2 = \frac{\gamma \bar{p}}{\bar{\rho}}.$$

Since this equation is definitely the acoustic wave equation with a uniform mean flow, eigenvalues and eigenfunctions of adjoint acoustic wave are the same as those of the Euler equations under similar boundary conditions. From the same point of view, we can say that the dispersion relations for the linear acoustic waves of the adjoint system in a uniform mean flow will be identical to that of the Euler equations.

4.3 ORTHOGONALITY OF EIGENFUNCTIONS

In this section, we show that the eigenfunctions of the Euler and adjoint systems are orthogonal. This orthogonality will be useful in deriving the reciprocal relations between these two systems. We can begin with the Lagrange identity already given by (43) as

$$\frac{\partial E(\boldsymbol{w}, \tilde{\boldsymbol{w}})}{\partial t} + \nabla \cdot \boldsymbol{J}(\boldsymbol{w}, \tilde{\boldsymbol{w}}) = 0 \tag{54}$$

where $E(\boldsymbol{w}, \tilde{\boldsymbol{w}})$ and $\boldsymbol{J}(\boldsymbol{w}, \tilde{\boldsymbol{w}})$ are given in (45)-(46). If Lagrange's identity is integrated over a bounded region, then the divergence theorem can be used. Firstly, consider a region with uniform mean flow and constant cross section D as shown in Fig. 25.

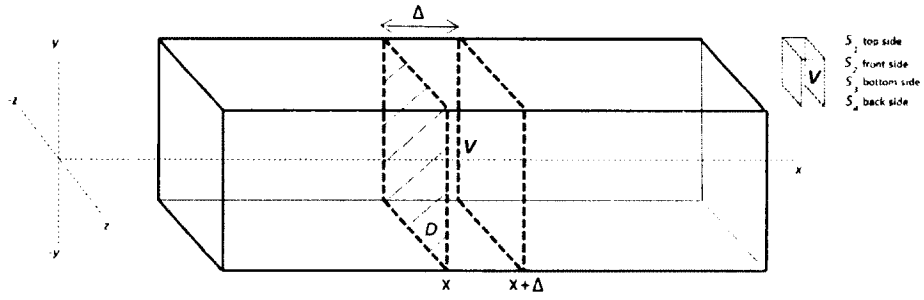

Fig. 25. A duct with uniform cross section and a rectangular prism inside.

Secondly, integrate (54) over a volume $V = [x, x + \Delta] \times D$ formed between two cross

section at x and $x+\Delta$,

$$\frac{\partial}{\partial t}\int_V E(\boldsymbol{w},\tilde{\boldsymbol{w}})dV + \int_V \nabla\cdot\boldsymbol{J}(\boldsymbol{w},\tilde{\boldsymbol{w}})dV = 0.$$

By the divergence theorem, the equation becomes

$$\frac{\partial}{\partial t}\int_V E(\boldsymbol{w},\tilde{\boldsymbol{w}})dV + \int_{\partial V} \boldsymbol{J}(\boldsymbol{w},\tilde{\boldsymbol{w}})\cdot\boldsymbol{n}dS = 0$$

where ∂V is the surface enclosing V and $\boldsymbol{n}$ is the normal vector outward from V. Since the boundary of V consists of the cross sections at x and $x+\Delta$ and duct side wall $S = S_1 \cup S_2 \cup S_3 \cup S_4$, we have

$$\frac{\partial}{\partial t}\int_V E(\boldsymbol{w},\tilde{\boldsymbol{w}})dV + \int_S \boldsymbol{J}(\boldsymbol{w},\tilde{\boldsymbol{w}})\cdot\boldsymbol{n}dS - \int_{D_x} J_x(\boldsymbol{w},\tilde{\boldsymbol{w}})dS + \int_{D_{x+\Delta}} J_x(\boldsymbol{w},\tilde{\boldsymbol{w}})dS = 0 \tag{55}$$

where J_x is the $x-$ component of the $\boldsymbol{J}$ vector given in (46), and D_x and $D_{x+\Delta}$ denote the cross sections located at x and $x+\Delta$ respectively.
The integration for the side walls can be written as

$$\begin{aligned}\int_S \boldsymbol{J}(\boldsymbol{w},\tilde{\boldsymbol{w}})\cdot\boldsymbol{n}dS = &\int_{S_1} J_y(\boldsymbol{w},\tilde{\boldsymbol{w}})dS - \int_{S_3} J_y(\boldsymbol{w},\tilde{\boldsymbol{w}})dS \\ &+ \int_{S_2} J_z(\boldsymbol{w},\tilde{\boldsymbol{w}})dS - \int_{S_4} J_z(\boldsymbol{w},\tilde{\boldsymbol{w}})dS.\end{aligned}$$

We know that S_1, S_2, S_3 and S_4 are solid walls. We have boundary conditions for velocity components at solid walls as

$$\begin{aligned}\tilde{u}_y &= 0 \quad \text{at} \quad S_1 \text{ and } S_3, \\ \tilde{u}_z &= 0 \quad \text{at} \quad S_2 \text{ and } S_4.\end{aligned}$$

On these solid walls by using the normal flux expression given in (46) and by applying above boundary conditions, we can get

$$\begin{aligned}\int_{S_1} J_y(\boldsymbol{w},\tilde{\boldsymbol{w}})dS &= \int_{S_1} \tilde{\boldsymbol{w}}^T\boldsymbol{B}\boldsymbol{w}dS = 2\int_{S_1}\tilde{p}\tilde{u}_y dS = 0, \\ \int_{S_2} J_z(\boldsymbol{w},\tilde{\boldsymbol{w}})dS &= \int_{S_2} \tilde{\boldsymbol{w}}^T\boldsymbol{C}\boldsymbol{w}dS = 2\int_{S_2}\tilde{p}\tilde{u}_z dS = 0, \\ \int_{S_3} J_y(\boldsymbol{w},\tilde{\boldsymbol{w}})dS &= \int_{S_3} \tilde{\boldsymbol{w}}^T\boldsymbol{B}\boldsymbol{w}dS = 2\int_{S_3}\tilde{p}\tilde{u}_y dS = 0, \\ \int_{S_4} J_z(\boldsymbol{w},\tilde{\boldsymbol{w}})dS &= \int_{S_4} \tilde{\boldsymbol{w}}^T\boldsymbol{C}\boldsymbol{w}dS = 2\int_{S_4}\tilde{p}\tilde{u}_z dS = 0.\end{aligned}$$

Therefore, on duct side walls, we have

$$\int_S \boldsymbol{J}(\boldsymbol{w}, \tilde{\boldsymbol{w}}) \cdot \boldsymbol{n} dS = 0$$

where $S = S_1 \cup S_2 \cup S_3 \cup S_4$.

By the above result, the equation (55) becomes

$$\frac{\partial}{\partial t} \int_V E(\boldsymbol{w}, \tilde{\boldsymbol{w}}) dV - \int_{D_x} J_x(\boldsymbol{w}, \tilde{\boldsymbol{w}}) dS + \int_{D_{x+\Delta}} J_x(\boldsymbol{w}, \tilde{\boldsymbol{w}}) dS = 0.$$

If we divide both sides of the equation above by Δ, then we get

$$\frac{\frac{\partial}{\partial t} \int_V E(\boldsymbol{w}, \tilde{\boldsymbol{w}}) dV}{\Delta} + \frac{\int_{D_{x+\Delta}} J_x(\boldsymbol{w}, \tilde{\boldsymbol{w}}) dS - \int_{D_x} J_x(\boldsymbol{w}, \tilde{\boldsymbol{w}}) dS}{\Delta} = 0.$$

By using the limit definition of a derivative and taking a limit of $\Delta \to 0$, we get a conservation statement

$$\frac{\partial}{\partial t} \left[\int_D E(\boldsymbol{w}, \tilde{\boldsymbol{w}}) dS \right] + \frac{\partial}{\partial x} \left[\int_D \boldsymbol{J}_x(\boldsymbol{w}, \tilde{\boldsymbol{w}}) dS \right] = 0. \tag{56}$$

Now we consider eigenfunctions of the Euler system and adjoint system of the form

$$\boldsymbol{w}(x, y, z, t) = \phi(k, y, z, \omega) e^{ikx - i\omega t} \tag{57}$$

and

$$\tilde{\boldsymbol{w}}(x, y, z, t) = \tilde{\phi}(\tilde{k}, y, z, \tilde{\omega}) e^{i\tilde{k}x - i\tilde{\omega}t}. \tag{58}$$

in which ω is the frequency and k is the wave number in the x direction, where a dispersion relation of $k = k(\omega)$ is assumed. $\phi(k, y, z, \omega)$ and $\tilde{\phi}(\tilde{k}, y, z, \tilde{\omega})$ are the mode shape functions. Both of the above, as well as their complex conjugates satisfy the homogeneous system of equations (10) and (42). By substituting (57) and (58) into (56), we get

$$\frac{\partial}{\partial t} \int_D E(\phi, \tilde{\phi}^*) e^{i(k - \tilde{k}^*)x - i(\omega - \tilde{\omega}^*)t} dS + \frac{\partial}{\partial x} \int_D J_x(\phi, \tilde{\phi}^*) e^{i(k - \tilde{k}^*)x - i(\omega - \tilde{\omega}^*)t} dS = 0.$$

After taking derivatives and making simplifications, we have

$$-i(\omega - \tilde{\omega}^*) \frac{\partial}{\partial t} \int_D E(\phi, \tilde{\phi}^*) dS + i(k - \tilde{k}^*) \frac{\partial}{\partial x} \int_D J_x(\phi, \tilde{\phi}^*) dS = 0. \tag{59}$$

For the actual frequencies, ω and $\tilde{\omega}$ are real numbers, then the above becomes

$$\left[k(\omega) - \tilde{k}^*(\omega) \right] \int_D J_x(\phi, \tilde{\phi}^*) dS = 0.$$

It follows that

$$\int_D J_x(\phi, \tilde{\phi}^*) dS = 0, \quad \text{if} \quad k(\omega) \neq \tilde{k}^*(\omega). \tag{60}$$

To express this condition using the expression for J_x given in (46), we have

$$\int_D \tilde{\phi}^{*T} \boldsymbol{A} \phi \, dS = 0, \quad \text{if} \quad k(\omega) \neq \tilde{k}^*(\omega). \tag{61}$$

Therefore, we find that the eigenfunctions (mode shapes) of the Euler and adjoint systems corresponding to different eigenvalues are orthogonal in the sense of (60). The orthogonality condition (61) given explicitly is

$$\int_D \tilde{\phi}^{*T} \boldsymbol{A} \phi \, dS = \int_D \left[\bar{u}_x \left(\tilde{\phi}^*_u \phi_u + \tilde{\phi}^*_v \phi_v + \tilde{\phi}^*_w \phi_w + \tilde{\phi}^*_p \phi_p \right) + \gamma \bar{p} \tilde{\phi}^*_p \phi_u + \frac{1}{\bar{\rho}} \tilde{\phi}^*_u \phi_p \right] dS = 0 \tag{62}$$

if $k(\omega) \neq \tilde{k}^*(\omega)$ where the subscript indicates the corresponding components of the eigenfunction ϕ and $\tilde{\phi}$.

4.4 NUMERICAL RESULTS OF THE ADJOINT SYSTEM

We present numerical results of the adjoint system. For all computations, the Dispersion Relation Preserving (DRP) scheme [48] and the Low Dissipation and Low Dispersion Runge-Kutta scheme (LDDRK 56) [23] is used to solve the adjoint system. At all the non-reflecting boundaries, Perfectly Matched Layer (PML) absorbing boundary conditions [22, 21, 31] are applied. Schematics of the rectangular duct computational domain for the adjoint system is shown in Fig. 26. We use the same computational domains of the Euler system for the adjoint system. This is shown in Fig. 26. Here, the source plane is located at $x_S = 50$. We need to mention that mean flow of the adjoint problem inside the duct is in the direction of $-x$ from right to left since we use the adjoint system in reversed time as defined in (47). By the same logic, we define $\tilde{A}^+_{mn}$ as the amplitude of the duct mode (m, n) propagating in the direction of $-x$, and $\tilde{A}^-_{mn}$ as the amplitude of duct mode propagating in the direction of $+x$.

TDWP simulations are carried out for the adjoint problem under the same boundary conditions of the forward problem. At all the non-reflecting boundaries, right-going and left-going waves are numerically absorbed by the PML without any visible reflection. Mode $(2, 1)$ is used as a forced mode for computations.

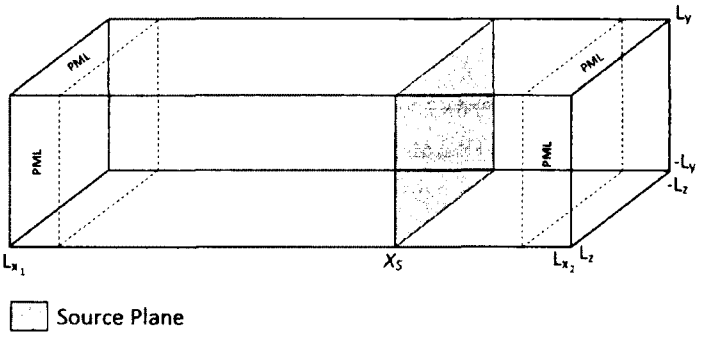

Fig. 26. Shematic of the rectangular computational domain for adjoint system.

As in section 3.5, solutions at a chosen frequency are decomposed into cut-on modes at various x locations inside the duct. These modal decomposition results are shown in Figs. 27 and 28 for $M = 0$ and $M = 0.45$, respectively. We show the amplitudes of left-going modes called $\tilde{A}^{+}_{mn}$ on the top sub-figures and the amplitudes of right-going modes called $\tilde{A}^{-}_{mn}$ on the bottom sub-figures.

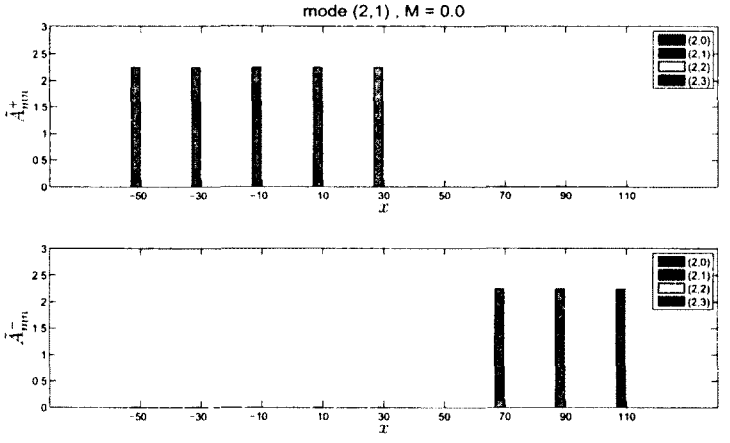

Fig. 27. The mode $(2, 1)$ and $M = 0$ for the adjoint system.

Again, we observe that amplitudes of the modes are constant as they propagate in the uniform duct as expect. This confirms again that the duct modes are imposed correctly.

In this chapter, the adjoint system for the linearized Euler equations was constructed in matrix form. The derivations were made using Cartesian coordinates

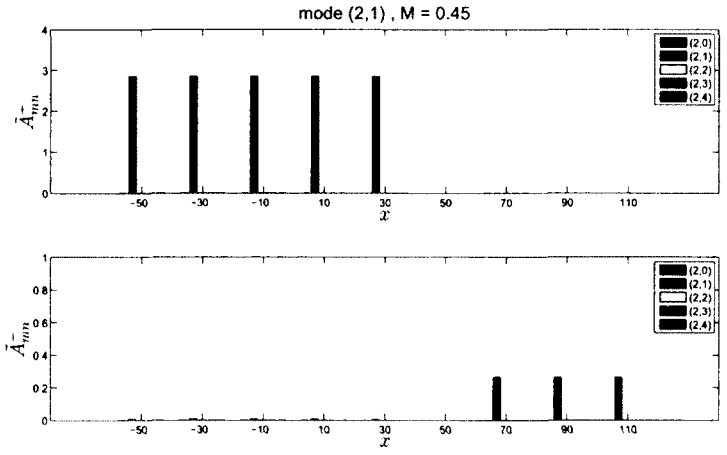

Fig. 28. The mode $(2, 1)$ and $M = 0.45$ for the adjoint system.

with the presence of a non-uniform mean flow. For an axially uniform mean flow, we analyzed the eigenvalues and eigenfunctions of the adjoint system and the dispersion relation of the linear waves. A simple relation for the acoustic solutions between the adjoint system and the Euler equations is shown for the axial uniform mean flow. We also showed that the eigenfunctions of the Euler and adjoint system are orthogonal which will be used to derive reciprocal relations between both systems in Chapter 7. Simulations for the adjoint system were carried out by the TDWP method in a uniform rectangular duct with solid walls. We also confirmed that by using the results shown for amplitudes of the cut-on duct modes for $M = 0$ and $M = 0.45$, the imposition of the forced modes into the adjoint system was successful.

CHAPTER 5

APPLICATION OF THE TDWP METHOD TO NON-UNIFORM DUCTS

In this chapter, the methods and analysis developed in the previous chapter will be applied to non-uniform ducts with non-uniform mean flows.

5.1 THE AREA-MACH NUMBER RELATION

In compressible flow theory, a parameter that is fundamental is the *speed of sound*, c. Its relation to the compressibility of the fluid is given by

$$c^2 = \left(\frac{\partial p}{\partial \rho}\right)_s$$

where p is the pressure and ρ is the density and the derivative is taken adiabatically, that is, at constant entropy per particle (s).

The speed of sound is a significant measure of the effects of compressibility when it is compared to the speed of the flow. This introduces a dimensionless parameter which is called the Mach number,

$$M = u/c.$$

The Mach number is an important parameter in the study of compressible flow theory. Much of the analysis will appear in terms of the Mach number in the development of the equations of motion of a compressible fluid. For the purposes of computing the Mach number M, the process is assumed to be isentropic. For the uniform mean flow in a uniform duct, M is constant everywhere. For the nonuniform duct, M will vary from point to point in a given flow. In this section, we will introduce a relation between the area A and the Mach number M that will be used to compute the non-uniform mean flow for ducts of non-uniform cross sections [25, 30]. In order to get this relation we use another relation that is the area-velocity relation. This relation can be simply demonstrated by considering a one-dimensional isentropic flow through a varying area channel as shown in Fig. 29.

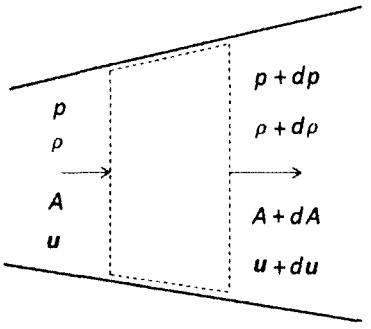

Fig. 29. A varying area channel.

The area-velocity relation is derived by combining the continuity and momentum equations and using the definition of the speed of sound for isentropic flow. In [30], it is given as

$$\frac{dA}{A} = -(1 - M^2)\frac{du}{u}. \tag{63}$$

It is easy to see that how area changes effect flow properties at where $M = 0$, at subsonic speeds ($0 < M < 1$) and at supersonic speeds ($1 < M$). What remains is the question of what happens at sonic speed, $M = 1$. Consider a tube in which the velocity increases continuously from subsonic to supersonic. The formula (63) shows that the tube must converge in the subsonic and diverge in the supersonic portion. It also needs to go through $M = 1$ since it is from subsonic to supersonic. Just at $M = 1$ there must be a throat. If the same argument applies to the case where the velocity decreases continuously from supersonic to subsonic, then we get the important conclusion that $M = 1$ can be attained only at a throat of the tube. It can be shown mathematically, by plugging $M = 1$ into the equation (63), and du/u can be finite, only if $dA/A = 0$. It is possible where the area attains a maximum or a minimum (see Fig. 30).

For the maximum area, if the incoming flow has $M < 1$, then M gets smaller or if $M > 1$, then M gets bigger as flow is transiting. Then, since we never get $M = 1$ for the maximum area, we need a throat to transition. The sonic condition attained at this throat is very useful here. In order to find the area-Mach number relation for

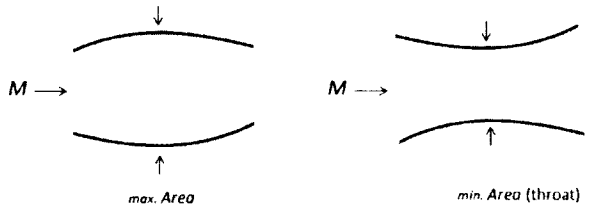

Fig. 30. Left: A maximum area and incoming flow with a Mach number M. Right: A minimum area that is called throat and incoming flow with a Mach number M.

an isentropic flow, we use a point where $M = 1$, that is, a throat as shown in Fig. 30. We denote this area as A^* and Mach number $M^* = 1$ and also consider another cross-sectional area A associated with Mach number M. They are shown in Fig. 31.

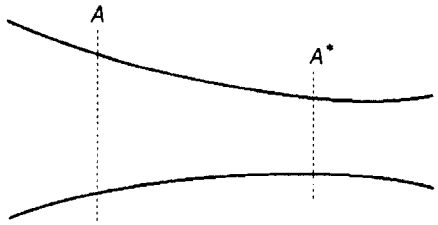

Fig. 31. Two cross-sectional areas A and A^*.

By using mass conservation, the mass flow rate at area A is equal to the mass flow rate at A^*, the relation between the area and Mach number can be found [25, 30]. Here, the mass flow rate at a flow cross-sectional area A is expressed in terms of stagnation of pressure and temperature. For a perfect gas in [25], the area-Mach number relation is given as

$$\frac{A}{A^*} = \frac{1}{M}\left(\frac{1+\frac{\gamma-1}{2}M^2}{\frac{\gamma+1}{2}}\right)^{\frac{\gamma+1}{2(\gamma-1)}} \tag{64}$$

where $\gamma = 1.4$ for air and M is the Mach number at area A.

For each value of A/A^*, there are two possible isentropic solutions, one subsonic and

the other supersonic. Equation (64) will be used to compute the mean flow in a non-uniform duct.

5.2 NON-UNIFORM DUCT AND ITS COMPUTATIONAL DOMAIN

In this section, we will define a non-uniform duct and its computational domain. We will map a physical domain of non-uniform duct to a uniform computational domain to apply a finite difference scheme to the linearized Euler equations and its adjoint system in the Cartesian coordinates. This can be achieved by using the coordinate transformation which represents a transformation from the physical to the computational coordinates. Firstly, we will work over the 2-D case to show this transformation and other relations clearly. Later, the actual 3-D non-uniform duct will be discussed.

We consider a non-uniform duct as shown in Fig. 32, with a region of slowly varying duct area in the middle and uniform parts at the beginning and at the ending of the duct.

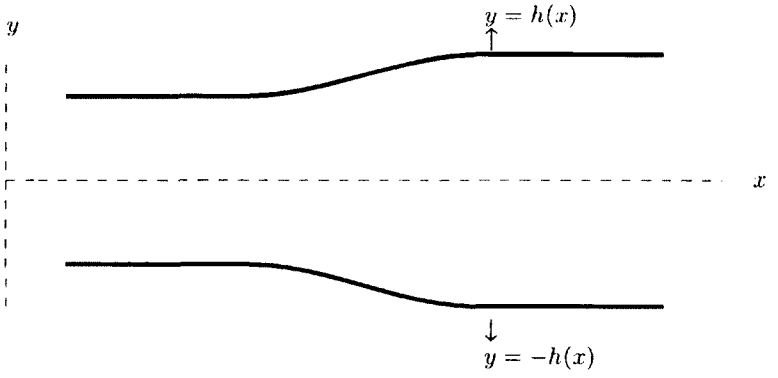

Fig. 32. Schematic diagram of a non-uniform duct.

The top and bottom sides of the duct are expressed by functions $y = h(x)$ and $y = -h(x)$, respectively. They represents heights from the x-axis to the top and the bottom of the duct. In Fig. 33, the physical domain and its mesh in terms of x and y are shown. The uniform computational domain in $\bar{x}$ and $\bar{y}$ and its mesh used in the simulations are shown in the bottom of the same figure.

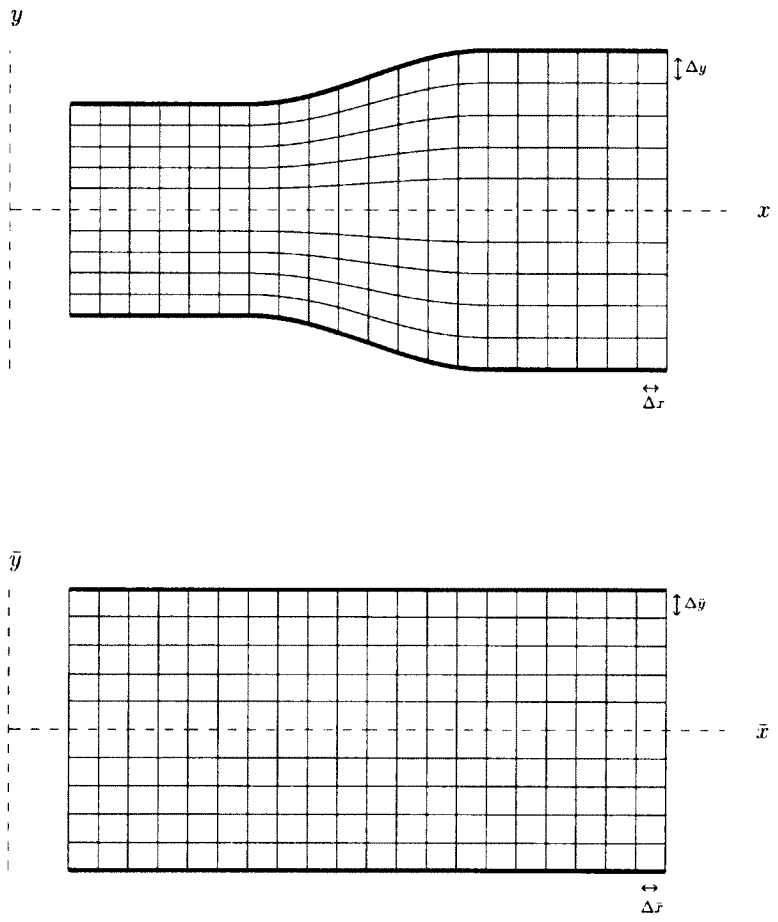

Fig. 33. Top: Physical domain of the non-uniform duct; Bottom: Uniform computational domain and mesh for time domain simulation and some of grid lines are shown.

Not all of the grid lines used in the computations are shown in Fig. 33. We can get the variables of the customized uniform computational domain by a suitable change of variables defined as

$$\bar{x}(x,y) = x,$$
$$\bar{y}(x,y) = \frac{h_0}{h(x)}y$$

where $h_0 = h(x_1)$ which is a value of the function h at the left-end of the duct. The point x_1 is the value on the x-axis where the duct inlet starts.
It is easy to find that

$$\frac{\partial \bar{x}}{\partial x} = 1; \quad \frac{\partial \bar{x}}{\partial y} = 0; \quad \frac{\partial \bar{y}}{\partial x} = -\frac{h_0 h'(x)}{h^2(x)}y; \quad \frac{\partial \bar{y}}{\partial y} = \frac{h_0}{h(x)}. \tag{65}$$

The first order spatial derivatives of the governing equations can be evaluated using the chain rule. By applying the chain rule to change of variables, we have

$$\frac{\partial}{\partial x} = \frac{\partial}{\partial \bar{x}}\frac{\partial \bar{x}}{\partial x} + \frac{\partial}{\partial \bar{y}}\frac{\partial \bar{y}}{\partial x}.$$
$$\frac{\partial}{\partial y} = \frac{\partial}{\partial \bar{x}}\frac{\partial \bar{x}}{\partial y} + \frac{\partial}{\partial \bar{y}}\frac{\partial \bar{y}}{\partial y}.$$

By (65), we can rewrite as

$$\frac{\partial}{\partial x} = \frac{\partial}{\partial \bar{x}} + \left(-\frac{h_0 h'(x)}{h^2(x)}y\right)\frac{\partial}{\partial \bar{y}},$$
$$\frac{\partial}{\partial y} = \left(\frac{h_0}{h(x)}\right)\frac{\partial}{\partial \bar{y}}.$$

After expressing all of what we need in terms of new variables for the governing partial differential equations, variation of the mean flow Mach number changes in the duct also needs to be calculated. We consider a non-uniform duct with an axial Mach number M at the left side of the duct. We express A_j for each cross-sectional area as shown in Fig. 34. For each j, A_j is the corresponding line segment for a 2-D non-uniform duct.
As a reference, a ghost area A^* at which $M^* = 1$ can be also assumed to make a connection between areas. By using (64) from the previous section, we can get relations for different cross-section areas as

$$\frac{A(x)}{A^*} = \frac{1}{M(x)}\left(\frac{1 + \frac{\gamma-1}{2}M^2(x)}{\frac{\gamma+1}{2}}\right)^{\frac{\gamma+1}{2(\gamma-1)}}$$

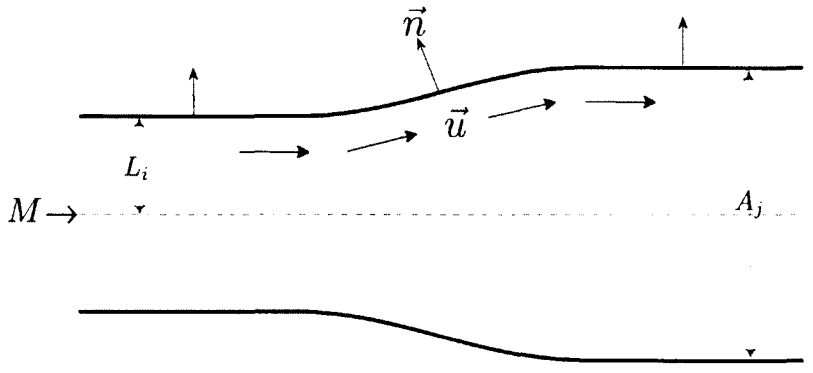

Fig. 34. Shematic sketch of the non-uniform duct with the velocity, normal vectors at the boundaries, lengths and cross-section areas.

where $\gamma = 1.4$ and $x = x_1, x_2, ..., x_N$.

For any two locations at x_i and x_j, we get

$$\frac{A(x_i)}{A^*} = \frac{1}{M(x_i)} \left(\frac{1 + 0.2 \cdot M^2(x_i)}{1.2} \right)^3$$

and

$$\frac{A(x_j)}{A^*} = \frac{1}{M(x_j)} \left(\frac{1 + 0.2 \cdot M^2(x_j)}{1.2} \right)^3 .$$

If we divide the top equation by the bottom equation, then we get

$$\frac{A(x_i)}{A(x_j)} = \frac{M(x_j)}{M(x_i)} \left(\frac{1 + 0.2 \cdot M^2(x_i)}{1 + 0.2 \cdot M^2(x_j)} \right)^3 .$$

Since the $M(x_1)$ and all $A(x)$ values are already known, we can express all $M(x_j)$ where $1 < j \leq N$.

The duct walls are assumed to solid and impermeable to the mean flow, so we have the mean flow boundary condition

$$\boldsymbol{u} \cdot \vec{n} = 0 \tag{66}$$

where $\boldsymbol{u} = (u, v)$ and $\vec{n}$ is the normal vector at solid walls. They are shown in Fig. 34.

The normal vector, $\vec{n}$, can be expressed as

$$\begin{aligned} \vec{n} &= \vec{\nabla} \cdot (y - h(x)) \\ &= (-h'(x), 1) \end{aligned} \tag{67}$$

Then, at boundaries of the solid wall duct by plugging (67) into (66), we get

$$(u, v) \cdot (-h'(x), 1) = 0$$

which is

$$v = h'(x)u. \tag{68}$$

For the uniform parts of the non-uniform duct shown in Fig. 34, $h'(x) = 0$, so we have $v = 0$. However, it is not zero at the boundaries of the slowly varying duct since $h'(x) \neq 0$. For simplicity, we assume that v varies with y linearly for this part of the duct. Let $v = v^b$ at the boundary. That variation can be formulated as

$$v_i(y) = v_i^b \frac{y}{L_i} \tag{69}$$

where L_i is a distance from the x-axis to boundaries for every x-value (see Fig. 34). A Mach number in the direction of y will be denoted as M_y. By (68) and (69), the M_y can be written as

$$M_y(x, y) = M(x)h'(x)\frac{y}{h(x)}.$$

5.3 NUMERICAL RESULTS FOR A 2-D NON-UNIFORM DUCT

We consider a 2-D non-uniform duct with a region of varying duct between $x = X_1$ and $x = X_2$ and uniform parts elsewhere. It is shown with location of a source function and PML absorbing boundary regions in Fig. 35. Assume that an incoming flow is present at the left side of duct for the Euler(forward) problem and at the right side of duct for Adjoint(backward) problem.

Due to the non-uniform duct body, the incident wave will be reflected as well as transmitted to the other side of the non-uniform region. The incoming mode will also be scattered into other modes. In this section, our goal is to examine duct modes which are incoming, reflected and transmitted duct modes at various x locations inside the duct. The forced mode $(0, 2)$ that is effective in forcing a wave packet is

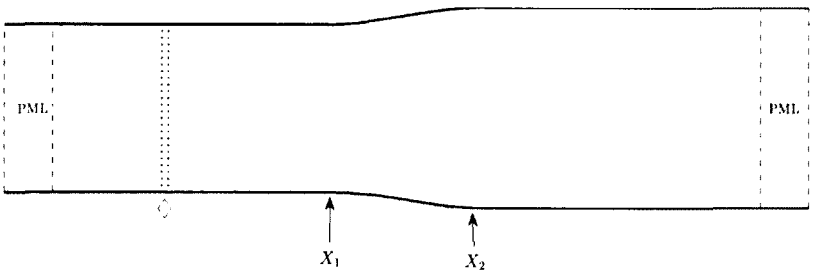

Fig. 35. A 2-D non-uniform duct showing a source function location (dotted-line) and PML regions (dashed-line).

used to simulate the forward and adjoint problems. We put sources at the uniform parts of the duct. They are located at $x_S = 0$ and $x_{\tilde{S}} = 300$ for forward and adjoint problems, respectively. The varying part of the duct is expressed with a cosine function. This part is from $X_1 = 100$ to $X_2 = 200$. The two uniform sections and the varying part for the top of the non-uniform duct can be expressed by $h(x)$ as

$$h(x) = \begin{cases} L & \text{if } x \le X_1 \\ \frac{L+H}{2} + \frac{H-L}{2}\cos\left(\frac{(x-X_1)\pi}{X_2-X_1} - \pi\right) & \text{if } X_1 < x < X_2 \\ H & \text{if } X_2 \le x \end{cases}$$

where $L = 25$ that is half of the height of the left uniform section and $H = 30$ that is half of the height of the right uniform section. The bottom part of the non-uniform duct can be expressed by $-h(x)$.

A TDWP simulation is carried out to get the time domain solution. Instantaneous pressure contours at $t = 20, 100, 300, 500$ and the pressure distribution at $\omega = 3\pi/50, 4\pi/50, 6\pi/50$ in the frequency domain are shown in Figs. 36 and 37 for the forward solution without a Mach number. The frequency domain solutions are obtained by an FFT of the time domain solutions. We should emphasize that solutions at other frequencies are also available in the same time domain solution.

At non-reflecting boundaries in Fig. 36, the right-going waves and left-going waves are absorbed by the PML at the right and left boundaries, respectively. We can find cut-on duct modes at any x location of the uniform parts of the non-uniform duct by the duct modal decomposition method given in section 3.5. For this process, the various x locations are chosen from the uniform parts of the duct. Two cases will

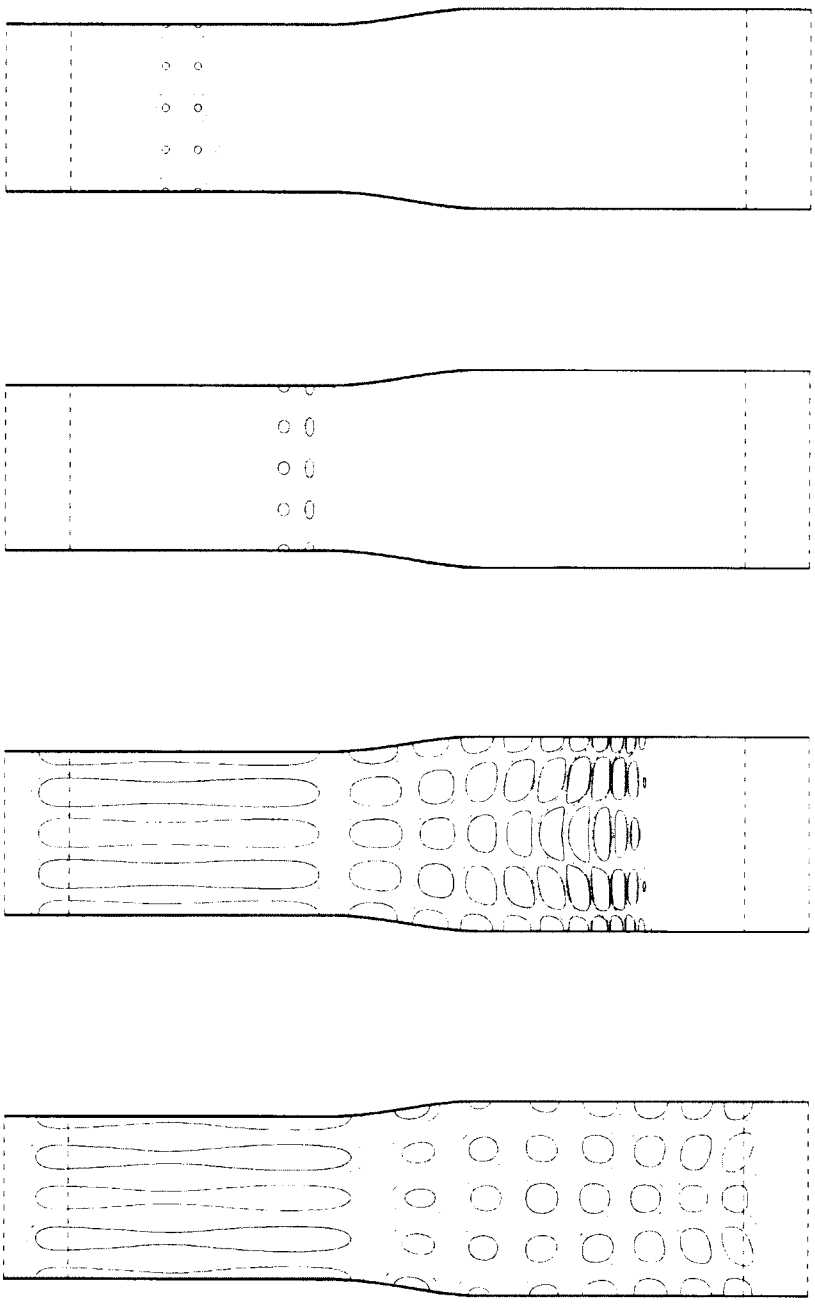

Fig. 36. Time domain pressure contours of the Euler solution at $t = 20, 100, 300, 500$.

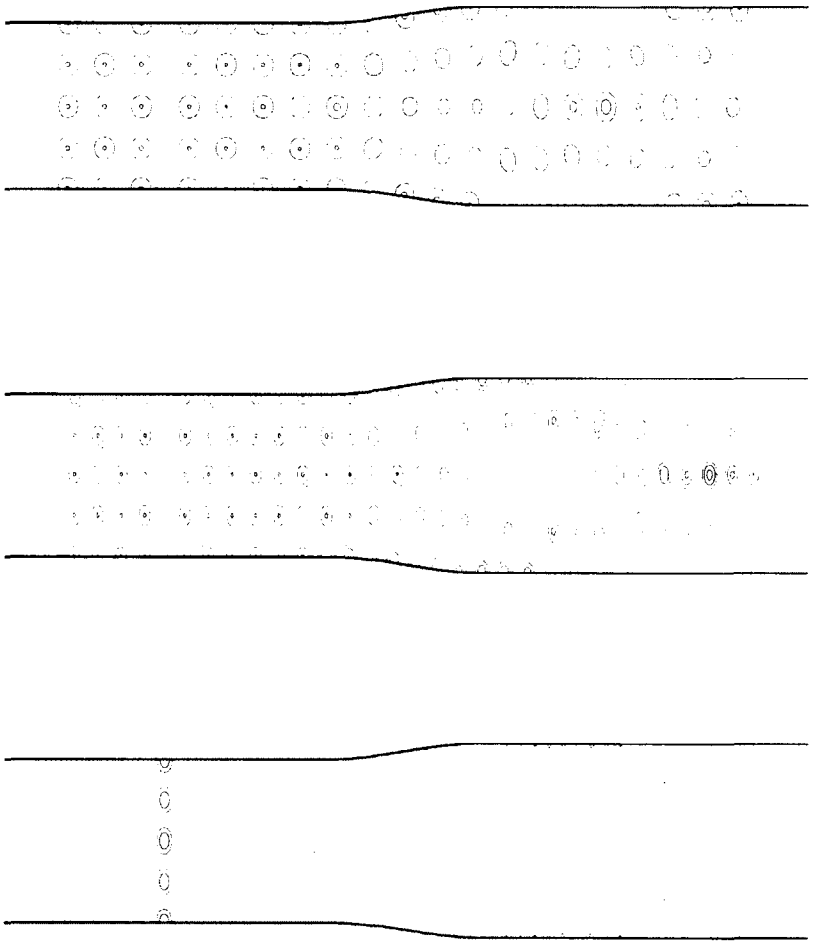

Fig. 37. Frequency domain pressure contours at $\omega = 3\pi/50, 4\pi/50. 6\pi/50$ by FFT of the time domain solution given in Fig. 36.

be shown with Mach number $M = 0$ and $M = 0.45$, respectively. We get the time domain solutions for the forward and adjoint problems by TDWP simulations in which the forced mode $(0, 2)$. Thereafter these solutions are converted to frequency domain solutions by FFT. The frequency domain solutions can be decomposed into cut-on duct modes at various x locations inside the duct at selected frequencies as described in section 3.5. After converting the time domain solutions of pressure and axial velocity to their frequency domain solutions by FFT, the modal decomposition method for 2-D case can be written as

$$A^+_{0n} e^{ik^+_{0n}x} + A^-_{0n} e^{ik^-_{0n}x} = \frac{\int_{-L_y}^{L_y} \hat{p}_0(x, y, \omega)\phi_{0n}(y)dy}{\int_{-L_y}^{L_y} \phi^2_{0n}(y)dy}. \tag{70}$$

$$A^+_{0n} \frac{k^+_{0n}}{w - Mk^+_{0n}} e^{ik^+_{0n}x} + A^-_{0n} \frac{k^-_{0n}}{w - Mk^-_{0n}} e^{ik^-_{0n}x} = \frac{\int_{-L_y}^{L_y} \hat{u}_0(x, y, \omega)\phi_{0n}(y)dy}{\int_{-L_y}^{L_y} \phi^2_{0n}(y)dy}. \tag{71}$$

The integrals in (70) and (71) are computed numerically. Finally, by solving (70) and (71), we find A^+_{0n} and A^-_{0n} which are the amplitude of the duct mode $(0, n)$ propagating to the right and left respectively.

We show results at different frequencies in Figs. 38-41 for forward and adjoint problems. S and $\tilde{S}$ indicate the source locations of the ducts in these figures. We can see that the incoming forced mode $(0, 2)$ is scattered into other cut-on modes. The cut-on modes number changes according to frequency that is used for FFT. For the forward problem solution shown in Fig. 39, cut-on modes are from $(0, 0)$ to $(0, 6)$ at $\omega = 30\pi/250$. In Fig. 41, cut-on modes are from $(0, 0)$ to $(0, 4)$ at $\omega = 20\pi/250$ for the adjoint problem solution.

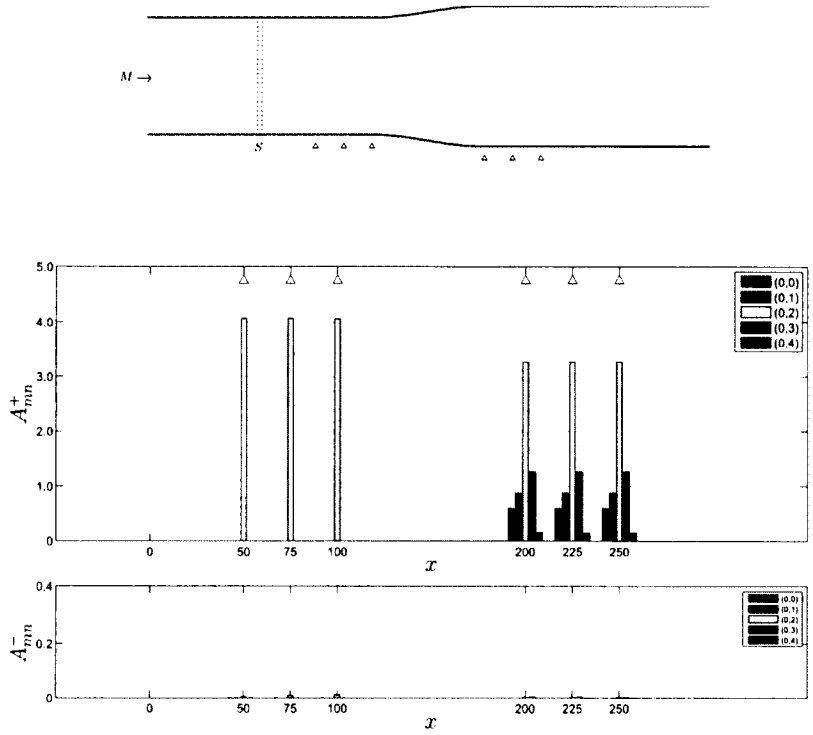

Fig. 38. Forward problem solution at $\omega = 20\pi/250$ for the forced mode $(0, 2)$ and $M = 0$.

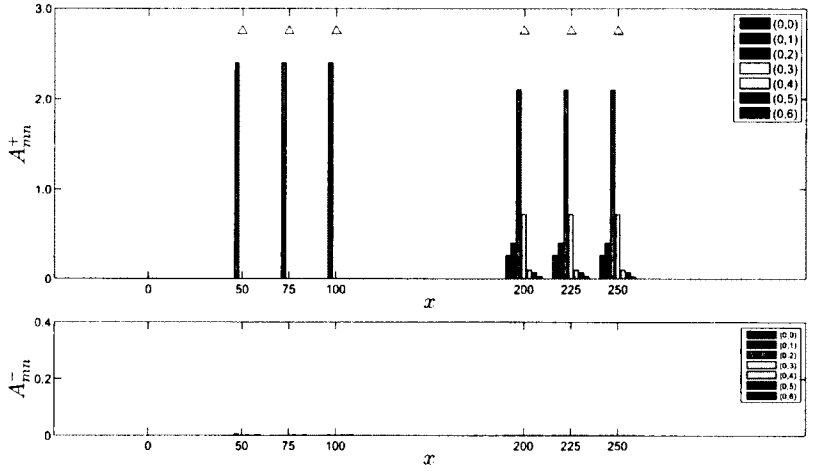

Fig. 39. Forward problem solution at $\omega = 30\pi/250$ for the forced mode $(0, 2)$ and $M = 0.45$.

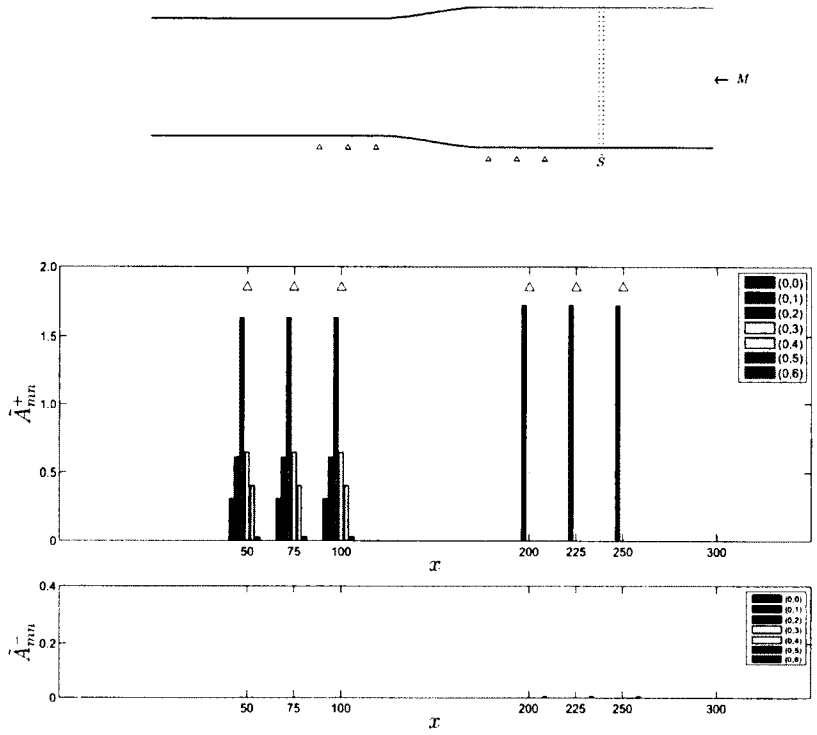

Fig. 40. Adjoint problem solution at $\omega = 30\pi/250$ for the forced mode $(0, 2)$ and $M = 0$.

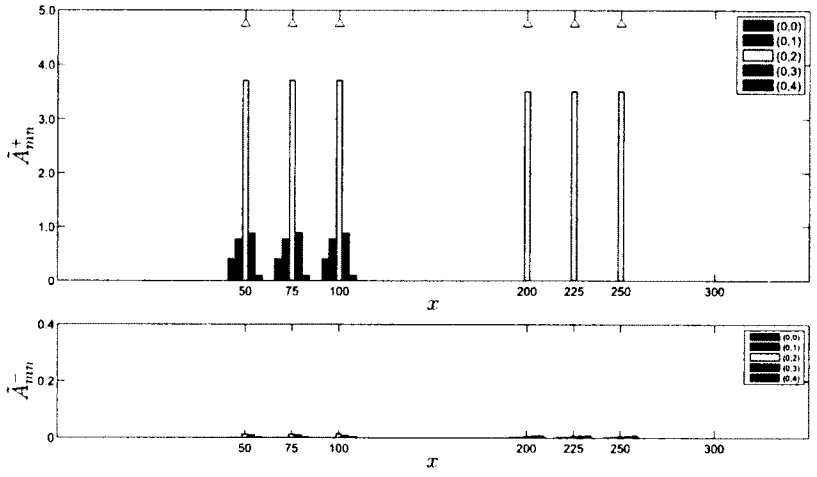

Fig. 41. Adjoint problem solution at $\omega = 20\pi/250$ for the forced mode $(0, 2)$ and $M = 0.45$.

5.4 NUMERICAL RESULTS FOR A 3-D NON-UNIFORM DUCT

An application to a 3-D duct is carried out in this section. Consider a 3-D non-uniform duct as shown in Fig. 42 with a region of varying duct area in the y-direction. The side of the duct in the z- direction is uniform.

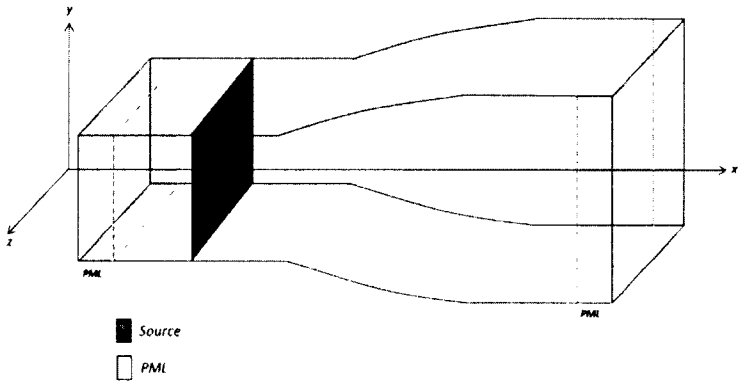

Fig. 42. A 3-D non-uniform duct and a plane source.

Firstly, a plane source will be used for computations and simulations for this case. It is shown in Fig. 42 as an example. Secondly, all calculations and relations in previous sections for mean flow are still valid for the 3-D non-uniform duct because the duct is assumed to uniform in z direction. In addition to this, all calculations and assumptions for M_y are also same. Because of the shape of the duct here, M_z, which is a Mach number of the mean flow in the direction of z is zero all over the duct.

A time sequence of sample instantaneous pressure contours of a simulation with the forced mode $(3, 2)$ and $M = 0.3$ for the forward problem on 2-D slices in 3-D non-uniform duct are shown in Figs. 43-45.

In order to apply the duct modal decomposition method properly, the time domain solution inside the 3-D nonuniform duct is converted to the frequency domain solution by FFT. These forward problem frequency domain solutions at $\omega = \pi/5$ are decomposed into cut-on duct modes at different x locations by using (38) and (39). They are shown in Fig. 46. In Fig. 47, cut-on modes at $\omega = \pi/5$ are shown for the adjoint problem simulation with the forced mode $(3, 2)$ and $M = 0.3$.

In this chapter, we have focused on the non-uniform ducts with non-uniform mean flows. One dimensional compressible flow is assumed for the mean flow inside the duct. The area-Mach number relation was derived to compute the mean flows inside the duct. The TDWP method was carried out for simulations of the forward problem and the adjoint system inside the 2-D and 3-D non-uniform ducts. The pressure contours of the forward problem were plotted to confirm that the TDWP method is implemented correctly to non-uniform ducts with the forced modes. At various x locations which are chosen from the uniform sections of the duct, amplitudes of the propagating duct modes were examined for both system. We observe that amplitudes of the forced modes are constant for each uniform sections. The results also showed that the incoming mode would be scattered into other modes due to non-uniform duct body. The incident waves would be reflected as well as transmitted to another uniform section.

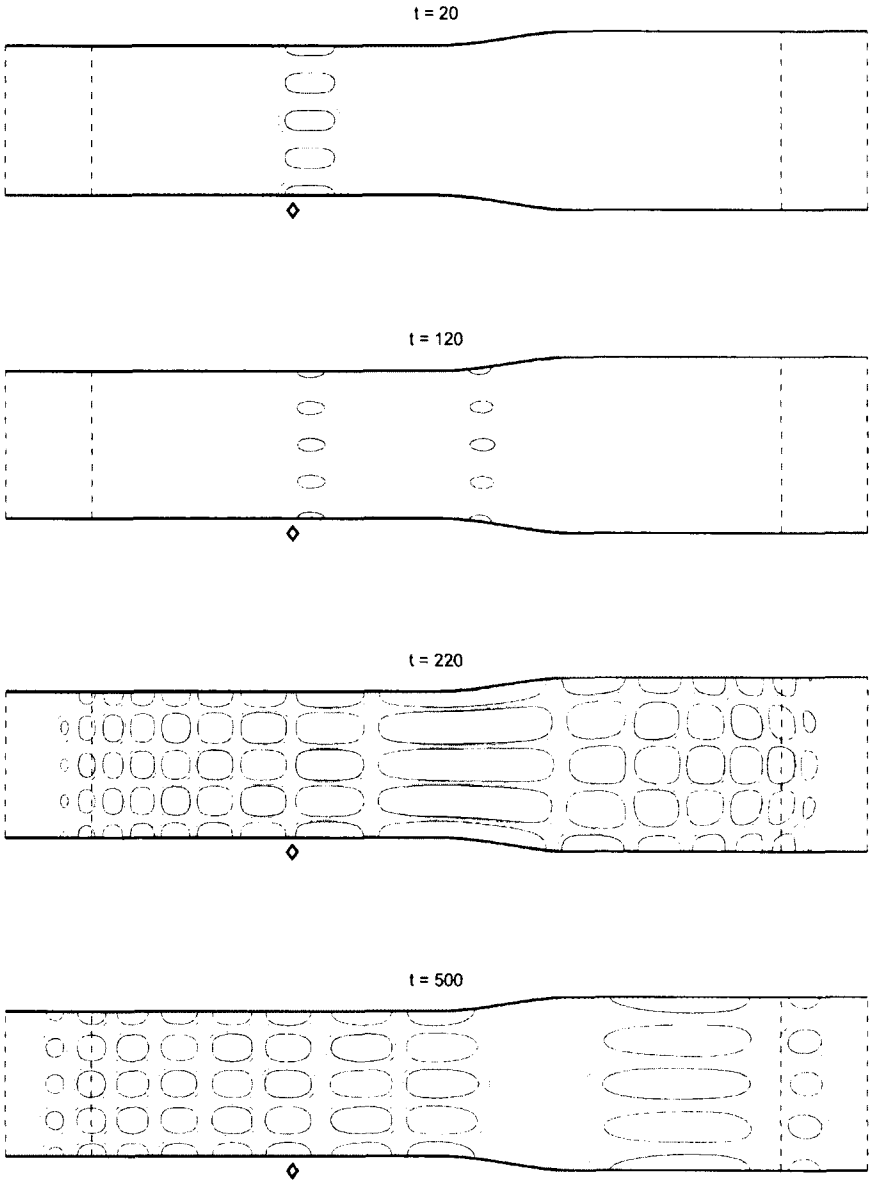

Fig. 43. A time sequence of instantaneous pressure contours of an acoustic wave packet on the xy slice at $z = 0$.

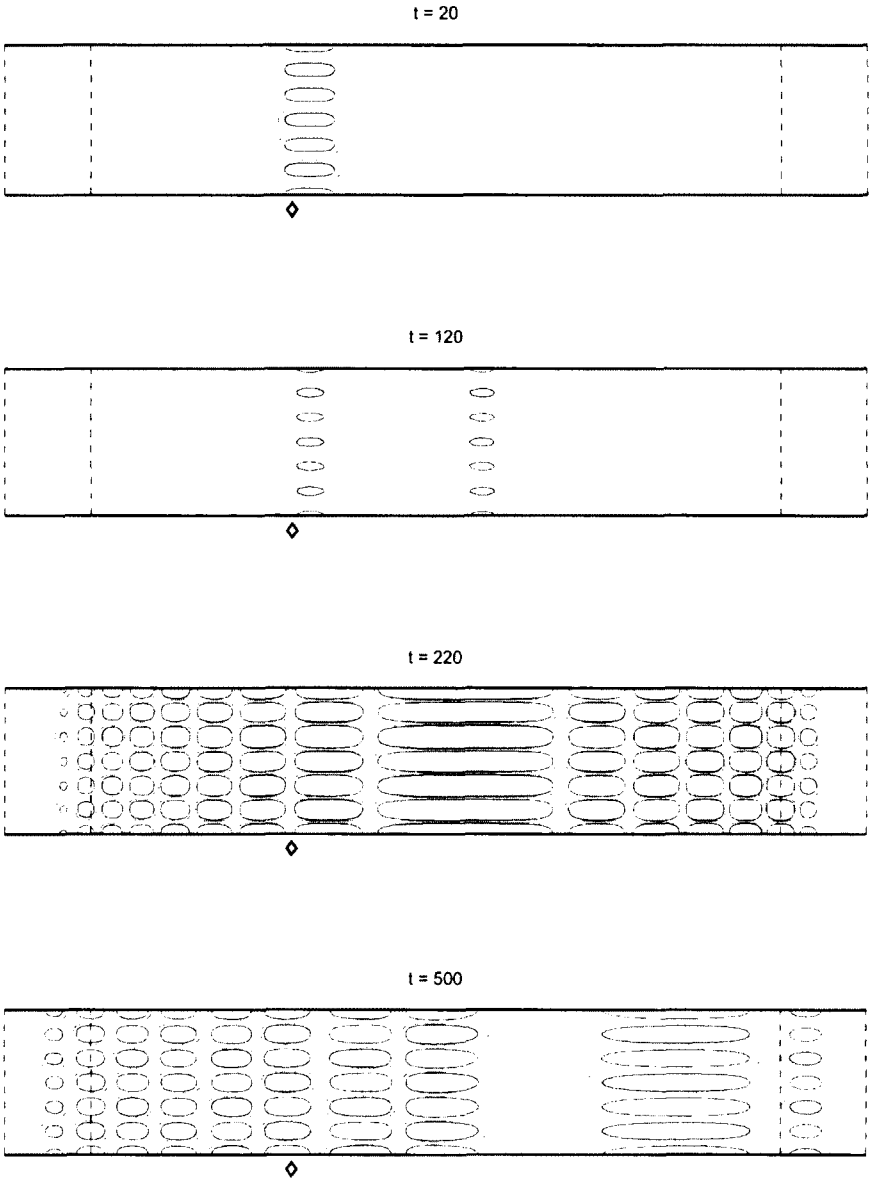

Fig. 44. A time sequence of instantaneous pressure contours of an acoustic wave packet on the xz slice at $y = 0$.

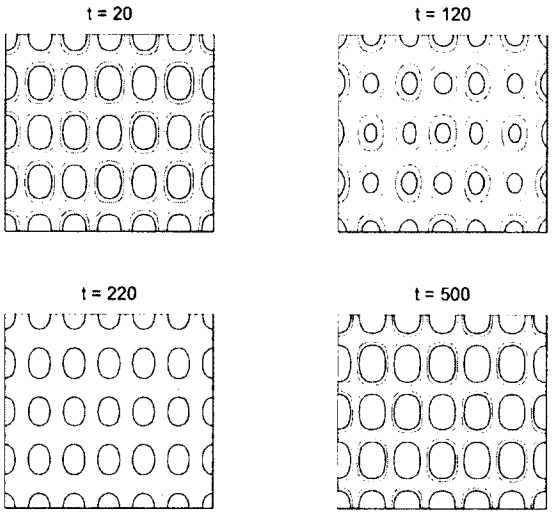

Fig. 45. A time sequence of instantaneous pressure contours of an acoustic wave packet on the yz slice at $x = 25$.

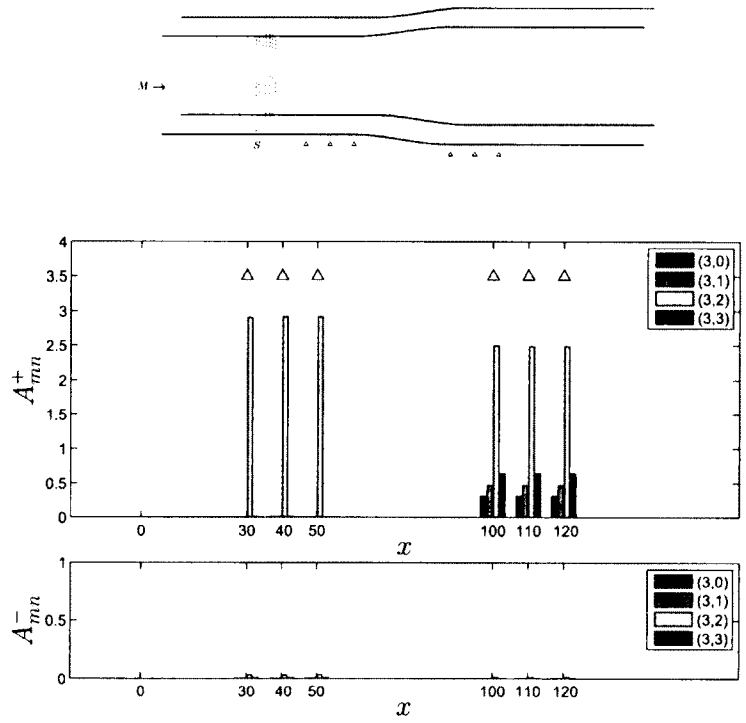

Fig. 46. Forward problem solution at $\omega = \pi/5$ for the forced mode $(3, 2)$ and $M = 0.3$.

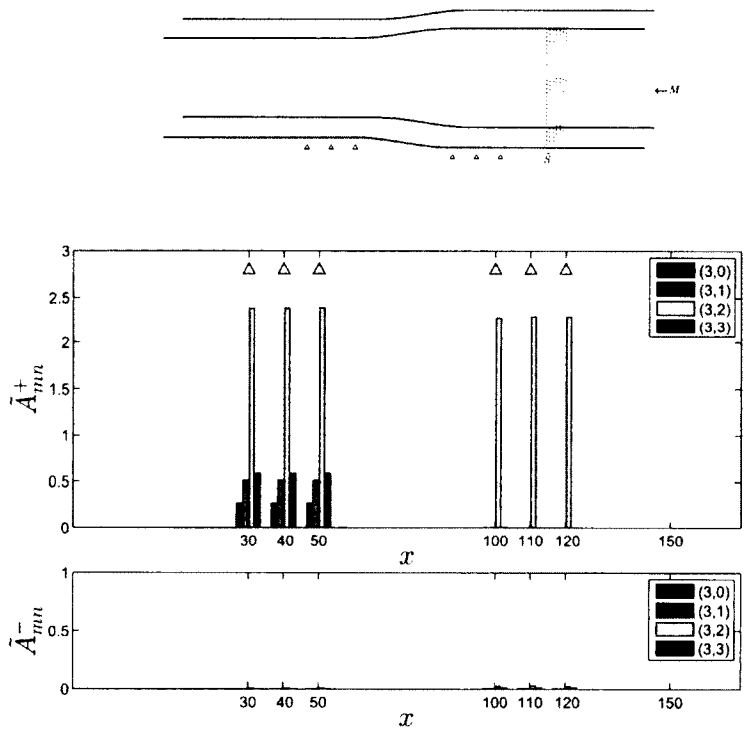

Fig. 47. Adjoint problem solution at $\omega = \pi/5$ for the forced mode $(3, 2)$ and $M = 0.3$.

CHAPTER 6

A DISCUSSION ON THE ACOUSTIC ENERGY AND ADJOINT SOLUTIONS

The sound propagation equations in flows are so complicated that analytic solutions exist only for the simplest examples. Global properties of the sound waves can help for comprehension of the solutions and offer a valuable check and an assessment of numerical solutions. One of these properties is the energy conservation. In [33, 36, 37, 5], there are works about energy and energy conservation for variety of ducts and flows. In this chapter, we will show relations between energy conservation and Euler-adjoint conservation for a uniform duct. Also, for any uniform and non-uniform duct with flow, it is possible to show the Euler-adjoint conservation is valid. In [36], the acoustic energy equation is given as

$$\frac{\partial E}{\partial t} + \nabla \cdot N = P$$

where E represents a generalized acoustic energy density, N is the generalized acoustic energy flux, and P is a production term which is zero in an irrotational uniform-entropy flow.

For the linearized Euler equations, the acoustic energy equation can be obtained as follow. For the uniform axial mean flow $(M_x, 0, 0)$, we write the linearized Euler equations as

$$\frac{\partial u}{\partial t} + M_x \frac{\partial u}{\partial x} + \frac{\partial p}{\partial x} = 0, \tag{72}$$

$$\frac{\partial v}{\partial t} + M_x \frac{\partial v}{\partial x} + \frac{\partial p}{\partial y} = 0, \tag{73}$$

$$\frac{\partial w}{\partial t} + M_x \frac{\partial w}{\partial x} + \frac{\partial p}{\partial z} = 0, \tag{74}$$

$$\frac{\partial p}{\partial t} + M_x \frac{\partial p}{\partial x} + \frac{\partial u}{\partial x} + \frac{\partial v}{\partial y} + \frac{\partial w}{\partial z} = 0. \tag{75}$$

By multiplication of $u*(72)+v*(73)+w*(74)+p*(75)$, we get

$$\frac{\partial E_e}{\partial t}+\nabla\cdot\boldsymbol{N}_e=0$$

where $E_e=u^2+v^2+w^2+p^2$ and $\boldsymbol{N}_e=(M_x(u^2+v^2+w^2+p^2)+2up,2vp,2wp)$. Unfortunately, this energy equation is valid only for acoustic waves in a uniform mean flow. Acoustic energy equation for non-uniform mean flow is still an open question in aeroacoustics.

For adjoint system, on the other hand by substituting (53) into (43), we can have

$$\frac{\partial E}{\partial t}+\nabla\cdot\boldsymbol{J}=0$$

where

$$E(\boldsymbol{w},\tilde{\boldsymbol{w}})=\tilde{\boldsymbol{w}}^T\boldsymbol{w}=\tilde{u}u+\tilde{v}v+\tilde{w}w+\tilde{p}p=u^2+v^2+w^2+p^2$$

and

$$\begin{aligned}\boldsymbol{J}(\boldsymbol{w},\tilde{\boldsymbol{w}})&=(M_x(\tilde{u}u+\tilde{v}v+\tilde{w}w+\tilde{p}p)+p\tilde{u}+u\tilde{p},p\tilde{v}+v\tilde{p},p\tilde{w}+w\tilde{p})\\&=\left(M_x(u^2+v^2+w^2+p^2)+2up,2vp,2wp\right).\end{aligned}$$

By $E_e=E$ and $\boldsymbol{N}_e=\boldsymbol{J}$, we show that the substitution of (53) into (43) recovers the acoustic energy equation in a uniform mean flow.

More importantly, the Euler-adjoint relation is valid for non-uniform flow as well. To show the Euler-adjoint conservation inside a duct (in 2-D), let the solutions inside the duct be written in the frequency domain as

$$\boldsymbol{w}(\boldsymbol{r},t)=\boldsymbol{f}(\boldsymbol{r},\omega)e^{-i\omega t}$$

and

$$\tilde{\boldsymbol{w}}(\boldsymbol{r},t)=\tilde{\boldsymbol{f}}(\boldsymbol{r},\omega)e^{-i\omega t}$$

where $\boldsymbol{r}=(x,y)$.

In the frequency domain, we have

$$(-i\omega)f+\boldsymbol{A}\frac{\partial f}{\partial x}+\boldsymbol{B}\frac{\partial f}{\partial y}+\boldsymbol{D}f=0 \tag{76}$$

and

$$(-i\omega)\tilde{f}+\tilde{\boldsymbol{A}}\frac{\partial\tilde{f}}{\partial x}+\tilde{\boldsymbol{B}}\frac{\partial\tilde{f}}{\partial y}+\tilde{\boldsymbol{D}}\tilde{f}=0. \tag{77}$$

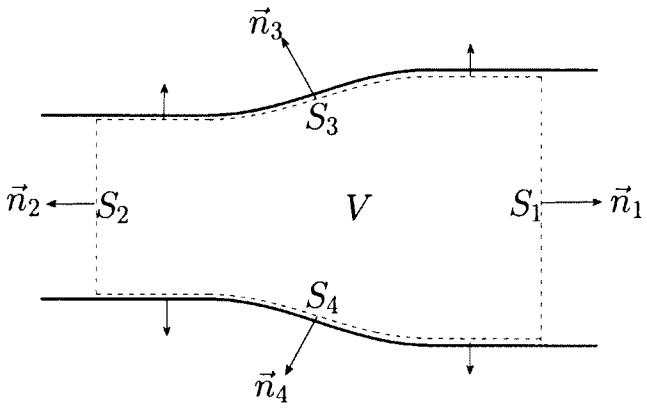

Fig. 48. An outlined volume of a non-uniform duct.

By an operation $\tilde{f}^{*T}(76) + f^T(77)^*$, we get

$$\tilde{f}^{*T}\boldsymbol{A}\frac{\partial f}{\partial x} + f^T\tilde{\boldsymbol{A}}\frac{\partial \tilde{f}^*}{\partial x} + \tilde{f}^{*T}\boldsymbol{B}\frac{\partial f}{\partial y} + f^T\tilde{\boldsymbol{B}}\frac{\partial \tilde{f}^*}{\partial y} + \tilde{f}^{*T}\boldsymbol{D}f + f^T\tilde{\boldsymbol{D}}\tilde{f}^* = 0.$$

It can be reorganized using the definition of the adjoint system as

$$\frac{\partial}{\partial x}\left(\tilde{f}^{*T}\boldsymbol{A}f\right) + \frac{\partial}{\partial y}\left(\tilde{f}^{*T}\boldsymbol{B}f\right) = 0$$

or, equivalently,

$$\nabla \cdot \boldsymbol{J}(f, \tilde{f}^*) = \nabla \cdot \left(\tilde{f}^{*T}\boldsymbol{A}f, \tilde{f}^{*T}\boldsymbol{B}f\right) = 0. \tag{78}$$

Integrate (78) over the volume shown in Fig. 48,

$$\int_V \nabla \cdot \left(\tilde{f}^{*T}\boldsymbol{A}f, \tilde{f}^{*T}\boldsymbol{B}f\right) dV = 0.$$

By divergence theorem, the above becomes

$$\int_{S_1} \left(\tilde{f}^{*T}\boldsymbol{A}f, \tilde{f}^{*T}\boldsymbol{B}f\right) \cdot \vec{n_1}\, dS + \int_{S_2} \left(\tilde{f}^{*T}\boldsymbol{A}f, \tilde{f}^{*T}\boldsymbol{B}f\right) \cdot \vec{n_2}\, dS$$
$$+ \int_{S_3} \left(\tilde{f}^{*T}\boldsymbol{A}f, \tilde{f}^{*T}\boldsymbol{B}f\right) \cdot \vec{n_3}\, dS + \int_{S_4} \left(\tilde{f}^{*T}\boldsymbol{A}f, \tilde{f}^{*T}\boldsymbol{B}f\right) \cdot \vec{n_4}\, dS = 0. \tag{79}$$

We, here, examine (79) for two duct options. The first one is the uniform duct with mean flow $(M_x, 0)$. On S_3,

$$\int_{S_3} \left(\tilde{f}^{*T}\boldsymbol{A}f, \tilde{f}^{*T}\boldsymbol{B}f\right) \cdot (0, 1)\, dS = \int_{S_3} (\tilde{p}^*\hat{v} + \hat{p}\tilde{v}^*)\, dS = 0$$

since $\tilde{v}^* = \hat{v} = 0$ on the solid walls.

Another one is non-uniform duct with $(M_x(x,y), M_y(x,y))$. By (67) and (68) in section 5.2, the following relations are given $\vec{n} = (-h'(x), 1)$ and $M_y(x,y) = h'(x)M_x(x)$ at solid walls. On S_3,

$$\int_{S_3} \left(\tilde{f}^{*T}\boldsymbol{A}f, \tilde{f}^{*T}\boldsymbol{B}f\right) \cdot \vec{n_3}\, dS =$$

$$= \int_{S_3} \left[(\tilde{u}^*\hat{u} + \tilde{v}^*\hat{v} + \tilde{p}^*\hat{p})\,(M_x, M_y) + \hat{p}(\tilde{u}^*, \tilde{v}^*) + \tilde{p}^*(\hat{u}, \hat{v})\right] \cdot \vec{n_3}\, dS = 0$$

since $(M_x, M_y) \cdot \vec{n_3} = 0$, $(\hat{u}, \hat{v}) \cdot \vec{n_3} = 0$ and $(\tilde{u}^*, \tilde{v}^*) \cdot \vec{n_3} = 0$. (see section 5.2 for more information).

On S_4 for both ducts, we can follow the same procedures and easily show

$$\int_{S_4} \left(\tilde{f}^{*T}\boldsymbol{A}f, \tilde{f}^{*T}\boldsymbol{B}f\right) \cdot \vec{n_4}\, dS = 0.$$

For both ducts, the equation (79) becomes

$$\int_{S_1} \left(\tilde{f}^{*T}\boldsymbol{A}f, \tilde{f}^{*T}\boldsymbol{B}f\right) \cdot \vec{n_1}\, dS + \int_{S_2} \left(\tilde{f}^{*T}\boldsymbol{A}f, \tilde{f}^{*T}\boldsymbol{B}f\right) \cdot \vec{n_2}\, dS = 0.$$

By plugging $\vec{n_1}$ and $\vec{n_2}$ into the above equation, we have

$$\int_{S_1} \left(\tilde{f}^{*T}\boldsymbol{A}f, \tilde{f}^{*T}\boldsymbol{B}f\right) \cdot (1,0)\, dS + \int_{S_2} \left(\tilde{f}^{*T}\boldsymbol{A}f, \tilde{f}^{*T}\boldsymbol{B}f\right) \cdot (-1,0)\, dS = 0.$$

Finally, we can get the following equality for the Euler-adjoint conservation,

$$\int_{S_1} \tilde{f}^{*T}\boldsymbol{A}f\, dS = \int_{S_2} \tilde{f}^{*T}\boldsymbol{A}f\, dS, \tag{80}$$

or, equivalently,

$$\int_{S_1} \boldsymbol{J}_x(f, \tilde{f}^*)\, dS = \int_{S_2} \boldsymbol{J}_x(f, \tilde{f}^*)\, dS. \tag{81}$$

This implies that the Euler-adjoint conservation is valid for uniform and non-uniform duct.

From (80), we can write for uniform mean flow

$$\tilde{f}^{*T}\boldsymbol{A}f = (\tilde{\rho}^*, \tilde{u}^*, \tilde{v}^*, \tilde{p}^*) \begin{pmatrix} M_x & 1 & 0 & 0 \\ 0 & M_x & 0 & 1 \\ 0 & 0 & M_x & 0 \\ 0 & 1 & 0 & M_x \end{pmatrix} \begin{pmatrix} \hat{\rho} \\ \hat{u} \\ \hat{v} \\ \hat{p} \end{pmatrix}$$

$$= (0, M_x\tilde{u}^* + \tilde{p}^*, M_x\tilde{v}^*, \tilde{u}^* + M_x\tilde{p}^*) \begin{pmatrix} \hat{\rho} \\ \hat{u} \\ \hat{v} \\ \hat{p} \end{pmatrix}$$

$$= M_x\left(\tilde{u}^*\hat{u} + \tilde{v}^*\hat{v} + \tilde{p}^*\hat{p}\right) + \tilde{p}^*\hat{u} + \tilde{u}^*\hat{p}.$$

By using the relation (53)

$$\tilde{f}^{*T}\boldsymbol{A}f = M_x\left(u\hat{u}^* + v\hat{v}^* + p\hat{p}\right) + p\hat{u}^* + u\hat{p}^*. \tag{82}$$

This shows again that the Euler-adjoint conservation is equivalent to energy conservation in the case of uniform mean flow inside the uniform duct.

CHAPTER 7

RECIPROCITY

In this chapter, we derive two reciprocal relations between the solutions of the Euler and adjoint systems. First, we will build a reciprocal relation between duct modes in a closed non-uniform duct. Second, a reciprocal relation will be developed between a point source at the far-field and duct modes inside the duct. In other words, a reciprocity between the duct propagating mode and far-field sound will be derived.

7.1 RECIPROCITY BETWEEN DUCT MODES

We consider a non-uniform duct that consists of two uniform sections which are connected by a smoothly varying transition region called a non-uniform region. In Fig. 49, it is shown with incident, reflected and transmitted waves for forward and adjoint problem separately. We assume that an incoming duct mode is present at the left side of the non-uniform duct for the forward problem and at the right side of the non-uniform duct for the adjoint problem. These incident waves will be reflected as well as transmitted to the other side of the non-uniform region on account of the non-uniform duct body. The incoming mode will also be scattered into other modes. We assume that a region of varying duct area is between $x = X_1$ and $x = X_2$. In constructing reciprocal relations, we only focus on duct modes at the uniform sections and not the modes at the non-uniform duct region.

Let the solutions inside the duct be written in the frequency domain as

$$\boldsymbol{w}(\boldsymbol{r}, t) = \boldsymbol{f}(\boldsymbol{r}, \omega)e^{-i\omega t} \tag{83}$$

and

$$\tilde{\boldsymbol{w}}(\boldsymbol{r}, t) = \tilde{\boldsymbol{f}}(\boldsymbol{r}, \omega)e^{-i\omega t} \tag{84}$$

where $\boldsymbol{r} = (x, y, z)$, for the forward and adjoint problems respectively.
Let's also assume the solution in frequency domain inside the two uniform sections for the forward problem as

for $x < X_1$ (incoming and reflected waves):

$$\boldsymbol{f}(x, y, z, \omega) = A_{m_0 n_0} \phi_{m_0 n_0}(y, z) e^{ik^+_{m_0 n_0}(\omega)x} + \sum_{m', n'} R_{m'n'} \phi_{m'n'}(y, z) e^{ik^-_{m'n'}(\omega)x} \tag{85}$$

for $x > X_2$ (transmitted waves):

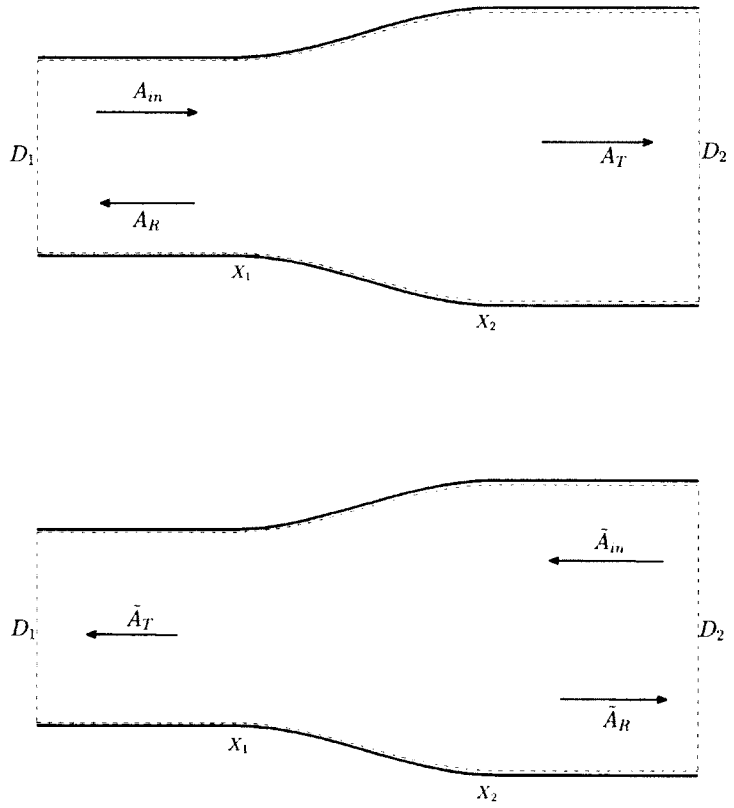

Fig. 49. Schematic diagram showing a non-uniform duct and incident, reflected and transmitted waves for forward and adjoint problems.

$$\boldsymbol{f}(x, y, z, \omega) = \sum_{m', n'} T_{m'n'} \phi_{m'n'}(y, z) e^{ik^+_{m'n'}(\omega)x} \tag{86}$$

where $A_{m_0 n_0}$ is the amplitude of the incoming mode, and $R_{m'n'}$ and $T_{m'n'}$ are the amplitudes of the reflected and transmitted wave modes respectively.

For the adjoint problem, we consider an incoming wave mode at the right side and

express the solution as

for $x < X_1$ (transmitted waves):

$$\tilde{\boldsymbol{f}}(x,y,z,\omega) = \sum_{\tilde{m}',\tilde{n}'} \tilde{T}_{\tilde{m}'\tilde{n}'} \phi_{\tilde{m}'\tilde{n}'}(y,z) e^{ik^+_{\tilde{m}'\tilde{n}'}(\omega)x} \tag{87}$$

for $x > X_2$ (incoming and reflected waves):

$$\tilde{\boldsymbol{f}}(x,y,z,\omega) = \tilde{A}_{\tilde{m}_0\tilde{n}_0} \phi_{\tilde{m}_0\tilde{n}_0}(y,z) e^{ik^+_{\tilde{m}_0\tilde{n}_0}(\omega)x} + \sum_{\tilde{m}',\tilde{n}'} \tilde{R}_{\tilde{m}'\tilde{n}'} \phi_{\tilde{m}'\tilde{n}'}(y,z) e^{ik^-_{\tilde{m}'\tilde{n}'}(\omega)x}. \tag{88}$$

In the frequency domain, we have the Euler equations and the adjoint system as follows,

$$-i\omega \boldsymbol{f} + \boldsymbol{L}(\boldsymbol{f}) = 0, \tag{89}$$

$$-i\omega \tilde{\boldsymbol{f}} + \tilde{\boldsymbol{L}}(\tilde{\boldsymbol{f}}) = 0. \tag{90}$$

As in Chapter 6, by an operation $\tilde{\boldsymbol{f}}^{*T}(89) + \boldsymbol{f}^T(90)^*$, we get

$$\nabla \cdot \boldsymbol{J}(\boldsymbol{f}, \tilde{\boldsymbol{f}}^*) = 0.$$

Integrating the above over a volume outlined in Fig. 49, it is shown in Chapter 6

$$\int_{D_1} J_x(\boldsymbol{f}, \tilde{\boldsymbol{f}}^*) dS - \int_{D_2} J_x(\boldsymbol{f}, \tilde{\boldsymbol{f}}^*) dS = 0. \tag{91}$$

Then, by substituting (85)-(88) into the above, due to orthogonality of the eigenfunctions, we get

$$A_{m_0n_0} \tilde{T}_{m_0n_0} \int_{D_1} \tilde{\phi}^{*T}_{m_0n_0} \boldsymbol{A} \phi_{m_0n_0}\, dS = T_{\tilde{m}_0\tilde{n}_0} \tilde{A}_{\tilde{m}_0\tilde{n}_0} \int_{D_2} \tilde{\phi}^{*T}_{\tilde{m}_0\tilde{n}_0} \boldsymbol{A} \phi_{\tilde{m}_0\tilde{n}_0}\, dS. \tag{92}$$

This equation is the reciprocal relation between duct modes of the forward and adjoint problems. It is a relation between incoming and transmitted modes of the forward and adjoint problems.

Equation (92) can also be written as

$$\alpha_{m_0n_0} \frac{\tilde{T}_{m_0n_0}}{\tilde{A}_{\tilde{m}_0\tilde{n}_0}} = \alpha_{\tilde{m}_0\tilde{n}_0} \frac{T_{\tilde{m}_0\tilde{n}_0}}{A_{m_0n_0}} \tag{93}$$

where the proportional constant

$$\alpha_{mn} = \int_D \tilde{\phi}^{*T}_{mn} \boldsymbol{A} \phi_{mn}\, dS.$$

The equation (93) establishes the direct relationship between any transmitted mode $(\tilde{m}_0, \tilde{n}_0)$ due to the incident mode (m_0, n_0) of the Euler equations and those of the adjoint system due to an incident $(\tilde{m}_0, \tilde{n}_0)$ mode.

Furthermore, let the eigenfunctions of the duct modes be expressed as

$$\phi_{mn}(y,z) = \begin{pmatrix} \phi_\rho \\ \phi_u \\ \phi_v \\ \phi_w \\ \phi_p \end{pmatrix} = \begin{pmatrix} \psi_{mn}(y,z) \\ \frac{k_{mn}}{\omega - \bar{u}_x k_{mn}} \psi_{mn}(y,z) \\ -\frac{i}{\omega - \bar{u}_x k_{mn}} \frac{\partial \psi_{mn}(y,z)}{\partial y} \\ -\frac{i}{\omega - \bar{u}_x k_{mn}} \frac{\partial \psi_{mn}(y,z)}{\partial z} \\ \psi_{mn}(y,z) \end{pmatrix}$$

and

$$\tilde{\phi}_{mn}(y,z) = \begin{pmatrix} \tilde{\phi}_\rho \\ \tilde{\phi}_u \\ \tilde{\phi}_v \\ \tilde{\phi}_w \\ \tilde{\phi}_p \end{pmatrix} = \begin{pmatrix} 0 \\ \bar{\rho} \frac{k_{mn}}{\omega - \bar{u}_x k_{mn}} \psi_{mn}(y,z) \\ -\bar{\rho} \frac{i}{\omega - \bar{u}_x k_{mn}} \frac{\partial \psi_{mn}(y,z)}{\partial y} \\ -\bar{\rho} \frac{i}{\omega - \bar{u}_x k_{mn}} \frac{\partial \psi_{mn}(y,z)}{\partial z} \\ \frac{1}{\gamma \bar{p}} \psi_{mn}(y,z) \end{pmatrix}$$

where $\psi_{mn}(y,z)$ is the pressure eigenfunction of mode (m,n). It is straightforward to verify, by using the expression in (62), that we have the proportional constant α_{mn} in (93) as

$$\begin{aligned} \alpha_{mn} = \int_D \tilde{\phi}_{mn}^{*T} \boldsymbol{A} \phi_{mn} \, dS &= 2 \left(\bar{u}_x + \frac{\gamma \bar{p}}{\bar{\rho}} \frac{k_{mn}}{\omega - \bar{u}_x k_{mn}} \right) \int_D \psi_{mn}^2 \, dS \\ &= 2 \left(\frac{d\omega}{dk} \right)_{mn} \int_D \psi_{mn}^2 \, dS \end{aligned} \tag{94}$$

where $D = [L_{y_1}, L_{y_2}] \times [L_{z_1}, L_{z_2}]$ and $\left(\frac{d\omega}{dk}\right)_{mn}$ is the group velocity of mode (m,n).

7.2 NUMERICAL VALIDATION OF RECIPROCITY BETWEEN DUCT MODES

In order to demonstrate and validate the reciprocal relations between the Euler and adjoint solutions, TDWP method simulations are carried out. We use mode $(2,3)$ as a forced mode for the forward problem. For the adjoint problem, five different forced modes $(2,0), (2,1), (2,2), (2,3)$ and $(2,4)$ are used to run the simulations in order to examine the reciprocal relations between the solutions of the forward and the adjoint problems. The Mach number is $M = 0.3$ for both problems. After converting the time domain solutions to frequency domain solutions by FFT and making proper

modal decompositions, we get cut-on duct modes at various x stations. They are re-scaled by amplitude of the incident mode that is at the closest station to source planes. In all the figures, the superscript notation "0" refers to this closest station and the other superscript "i" indicates the various x stations. In Figs. 50 and 51, the re-scaled amplitudes of the cut-on modes are shown for the forward and the adjoint solutions respectively. It is also shown that in the same figures, the re-scaled amplitude of the mode for the closest station is one.

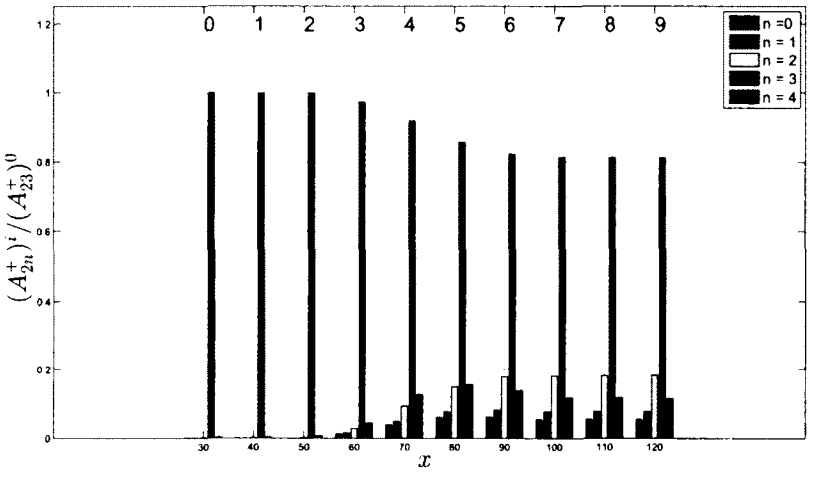

Fig. 50. The normalized amplitudes of right-going modes along the duct for the forced mode $(2,3)$ in the forward problem and "i" is the station number from 0 to 9.

To demonstrate reciprocal relations, we choose two stations from inside the duct, one from left uniform section and another one from right uniform section of the duct. To validate the reciprocal relation (93) between the duct modes, we can choose the left side at $x = 30$ and the right side at $x = 120$. The relation (93) can also be re-expressed as

$$\frac{\alpha_{mn}}{\alpha_{\tilde{m}\tilde{n}}}\frac{\tilde{T}_{mn}}{\tilde{A}_{\tilde{m}\tilde{n}}} = \frac{T_{\tilde{m}\tilde{n}}}{A_{mn}}. \tag{95}$$

In Fig. 52 (top), the amplitudes of the transmitted duct modes normalized by the mode incoming amplitude, $T_{\tilde{m}\tilde{n}}/A_{mn}$, in the forward problem is shown. They are the same as those in Fig. 50 at the stations $x = 100, 110, 120$. The expression formed by α_{mn} and $\alpha_{\tilde{m}\tilde{n}}$, and modal amplitudes, $\tilde{T}_{mn}$ and $\tilde{A}_{\tilde{m}\tilde{n}}$, of the adjoint problem is shown in Fig. 52 (bottom). Clearly, excellent agreements are observed.

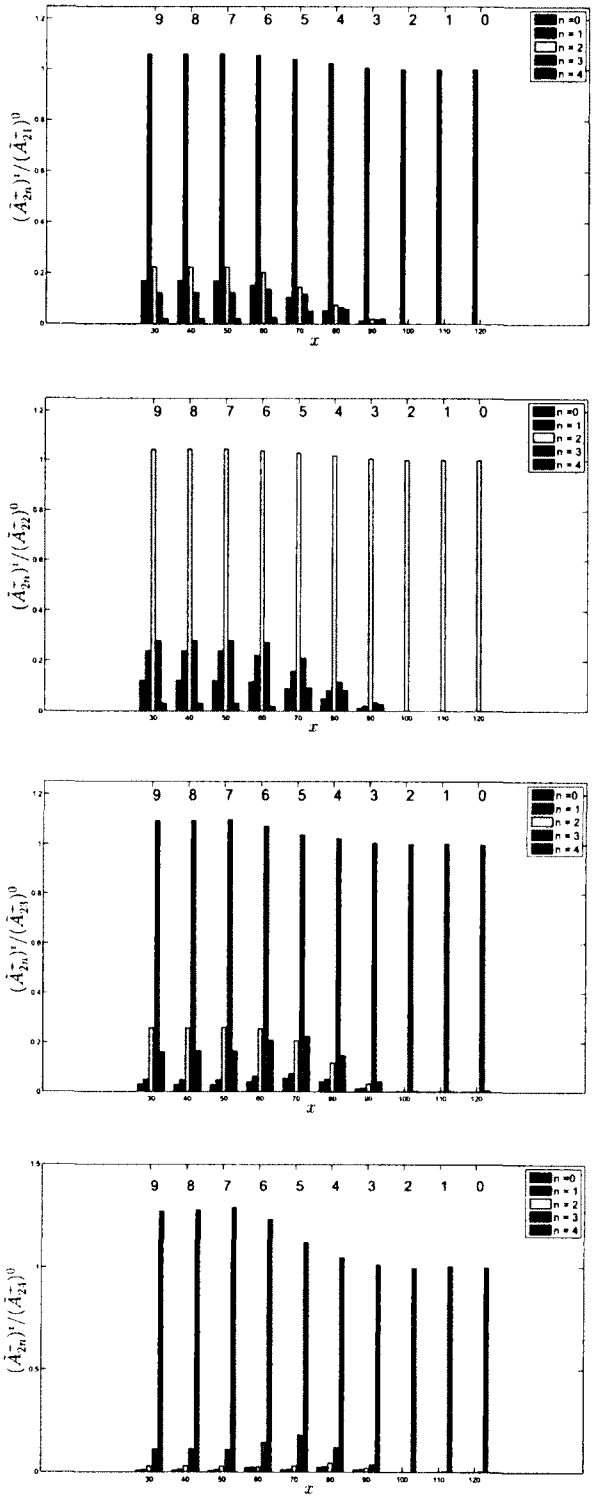

Fig. 51. The normalized amplitudes of left-going modes along the duct for the forced modes $(2,1),(2,2),(2,3),(2,4)$ in the adjoint problem and "i" is the station number from 0 to 9.

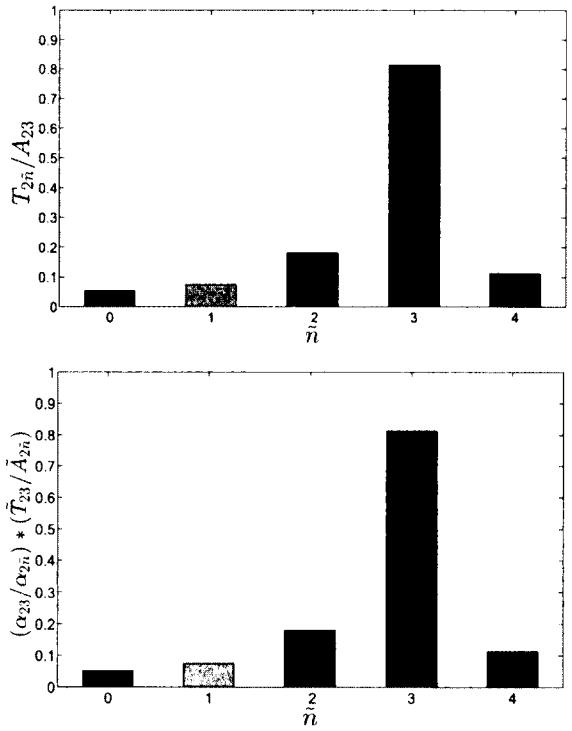

Fig. 52. Demonstration of reciprocity (95).

7.3 RECIPROCITY BETWEEN A POINT SOURCE AND DUCT MODES

We consider Green's function of the adjoint system in 3-D defined by

$$\frac{\partial \tilde{\boldsymbol{w}}}{\partial t} + \tilde{\boldsymbol{L}}(\tilde{\boldsymbol{w}}) = -\delta(\boldsymbol{r} - \tilde{\boldsymbol{r}}')\delta(t - t')\boldsymbol{e}_p$$

with initial condition

$$\tilde{\boldsymbol{w}} = 0, \quad t > t'$$

where $\boldsymbol{r} = (x, y, z)$, $\tilde{\boldsymbol{r}}' = (x', y', z')$ and $\boldsymbol{e}_p = (0, 0, 0, 0, 1)$.

The form of $\boldsymbol{e}_p$ is chosen for the convenience of establishing the reciprocal relations in pressure. Other choices are possible of course.

We study the case where the solution to the Euler equations, a forward problem, will be the one formed by an incoming wave mode inside the duct as shown at the top of Fig. 53. Specifically, let the solutions inside the duct and near the inlet be written in the frequency domain as

$$\boldsymbol{w}(\boldsymbol{r}, t) = \boldsymbol{f}(\boldsymbol{r}, \omega)e^{-i\omega t}$$

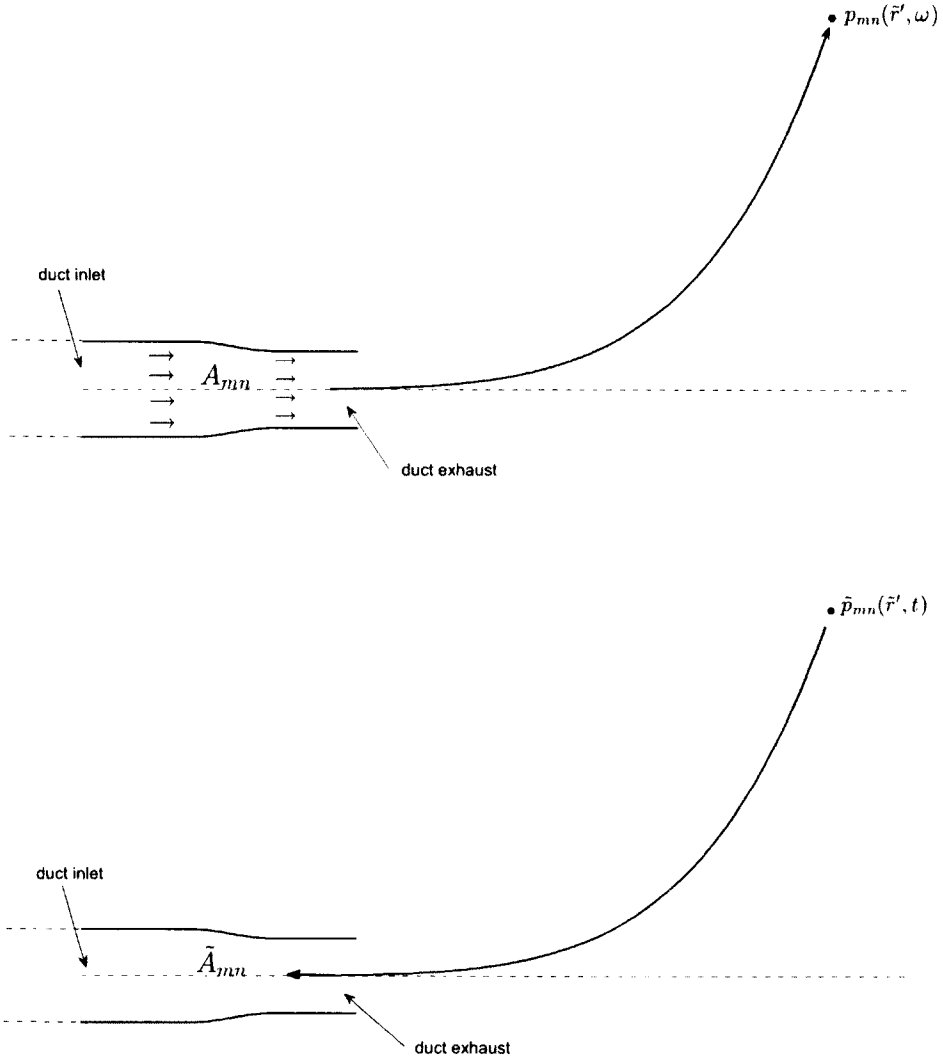

Fig. 53. Schematic diagrams showing the forward (top) and adjoint (bottom) problem.

and

$$\tilde{\boldsymbol{w}}(\boldsymbol{r},t) = \tilde{\boldsymbol{f}}(\boldsymbol{r},\omega)e^{-i\omega t}$$

where, with a local uniform duct assumption, we have

$$\boldsymbol{f}(x,y,z,\omega) = A_{m_0n_0}\phi_{m_0n_0}(y,z)e^{ik^+_{m_0n_0}(\omega)x} + \sum_{m',n'} R_{m'n'}\phi_{m'n'}(y,z)e^{ik^-_{m'n'}(\omega)x} \tag{96}$$

$$\tilde{\boldsymbol{f}}(x,y,z,\omega) = \sum_{m,n} \tilde{A}_{mn}\tilde{\phi}_{mn}(y,z)e^{ik^+_{mn}(\omega)x} \tag{97}$$

in which we have used the fact that eigenvalues of the adjoint system and the Euler equations are identical. Mode (m_0, n_0) is the incoming wave with amplitude $A_{m_0n_0}$, and $R_{m'n'}$ are the reflected wave amplitude of modes (m', n'). The solution to the adjoint system inside the duct is also decomposed into duct modes (m, n) with amplitudes denoted by $\tilde{A}_{mn}$. It is shown at the bottom of Fig. 53. Since it is generated by a point source at the far field, the adjoint solution inside the duct near the inlet region should consist of only left traveling modes. By the results in section (4.2), these left traveling acoustics waves, when solved in the reversed time τ, have the same dispersion relations as the right traveling acoustic waves, as indicated by $ik^+_{mn}(\omega)$ in (97).

In the frequency domain, we have

$$-i\omega\boldsymbol{f} + \boldsymbol{L}(\boldsymbol{f}) = 0 \tag{98}$$

and

$$-i\omega\tilde{\boldsymbol{f}} + \tilde{\boldsymbol{L}}(\tilde{\boldsymbol{f}}) = -\delta(\boldsymbol{r} - \tilde{\boldsymbol{r}}')\boldsymbol{e}_p \tag{99}$$

for the Euler equations and the Green's function of the adjoint system, respectively. By an operation $\tilde{\boldsymbol{f}}^{*T}(98) + \boldsymbol{f}^T(99)^*$, we get

$$\tilde{\boldsymbol{f}}^{*T}\boldsymbol{L}(\boldsymbol{f}) + \boldsymbol{f}^T\tilde{\boldsymbol{L}}(\tilde{\boldsymbol{f}}^*) = -\delta(\boldsymbol{r} - \tilde{\boldsymbol{r}}')\boldsymbol{f}^T\boldsymbol{e}_p$$

where a star indicates the complex conjugate. Using the properties of the adjoint system discussed in Chapter 4, the left hand side becomes a complete divergence and by the integration over a volume V in space, outlined in Fig. 54, we get

$$\int_V \nabla\cdot\boldsymbol{J}(\boldsymbol{f},\tilde{\boldsymbol{f}}^*)dV = -p(\tilde{\boldsymbol{r}}',\omega).$$

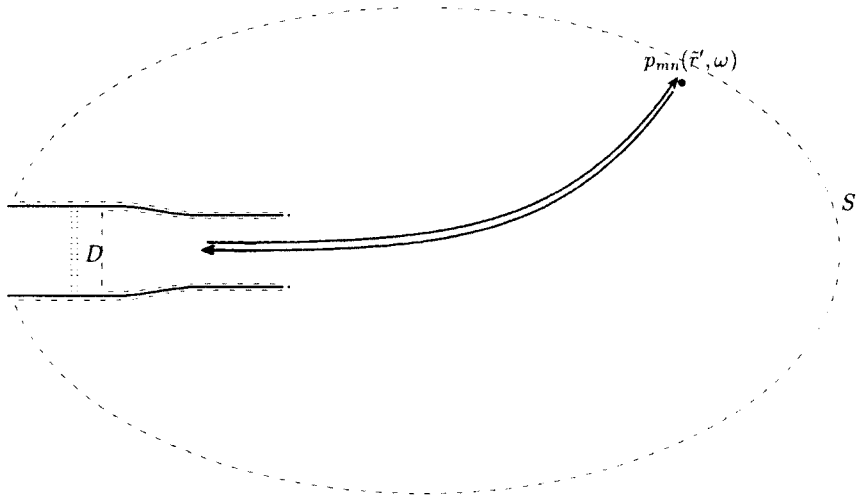

Fig. 54. A schematic diagram of outlined volume.

By again using the divergence theorem and letting the boundary of V in open space go to infinity and applying the wall boundary conditions, we have

$$-\int_D J_x(\boldsymbol{f}, \tilde{\boldsymbol{f}}^*) dS = -p(\tilde{\boldsymbol{r}}', \omega)$$

where D is the area of the cross section at the duct inlet region and J_x is the x component of the flux vector $\boldsymbol{J}$ in the Lagrange identity.

By substituting (96) and (97) into the above equation, due to the orthogonality condition for the eigenfunctions (61), we get

$$\tilde{A}^*_{m_0 n_0} A_{m_0 n_0} \int_D \tilde{\phi}^{*T}_{m_0 n_0} \boldsymbol{A} \phi_{m_0 n_0} \, dS = p(\tilde{\boldsymbol{r}}', \omega). \tag{100}$$

In other words, the adjoint solution can act as a filter for the modal contributions at the far field as noted in [17].

Using the proportionality constant derived earlier, (100) can also be written succinctly as

$$\frac{p(\tilde{\boldsymbol{r}}', \omega)}{A_{m_0 n_0}} = \alpha_{m_0 n_0} \tilde{A}_{m_0 n_0} \tag{101}$$

where the proportionality constant

$$\alpha_{mn} = \int_D \tilde{\phi}^{*T}_{mn} \boldsymbol{A} \phi_{mn} \, dS.$$

Equation (101) is the reciprocal relation between the acoustic pressure $p(\tilde{\boldsymbol{r}}', \omega)$ at $\tilde{\boldsymbol{r}}'$ produced by duct mode (m_0, n_0) and the amplitude $\tilde{A}_{m_0 n_0}$ of that mode inside the duct due to a point source at $\tilde{\boldsymbol{r}}'$ of the adjoint system.

7.4 INITIAL CONDITION FOR THE ADJOINT SYSTEM

For the reciprocal condition (101), a point source is placed at the far field and we also need to solve

$$\frac{\partial \tilde{\boldsymbol{w}}}{\partial t} + \tilde{\boldsymbol{L}}(\tilde{\boldsymbol{w}}) = -\Psi(t - t')\delta(\boldsymbol{r} - \tilde{\boldsymbol{r}}')\boldsymbol{e}_p \tag{102}$$

where $\tilde{\boldsymbol{r}}'$ is a far field observation point, t' is a time of interest, and $\Psi(t)$ is the broadband time function used in the TDWP method. As we used in the previous chapters, function $\Psi(t)$ is non-zero for a finite time duration $-T < t < T$ and is given as

$$\Psi(t) = \frac{\Delta t \sin(w_0 t)}{\pi t} e^{(\ln 0.01)(t/N\Delta t)^2}, \quad |t| \leq N\Delta t$$

where $T = N\Delta t$.

We note that the time domain for which the solution of the adjoint system is nonzero is $t < t' + N\Delta t$. To solve (102) numerically in a time marching fashion, we introduce τ as

$$\tau = t' - t.$$

This leads to the equation for numerical solution as

$$\frac{\partial \tilde{\boldsymbol{w}}}{\partial \tau} - \tilde{\boldsymbol{L}}(\tilde{\boldsymbol{w}}) = -\Psi(-\tau)\delta(\boldsymbol{r} - \tilde{\boldsymbol{r}}')\boldsymbol{e}_p. \tag{103}$$

However, the numerical computational method cannot be carried out here directly because of the delta function in (103). In order to deal with the delta function in the source term in (102), we make use of the exact acoustic solution in a uniform stream and recast (102)as an initial value problem. The details will be described below.

At the far-field where the mean flow is assumed to be uniform, the exact solution to (103) can be found as the adjoint acoustic waves. We will use "(e)" to refer to the exact solution.

Since the source term in (103) becomes zero for $\tau > T$, the equation (103) can be solved as an initial boundary value problem without the source term. We define an

initial condition as

$$\tilde{\boldsymbol{w}}(\boldsymbol{r},\tau)|_{\tau=\tau_0} = \tilde{\boldsymbol{w}}^{(e)}(\boldsymbol{r},\tau)|_{\tau=\tau_0} \tag{104}$$

where τ_0 is any time greater than T.

We will derive exact solutions for 2-D and 3-D separately. For these solutions, the axially uniform mean flow is denoted by M. Then the equations of the adjoint system defined in (103) can be written as

$$\frac{\partial\tilde{\rho}}{\partial\tau} - M\frac{\partial\tilde{\rho}}{\partial x} = 0,$$

$$\frac{\partial\tilde{\boldsymbol{u}}}{\partial\tau} - M\frac{\partial\tilde{\boldsymbol{u}}}{\partial x} - \bar{\rho}\nabla\tilde{\rho} - \gamma\bar{p}\nabla\tilde{p} = 0,$$

$$\frac{\partial\tilde{p}}{\partial\tau} - M\frac{\partial\tilde{p}}{\partial x} - \frac{1}{\bar{\rho}}(\nabla\cdot\tilde{\boldsymbol{u}}) = -\delta(\boldsymbol{r}-\tilde{\boldsymbol{r}}')\Psi(-\tau).$$

We look for the exact solution $\tilde{\boldsymbol{w}}^{(e)}(\boldsymbol{r},\tau)$ to (103) for the density, pressure and velocity components of the adjoint solution as

$$\tilde{\rho}^{(e)}(\boldsymbol{r},\tau) = 0, \tag{105}$$

$$\tilde{p}^{(e)}(\boldsymbol{r},\tau) = \left(\frac{\partial}{\partial\tau} - M\frac{\partial}{\partial x}\right)\tilde{P}^{(e)}(\boldsymbol{r},\tau), \tag{106}$$

$$\tilde{\boldsymbol{u}}^{(e)}(\boldsymbol{r},\tau) = \gamma\bar{p}\nabla\tilde{P}^{(e)}(\boldsymbol{r},\tau). \tag{107}$$

Then, we can get

$$\left(\frac{\partial}{\partial\tau} - M\frac{\partial}{\partial x}\right)^2\tilde{P}^{(e)} - \bar{a}^2\nabla^2\tilde{P}^{(e)} = -\delta(\boldsymbol{r}-\tilde{\boldsymbol{r}}')\Psi(-\tau)$$

where $\bar{a}^2 = \frac{\gamma\bar{p}}{\bar{\rho}}$, $\boldsymbol{r} = (x,y)$ for 2-D and $\boldsymbol{r} = (x,y,z)$ for 3-D.

In order to solve this equation, we need to find out what the Green's function is here. To do that, we can consider the following equation

$$\left(\frac{\partial}{\partial\tau} - M\frac{\partial}{\partial x}\right)^2 G - \bar{a}^2\nabla^2 G = \delta(\boldsymbol{r}-\tilde{\boldsymbol{r}}')\delta(\tau-\tau'). \tag{108}$$

We can also consider a transformation

$$\bar{\tau} = \tau - \beta x$$

where

$$\beta = \frac{M}{\bar{a}^2 - M^2}.$$

After that point, we first derive Green's function and then express $\tilde{P}^{(e)}$ for 2-D. We write a new equation in variables x, y and $\bar{\tau}$ as

$$\left(\frac{\partial}{\partial\bar{\tau}} - M\frac{\partial}{\partial x} + M\frac{\partial}{\partial\bar{\tau}}\right)^2 G - \bar{a}^2\left(\frac{\partial}{\partial x} - \beta\frac{\partial}{\partial\bar{\tau}}\right)^2 G - \bar{a}^2\frac{\partial^2 G}{\partial y^2} = \delta(x-x')\delta(y-y')\delta(\bar{\tau}+\beta x-\tau').$$

It can be simplified to be

$$\frac{\partial^2 G}{\partial\bar{\tau}^2} - \frac{\left(\bar{a}^2 - M^2\right)^2}{\bar{a}^2}\frac{\partial^2 G}{\partial x^2} - \left(\bar{a}^2 - M^2\right)\frac{\partial^2 G}{\partial y^2} = \left[\frac{\bar{a}^2 - M^2}{\bar{a}^2}\times \delta(x-x')\delta(y-y')\delta(\bar{\tau}+\beta x-\tau')\right].$$

Let

$$\alpha = \sqrt{\frac{\bar{a}^2 - M^2}{\bar{a}^2}}, \quad \bar{x} = \frac{x}{\alpha^2}, \quad \bar{y} = \frac{y}{\alpha}$$

and we can use

$$\begin{aligned}\alpha^2\delta(x-x')\delta(y-y') &= \alpha^2\delta(\alpha^2(\bar{x}-\bar{x}'))\delta(\alpha(\bar{y}-\bar{y}')) \\ &= \alpha^2\frac{1}{\alpha^2}\delta(\bar{x}-\bar{x}')\frac{1}{\alpha}\delta(\bar{y}-\bar{y}') \\ &= \frac{1}{\alpha}\delta(\bar{x}-\bar{x}')\delta(\bar{y}-\bar{y}').\end{aligned}$$

We can finally re-write (108) for 2-D as

$$\frac{\partial^2 G}{\partial\bar{\tau}^2} - \bar{a}^2\left(\frac{\partial^2 G}{\partial\bar{x}^2} + \frac{\partial^2 G}{\partial\bar{y}^2}\right) = \frac{1}{\alpha}\delta(\bar{x}-\bar{x}')\delta(\bar{y}-\bar{y}')\delta(\bar{\tau}+\beta x-\tau'). \tag{109}$$

The Green's function for the following equation

$$\frac{\partial^2 g}{\partial t^2} - \bar{a}^2\left(\frac{\partial^2 g}{\partial x^2} + \frac{\partial^2 g}{\partial y^2}\right) = \delta(x-x')\delta(y-y')\delta(t-t')$$

is well-known [18],

$$g(x,y,t;x',y',t') = \frac{H(\bar{a}(t-t') - R(r,r'))}{2\pi\bar{a}\sqrt{\bar{a}^2(t-t')^2 - R^2(r,r')}}$$

where H is the step function and $R(r,r') = \sqrt{(x-x')^2+(y-y')^2}$.
For 2-D, by taking above information and (109) into consideration, we can write the Green's function of (108) as

$$G(x,y,\tau;\tilde{x}',\tilde{y}',\tau') = \frac{1}{2\alpha\pi\bar{a}} \frac{H\left(\bar{a}(\tau-\tau'-\beta(x-\tilde{x}')) - \frac{R(r,\tilde{r}')}{\alpha}\right)}{\sqrt{\bar{a}^2\left(\tau-\tau'-\beta(x-\tilde{x}')\right)^2 - \left(\frac{R(r,\tilde{r}')}{\alpha}\right)^2}} \tag{110}$$

where $R(r,\tilde{r}') = \sqrt{\frac{(x-\tilde{x}')^2}{\alpha^2}+(y-\tilde{y}')^2}$.
By (110), we get

$$\begin{aligned}\tilde{P}^{(e)}(x,y,\tau) &= \int_{-\infty}^{\infty} G(x,y,\tau;\tilde{x}',\tilde{y}',\tau')\Psi(\tau')\,d\tau' \\ &= \int_{-\infty}^{\infty} \frac{1}{2\alpha\pi\bar{a}} \frac{H\left(\bar{a}(\tau-\tau'-\beta(x-\tilde{x}')) - \frac{R(r,\tilde{r}')}{\alpha}\right)\Psi(\tau')}{\sqrt{\bar{a}^2\left(\tau-\tau'-\beta(x-\tilde{x}')\right)^2 - \left(\frac{R(r,\tilde{r}')}{\alpha}\right)^2}}\,d\tau'\end{aligned}$$

$$= \frac{1}{2\alpha\pi\bar{a}} \int_{-T_0}^{\min\left(\tau-\beta(x-\tilde{x}')-\frac{R(r,\tilde{r}')}{\alpha\bar{a}},T_0\right)} \frac{\Psi(\tau')}{\sqrt{\bar{a}^2\left(\tau-\tau'-\beta(x-\tilde{x}')\right)^2 - \left(\frac{R(r,\tilde{r}')}{\alpha}\right)^2}}\,d\tau'$$

where $R(r,\tilde{r}') = \sqrt{\frac{(x-\tilde{x}')^2}{\alpha^2}+(y-\tilde{y}')^2}$.
Secondly, we derive the Green's function and then find $\tilde{P}^{(e)}$ for 3-D. We can express (108) in terms of x, y, z and $\bar{\tau}$ as

$$\left(\frac{\partial}{\partial\bar{\tau}} - M\frac{\partial}{\partial x} + M\frac{\partial}{\partial\bar{\tau}}\right)^2 G - \bar{a}^2\left(\frac{\partial}{\partial x} - \beta\frac{\partial}{\partial\bar{\tau}}\right)^2 G - \bar{a}^2\left(\frac{\partial^2 G}{\partial y^2} + \frac{\partial^2 G}{\partial z^2}\right) =$$
$$\delta(x-x')\delta(y-y')\delta(z-z')\delta(\bar{\tau}+\beta x-\tau').$$

It can be simplified to be

$$\frac{\partial^2 G}{\partial\bar{\tau}^2} - \frac{(\bar{a}^2-M^2)^2}{\bar{a}^2}\frac{\partial^2 G}{\partial x^2} - (\bar{a}^2-M^2)\left(\frac{\partial^2 G}{\partial y^2} + \frac{\partial^2 G}{\partial z^2}\right) =$$
$$\frac{\bar{a}^2-M^2}{\bar{a}^2}\delta(x-x')\delta(y-y')\delta(z-z')\delta(\bar{\tau}+\beta x-\tau').$$

Let

$$\alpha = \sqrt{\frac{\bar{a}^2-M^2}{\bar{a}^2}}, \quad \bar{x} = \frac{x}{\alpha^2}, \quad \bar{y} = \frac{y}{\alpha} \quad \bar{z} = \frac{z}{\alpha}$$

and

$$\begin{aligned}\alpha^2\delta(x-x')\delta(y-y') &= \alpha^2\delta(\alpha^2(\bar{x}-\bar{x}'))\delta(\alpha(\bar{y}-\bar{y}'))\delta(\alpha(\bar{y}-\bar{y}')) \\ &= \alpha^2\frac{1}{\alpha^2}\delta(\bar{x}-\bar{x}')\frac{1}{\alpha}\delta(\bar{y}-\bar{y}')\frac{1}{\alpha}\delta(\bar{z}-\bar{z}') \\ &= \frac{1}{\alpha^2}\delta(\bar{x}-\bar{x}')\delta(\bar{y}-\bar{y}')\delta(\bar{z}-\bar{z}').\end{aligned}$$

Then, we get

$$\frac{\partial^2 G}{\partial\bar{\tau}^2} - \bar{a}^2\left(\frac{\partial^2 G}{\partial\bar{x}^2}+\frac{\partial^2 G}{\partial\bar{y}^2}+\frac{\partial^2 G}{\partial\bar{z}^2}\right) = \frac{1}{\alpha^2}\delta(\bar{x}-\bar{x}')\delta(\bar{y}-\bar{y}')\delta(\bar{z}-\bar{z}')\delta(\bar{\tau}+\beta x-\tau'). \tag{111}$$

The Green's function for the the following equation

$$\frac{\partial^2 g}{\partial t^2} - \bar{a}^2\left(\frac{\partial^2 g}{\partial x^2}+\frac{\partial^2 g}{\partial y^2}+\frac{\partial^2 g}{\partial z^2}\right) = \delta(x-x')\delta(y-y')\delta(z-z')\delta(t-t')$$

is well-known [18],

$$g(x,y,t;x',y',t') = \frac{1}{4\pi\bar{a}R(r,r')}\delta(R(r,r')-\bar{a}(t-t'))$$

where δ is the delta function and $R(r,r') = \sqrt{(x-x')^2+(y-y')^2+(z-z')^2}$.
For 3-D, by taking the above information and (111) into consideration, we can write the Green's function of (108) as

$$\begin{aligned}G(x,y,z,\tau;\tilde{x}',\tilde{y}',\tilde{z}',\tau') &= \frac{1}{4\alpha^2\pi\bar{a}}\frac{\delta\left(\frac{R(r,\tilde{r}')}{\alpha}-\bar{a}\left(\tau-\tau'-\beta(x-\tilde{x}')\right)\right)}{\frac{R(r,\tilde{r}')}{\alpha}} \\ &= \frac{1}{4\alpha\pi\bar{a}}\frac{\delta\left(\frac{R(r,\tilde{r}')}{\alpha}-\bar{a}\left(\tau-\tau'-\beta(x-\tilde{x}')\right)\right)}{R(r,\tilde{r}')}\end{aligned} \tag{112}$$

where $R(r,\tilde{r}') = \sqrt{\frac{(x-\tilde{x}')^2}{\alpha^2}+(y-\tilde{y}')^2+(z-\tilde{z}')^2}$.
By (112), we get

$$\begin{aligned}\tilde{P}^{(e)}(x,y,z,\tau) &= \int_{-\infty}^{\infty} G(x,y,z,\tau;\tilde{x}',\tilde{y}',\tilde{z}',\tau')\,d\tau' \\ &= \int_{-\infty}^{\infty}\frac{1}{4\alpha\pi\bar{a}}\frac{\delta\left(\frac{R(r,\tilde{r}')}{\alpha}-\bar{a}\left(\tau-\tau'-\beta(x-\tilde{x}')\right)\right)\Psi(\tau')}{R(r,\tilde{r}')}\,d\tau' \\ &= \frac{1}{4\alpha\pi\bar{a}R(r,\tilde{r}')}\int_{-\infty}^{\infty}\delta\left(\frac{R(r,\tilde{r}')}{\alpha}-\bar{a}\left(\tau-\tau'-\beta(x-\tilde{x}')\right)\right)\Psi(\tau')\,d\tau' \\ &= \frac{\Psi\left(-\tau+\beta(x-\tilde{x}')+\frac{R(r,\tilde{r}')}{\alpha\bar{a}}\right)}{4\alpha\pi\bar{a}R(r,\tilde{r}')}\end{aligned}$$

where $R(r,\tilde{r}') = \sqrt{\frac{(x-\tilde{x}')^2}{\alpha^2} + (y-\tilde{y}')^2 + (z-\tilde{z}')^2}$.
After deriving formula $\tilde{P}^{(e)}$ for any τ, it is easy to find out $\tilde{p}^{(e)}$ and $\tilde{\boldsymbol{u}}^{(e)}$ by (106) and (107) for 2-D and 3-D cases, respectively.

In this section, we also make a comparison between exact and computational solutions. First, exact solutions are calculated for pressure and velocity components at $t = 22$. Second, we start to run a simulation at the same time to solve (102) with initial condition by using exact solutions. In Fig. 55, pressure contours at $t = 28$ is shown.

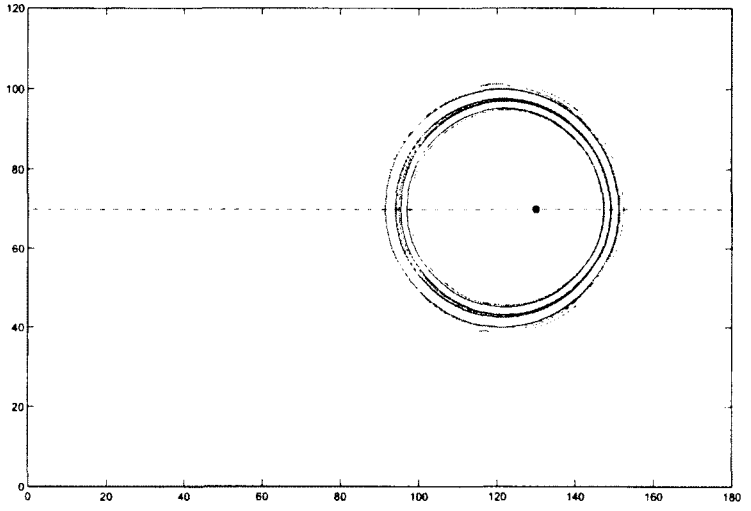

Fig. 55. Pressure contours at time $t = 28$ of the adjoint solution and the source point at $(130, 70)$.

In Fig. 56, the numerical solution at a later time $t = 28$ is compared with the exact pulse solution given in (105)-(107). Although any mean flow can be chosen for computations, we use a Mach number 0.3. The comparisons of pressures and velocities are shown along with a dashed line given in Fig. 55. The good agreement between the computed and theoretical solutions indicates that the initial state given in (104) has been implemented correctly.

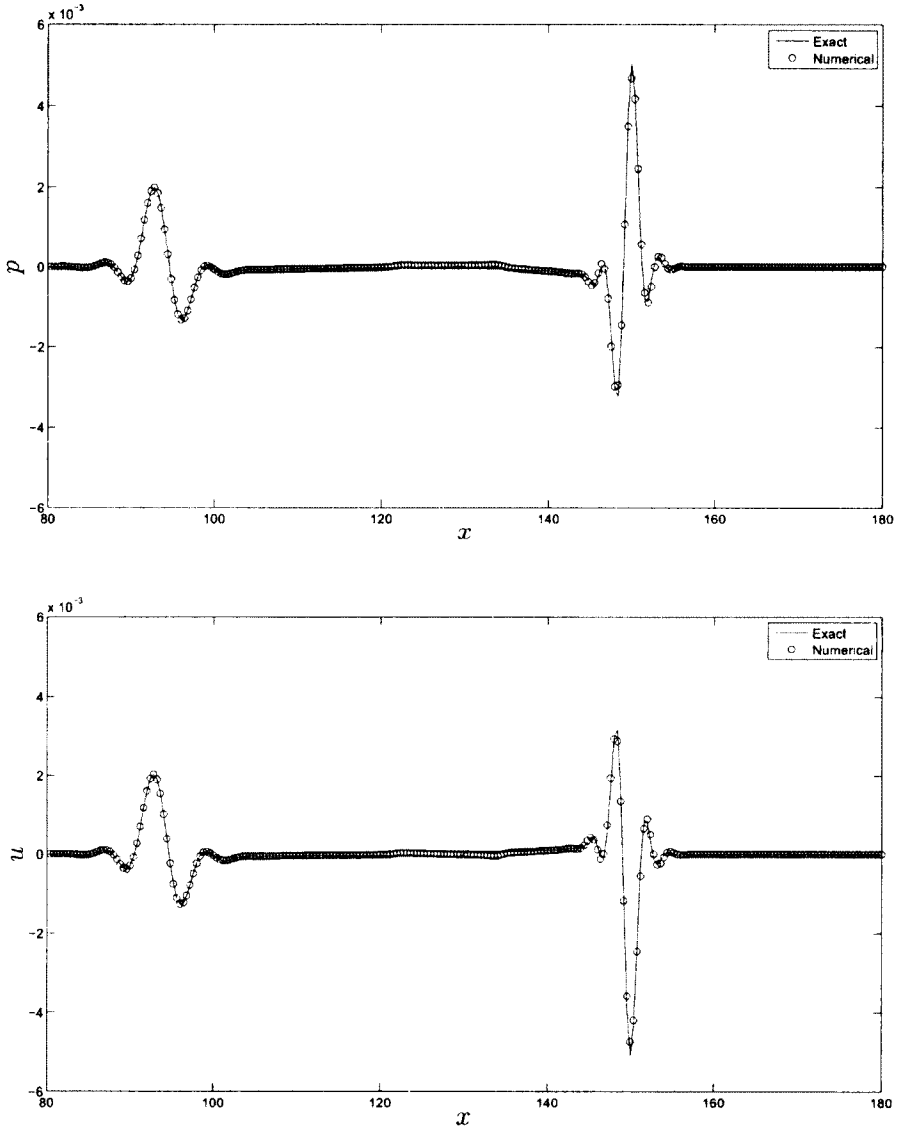

Fig. 56. Pressure (top) and u-velocity (bottom) at time $t = 28$ of the adjoint solution.

7.5 NUMERICAL RESULTS FOR 2-D OPEN DUCT

In this section, a non-uniform duct that consists of two uniform sections connected by a smooth transition region will be used for all computations and simulations. We put a non-uniform duct into an open domain to get a reciprocal relation between a point source and duct modes. It will be called an open duct case. The main computational domain and mesh used in the simulations are shown in Fig. 57. We fit the meshes for three zones. In other words, the computational domain includes three sub-domains. These divisions are labeled by (1), (2) and (3) in the same figure. Perfectly Matched Layer (PML) absorbing boundary conditions are applied at all the non-reflecting boundaries of all four sides of the main computational domain, including the one at the left hand side inside of the duct.

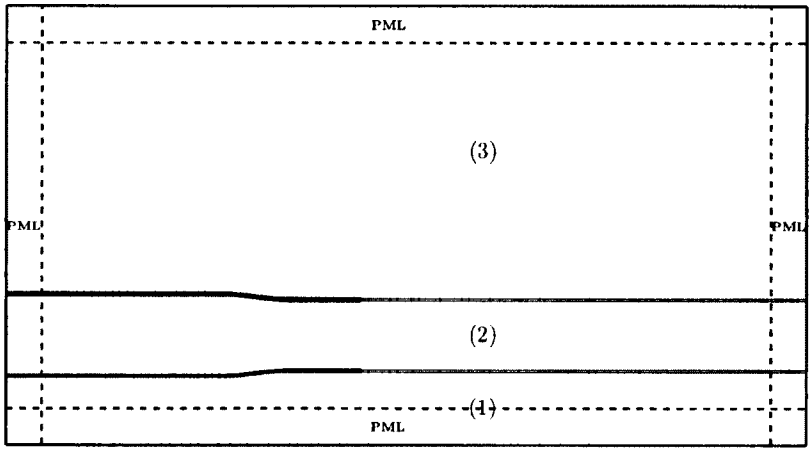

Fig. 57. Computational domain and mesh for the time domain solution with PML at all non-reflecting boundaries.

The mean flow inside the duct will be approximated by a one-dimensional compressible flow as we did in section 5.1. There are exiting flows outside of the duct. We assume that there is a shear layer outside of the duct as shown in Fig. 58. For simplicity, an empirical function is used for the mean flow distributions after leaving

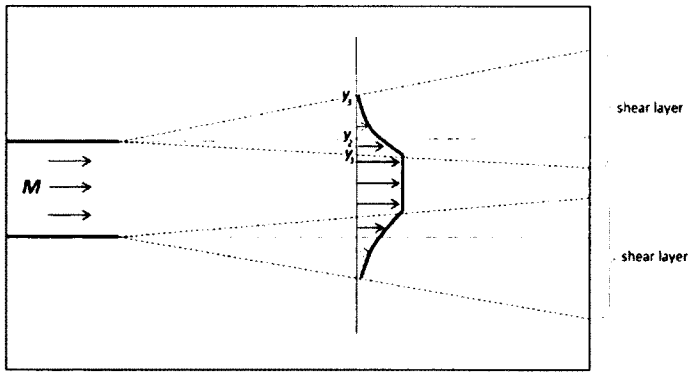

Fig. 58. Schematic diagram of shear layers.

the duct as

$$F(y) = \begin{cases} 1 & y \le y_1 \\ e^{\left(-\ln 2 \cdot (\frac{y+y_1}{b})^2\right)} & y_1 < y < y_2 \\ 0.5 & y = y_2 \\ e^{\left(-\ln 2 \cdot (\frac{y-y_1}{b})^2\right)} & y_2 < y \le y_3 \end{cases} \tag{113}$$

where y_1, y_2 and y_3 are shown in Fig. 58 and $b = y_2 - y_1$.

In Fig. 59, we show a plot of the function (113). For the exhaust flow outside of the duct, the mean flow distribution can be obtained by (113) in the top shear layer. The contours of the mean axial flow with a Mach number M over the entire computational domain are shown in Fig. 60. We will use this mean flow distribution for all Euler and adjoint equation computations.

A TDWP method is again used to carry out simulation for the Euler equations and the adjoint system. In Fig. 61, the computational domain is sketched. It shows the source location ($\diamond$) inside the duct and the far-field observation locations 1, 2 and 3 for the Euler system. These observation locations are also used as a point source for an adjoint system. Three finite difference domains are used to cover (1) the bottom exterior region, (2) the region inside the duct and its extended uniform part and (3) the top exterior region that is extended to include the far field observation

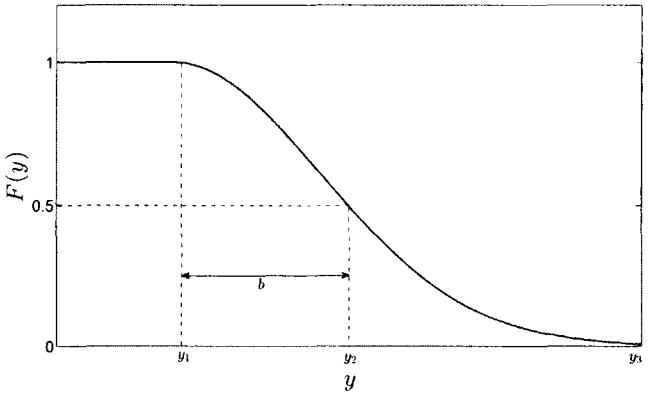

Fig. 59. A function $F(y)$ as an example of the distribution function for the shear layer.

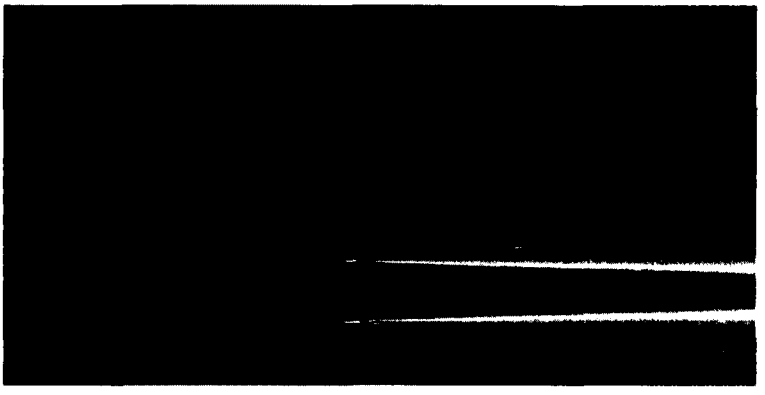

Fig. 60. Mean axial velocity distribution inside and outside of the duct.

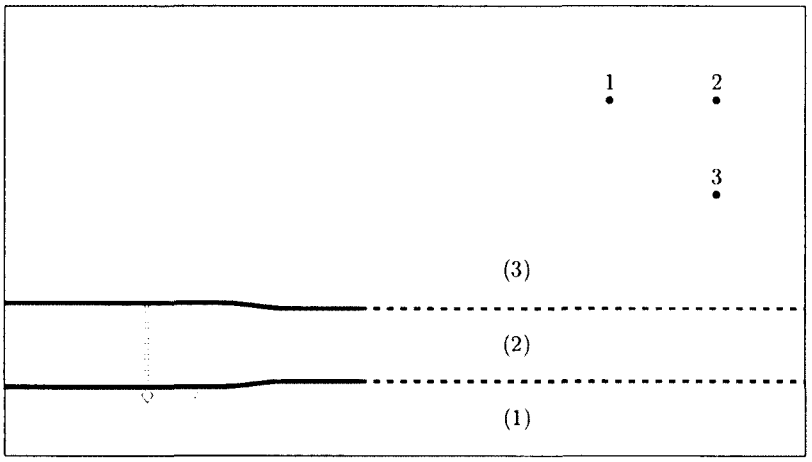

Fig. 61. Computational domain for the Euler and the adjoint system.

points. A time domain finite difference scheme is used for both systems. The spatial derivatives are approximated by a 7-point stencil as in the Dispersion Relation Preserving (DRP) scheme. While applying a 7-point stencil DRP scheme to compute the derivative at a point, if this point is close to the edge of the region, some points in the near by region are required to carry out the computation. A visual example of what we mean about the requirement of some points from another region is shown in Fig. 62. This figure shows clearly how the regions are connected in one computation. Assume that we compute the derivative at a point in region (3) that is the one of the points closest to region (2). To do that, we need three points from region (2). Of course, this is only needed for computational domains outside of the duct.
Time integration is carried by the Low Dissipation and Low Dispersion Runge-Kutta scheme (LDDRK56).
We can start by giving some results for the forward problem. A time sequence of sample instantaneous pressure contours for the forward problem at $t = 500\Delta t, 1000\Delta t, 1500\Delta t$ and $2000\Delta t$ are shown in Fig. 63. These simulations are carried out for $M = 0.3$ and the forced mode $(0, 2)$. The hydrodynamic instability wave is not very strong due the rapid spreading of the shear flow. At $t = 2000\Delta t$, there are barely visible just around the corners of the duct, but it does not affect

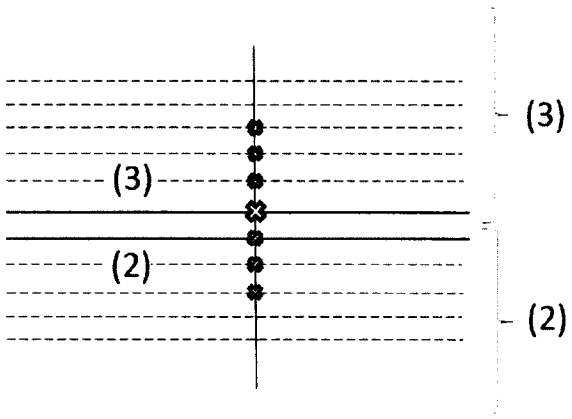

Fig. 62. An example of the connected domains.

simulations much. At all the non-reflecting boundaries, out-going waves are numerically absorbed by the PML without any visible reflection.

For the adjoint problem, we show the results where point number two in Fig. 61 is used as a point source. We first use equations (105)-(107) to get exact solutions at $t_0 = 210\Delta t$. The external flow has no Mach number. While calculating exact solutions we have to be sure that the exact solution does not reach the shear layer at the chosen time t_0, since the Mach number is not zero inside the shear layer. Then, by using exact solutions we run the adjoint system as an initial value problem.

The hydrodynamic instability wave is stronger in the adjoint simulation. As the time progress, the growth of the instability waves becomes significant. To deal with a growing instability, we use the Mean Flow Gradient Removal (MFGR) method. We know that when the mean flow profile u_x has an inflection point, the term $\frac{\partial u_x}{\partial y}$ in matrix $\tilde{D}$ is responsible for the Kelvin-Helmhotz instability waves. A simple and frequently used tactic to void the instability waves is to remove this term from the matrix. Since a wave packet used in TDWP method is temporarily compact, it is possible to separate the acoustic and instability waves. Therefore, the instability wave suppression technique is applied after the wave packet has propagated through the shear layers. This modification helps to reduce instability waves and does not effect adversely on the acoustic waves.

A time sequence of pressure contours at $t = 225\Delta t, 900\Delta t, 1250\Delta t, 1700\Delta t$ is shown

in Fig. 64. On the second contour, we can see that the simulation has already entered the shear layer since some parts of the waves travel faster than other parts. The Time Domain Wave packet is reflected by the top side of the duct as well as propagated into the duct. They can easily be seen on the third and forth contour graphs.

The frequency domain solutions of forward and adjoint equations at the frequency $\pi/5$, obtained by an FFT of the time domain solutions for both system, are plotted in Fig. 65. As noted earlier, the solutions at other frequencies are also available in the same computations.

In order to demonstrate the reciprocal relations or validate reciprocal condition (101) between the duct modes and a point source, we can carry out the TDWP method simulations for the forward and adjoint problem. For the forward problem, the forced mode has to be specified. For the forward and adjoint problems, the station where we use modal decomposition to find the amplitude of the duct mode (m, n) is marked by $(\triangle)$ in Fig. 61. As illustrated in Fig. 53, we need to find the amplitude of the duct mode (m, n) propagating toward the exhaust plane for the forward problem and amplitude of the duct mode (m, n) of the wave coming from the point source and propagating toward the left absorbing boundary inside the duct for the adjoint problem. Computations are presented for the forced modes $(0, 1), (0, 2), (0, 3)$ and $(0, 4)$ with Mach number 0.3 and are recorded at three far field observation points for the forward problem. The obtained pressure time domain solutions of the observation points are converted to frequency domain solutions by FFT.

To compare with far field experimental results, and to demonstrate the reciprocal relations between the forward and adjoint problem, we show in Fig. 66 (top) the far field pressure amplitudes at the observation points corresponding to each propagating radial mode of the duct. It is shown that the far field amplitude, $p(\tilde{\boldsymbol{r}}', \omega)/A_{mn}$, is produced by the indicated duct mode normalized by the mode incoming amplitude. The duct input mode is indicated by the color and observation points as defined in Fig. 61 are indicated by numbers on the x-axis. In Fig. 66 (bottom), we show the modal decomposition of the adjoint system where the far field source location is as indicated. It is shown that the proportionality constant multiplied by the modal amplitudes, $\alpha_{mn}\tilde{A}_{mn}$, of the adjoint problem when a point source is placed at the corresponding far field observation point. The relative strengths of the radial mode are clearly similar to those predicted by the reciprocal condition (101). The

comparison that is shown in Fig. 66 seems satisfactory for every mode and its corresponding observation points.

Due to reciprocity, solutions of the adjoint problem serve to validate those of the forward problem. If the number of observation points is smaller than the number of possible propagating duct modes, using the adjoint system is more efficient. On the other hand, when the number of the forced duct modes is less than the number of observation points, the forward solution can be more beneficial.

In this chapter, the reciprocal relation between duct modes in a closed non-uniform duct was derived. This relation was also validated by numerical computations which were carried out by the TDWP method simulations for five different forced modes. For the non-uniform duct in an open domain, which is called open duct, a reciprocal relation between a point source and duct modes was derived. For the adjoint problem, the exact acoustic solution was defined in a uniform stream. Later, we simulated the adjoint problem as an initial value problem without the source term to get numerical solutions. In 2-D, the reciprocity between a point source and duct modes was validated 12 times. This is done by carrying out the TDWP method simulations for four forced modes for the forward problem and for three point sources/observation points for the adjoint problem in the presence of Mach number $M = 0.3$. Besides being a useful tool in validating numerical solutions, we showed that using the adjoint system is more efficient than computing the far field directivity for each forced duct mode when the number of observation points is smaller that the number of possible propagating duct modes.

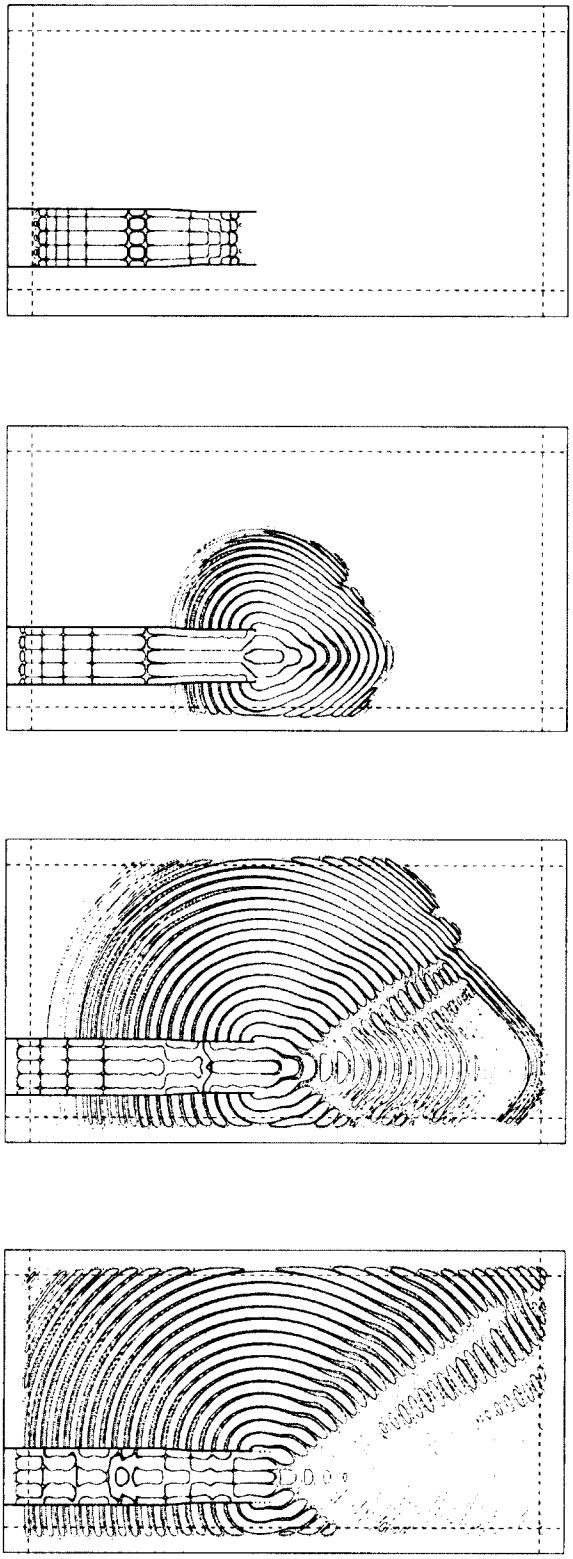

Fig. 63. Instantaneous pressure contours at $t = 500\Delta t, 1000\Delta t, 1500\Delta t, 2000\Delta t$.

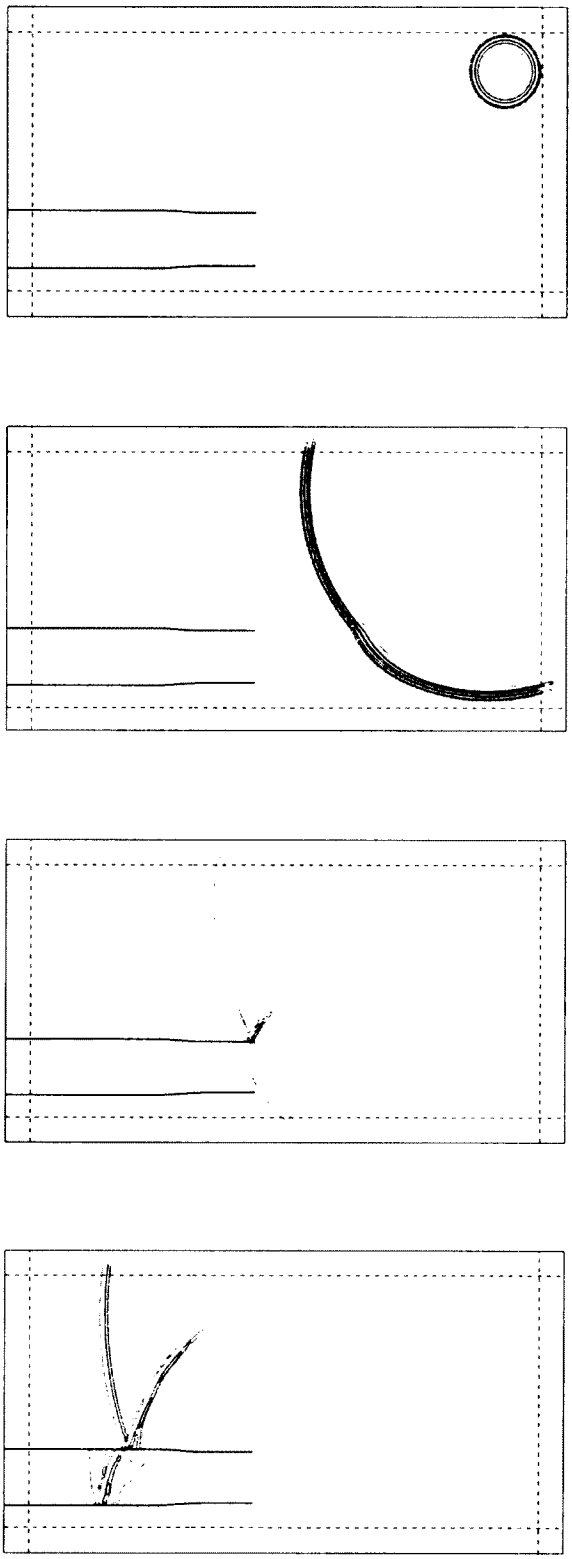

Fig. 64. Contours of pressure at four chosen moments of the adjoint solution for a broadband point source.

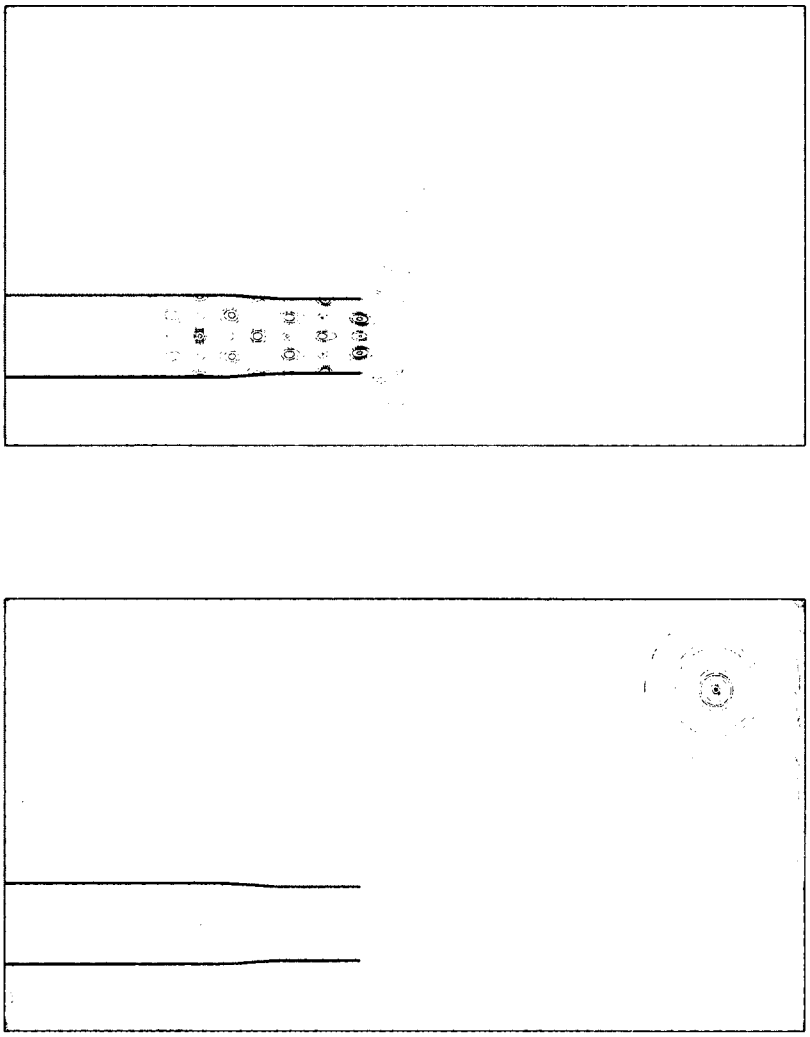

Fig. 65. Frequency domain pressure contours of forward (top) and adjoint (bottom) at frequency ($\pi/5$) by FFT of the time domain solutions given in Figs. 63 and 64.

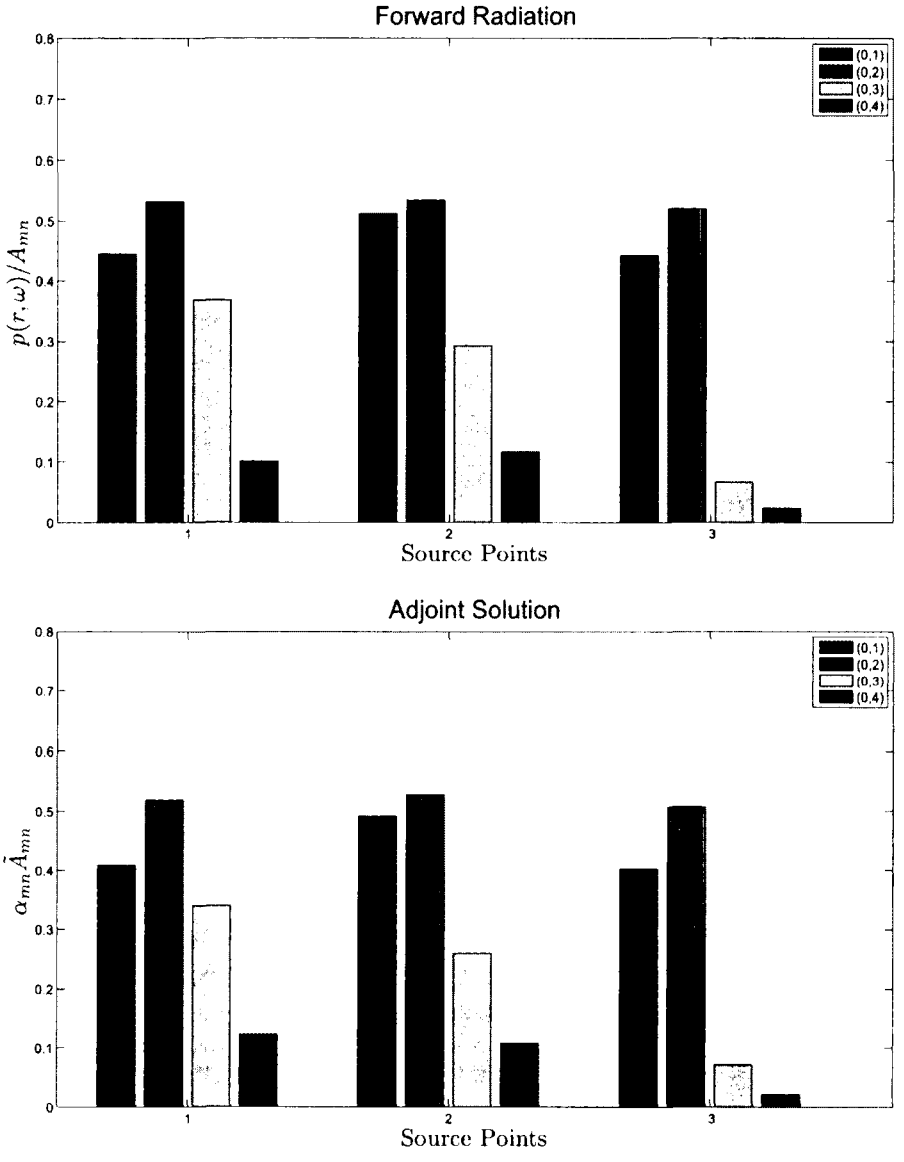

Fig. 66. Demonstration of reciprocity between point sources and their corresponding duct modes.

CHAPTER 8

CONCLUSIONS

In computational aeroacoustics (CAA), global properties of the sound waves are often of help in the comprehension of the solutions, making a validation in numerical solutions and finding efficient numerical methods to get solutions. Hence, the main objective of this thesis was to formulate and develop a reciprocal relation between the linearized Euler equations and their adjoint system that could be easily applied to closed and open ducts.

In this thesis, a new efficient and effective approach for time domain solutions, the Time Domain Wave Packet (TDWP) method, has been studied. The TDWP method is generally more efficient than the conventional single frequency sinusoidal wave approach in time domain. Implementation of a source term modeled by the TDWP method in the linearized Euler equation has been investigated and analyzed for axial uniform mean flow inside the rectangular duct with solid walls, and the provided analytical solution by the Green's function could be used to check accuracy of numerical simulations. A FFT of the computed pressure time signal at a fixed point was also compared with the Fourier transform of the pressure expressed as analytical solution at the same fixed point. To understand propagation of sound inside the duct, the amplitudes of the cut-on duct modes were computed by modal decomposition method. The TDWP method's ability of computing acoustic radiation at all frequencies in a single time domain computation should be particularly useful for solving aeroacoustic problem involving broadband noise sources. It was discovered that the half-width of the exponential function which is one of the terms we use to model the source function should be chosen appropriately to obtain solutions at all frequencies in a single computation.

Adjoint system for the linearized Euler equations in the Cartesian coordinates have been derived and studied in the time domain. A relation between the acoustics solution of the Euler and adjoint equations in a uniform mean flow is given and it is further shown, under a local uniform flow assumption, that the linear waves in the two systems have the same dispersion relations and their eigenfunctions are orthogonal. Application of the TDWP method to adjoint system for the rectangular

duct with solid walls shows that the adjoint system is just the backward problem of the Euler equations.

Applications of the TDWP method has been extended to closed non-uniform ducts with solid walls for the Euler and adjoint system. Here, the area-velocity relation could be simply demonstrated by considering a one-dimensional isentropic flow through a varying area channel. Although the mean velocity is axially uniform at the duct inlet, it varies along the non-uniform duct. All of the results by TDWP method presented have been obtained with a two-dimensional and three-dimensional geometry. After making modal analysis for the cut-on duct modes, it is shown that computing sound propagation by solving the linearized Euler equations and their adjoint system provides accurate solutions.

A reciprocal relation for transmitted waves inside the non-uniform duct has been derived in the presence of the mean flow in three-dimensions. After simulations for both system were carried out by TDWP method for specific incident modes, excellent agreements are observed. By reciprocity, numerical solutions of the adjoint system can be used to validate the Euler equations' numerical solutions. A reciprocal relation between the in-duct propagating modes and the far-field pressure field has also been derived in the presence of the mean flow. Furthermore, techniques for computing the adjoint Green's function by the Time Domain Wave Packet method presented for two-dimension and three-dimension, separately. In two-dimension, numerical results for the TDWP method simulations of both systems are shown where the reciprocal relation has been demonstrated. Combined with the Mean Flow Gradient Removal (MFGR) technique, the TDWP method could avoid the instability waves through a separation of the acoustic wave packet and the instability waves in the simulation of adjoint system. Good numerical accuracy has been observed in the validation of reciprocal relation derived in the thesis.

REFERENCES

[1] M. Abom, Modal decomposition in ducts based on transfer function measurements between microphone pairs, J. Sound Vib. 135(l) (1989) 95-114

[2] C. Bailly, D. Juve, Numerical solution of acoustic propagation problems using linearized Euler equations, AIAA Journal 38 (2000) 22-29

[3] E. Becache, S. Fauqueux, P. Joly, Stability of perfectly matched layers, group velocities and anisotropic waves, J. Comput. Phys. 188 (2003) 399-433

[4] C. Bogey, A. Bailly, D. Juv'e, Computation of flow noise using the source terms in linearized Euler equations, AIAA Journal 40(2) (2002) 235-243

[5] R.H. Cantrell, R.W. Hart, Interaction between sound and flow in acoustic cavities: mass, momentum, and energy considerations, J. Acoust. Soc. Am. 36(4) (1963)

[6] Y-C. Cho, Reciprocity principle in duct acoustics, J. Acoust. Soc. Am. 67(5) (1980)

[7] W.O. Criminale, T.L. Jackson, R.D. Joslin, Theory and Computation of Hydrodynamic Stability, Cambridge University Press, 2003

[8] P.G. Drazin, W.H. Reid, Hydrodynamic Stability, Cambridge University Press, 2004

[9] D.J. Duffy, Green's Function with Applications, Chapman and Hall/CRC, 2001

[10] W. Eckhaus, Studies in Nonlinear Stability, Springer, 1965

[11] L. Euler, General principles of the motion of fluids (Truesdell, Rational Fluid mechanics, 1687-1765, eq.99) 1755

[12] L. Euler, Principles of the motion of fluids (Truesdell, Rational Fluid mechanics, 1687-1765, eq.60) 1752

[13] W. Everseman, A reciprocal relation for transmission in non-uniform hard walled ducts without flow, J. Sound Vib. 47 (1976) 515-521

[14] J.B. Freund, Adjoint-based optimization for understanding and suppressing jet noise, J. Sound Vib. 330 (2011) 4114-4122

[15] O.A. Godin, Reciprocity and energy conservation within the parabolic approximation, Wave Motion 29 (1999) 175-194

[16] C.E. Grosch, H.Salwen, The continuous spectrum of the Orr-Sommerfeld equation. Part 1. The spectrum and the eigenfunctions, J. Fluid Mech. 87 (1978) 33-54

[17] L.J Heidelberg, Fan noise source diagnostic test-tone modal structure results, NASA TM 2002-211594, 2002

[18] J.H. Heinbockel, Mathematical Methods for the Partial Differential Equations, Trafford, 2003

[19] D.C. Hill, Adjoint system and their role in the receptivity problem for boundary layers, J. Fluid Mech. 292 (1995) 183-204

[20] M.S. Howe, The generation of sound by aerodynamic sources in an inhomogeneous steady flow, J. Fluid Mech. 67 (1975) 597-610

[21] F.Q. Hu, A Perfectly Matched Layer absorbing boundary condition for the Euler equations with a non-uniform mean flow, J. Comput. Phys. 208 (2005) 469-492

[22] F.Q. Hu, A stable, Perfectly Matched Layer for linearized Euler equations in unsplit physical variables, J. Comput. Phys. 173 (2001) 455-480

[23] F.Q. Hu, M.Y. Hussaini, J.L. Manthey, Low-dissipation and low-dispersion Runge-Kutta schemes for computational acoustics, J. Comput. Phys. 124 (1996) 177-191

[24] F.Q. Hu, X. Li, X. Li, M. Jiang, Time domain wave packet method and suppression of instability waves in aeroacoustic computations, AIAA paper 2011-2891, 2011

[25] J.E.A. John, Gas Dynamics, Allyn and Bacon Series, 1969

[26] L.E. Kinsler, A.R. Frey, A.B. Coppens, J.V. Sanders, Fundamentals of Acoustics, John Wiley and Sons, 2000

[27] J.J. Knab, Interpolation of band-limited functions using the approximate prolate series, IEEE Transactions in Information Theory 25 (1979) 717-720

[28] L.S.G. Kovasznay, Turbulence in supersonic flow, Journal of the Aeronautical Sciences 20(10) (1953) 657-674

[29] X.D. Li, J.H. Gao, D. Eschricht, F. Thiele, Numerical computation of the radiation and refraction of sound waves through a two dimensional shear layer, NASA CP 2004-212954 (2004) 159-164

[30] H.W. Liepmann, A. Roshko, Elements of Gasdynamics, John Wiley and Sons, 1962

[31] D.K. Lin, X.D. Li, F.Q. Hu, Absorbing boundary condition for nonlinear Euler equations in primitive variables based on the Perfectly Matched Layer technique, Computers and Fluids 40 (2011) 333-337

[32] R.R. Mankbadi, R. Hixon, S.H. Shih, L.A. Povinelli, Use of linearized Euler equations for supersonic jet noise prediction, AIAA Journal 36(2) (1998) 140-147

[33] W. Mohring, Acoustic energy flux in nonhomogeneous ducts, J. Acoust. Soc. Am. 64(4) (1978)

[34] W. Mohring, Energy conservation, time-reversal invariance and reciprocity in ducts with flow, J. Fluid Mech. 431 (2001) 223-237

[35] W. Mohring, On energy, group velocity and small damping of sound waves in ducts with shear flow, J. Sound Vib. 29 (1973) 93-101

[36] C.L. Morfey, Acoustic energy in non-uniform flows, J. Sound Vib. 14(2) (1971) 159-170

[37] C.L. Morfey, Sound transmission and generation in ducts with flow, J. Sound Vib. 14(1) (1971) 37-55

[38] P.M. Morse, K.U. Ingard, Theoretical Acoustics, McGraw-Hill, 1980

[39] A.H. Nayfeh, J.E. Kaiser, D.P. Telionis, Acoustics of aircraft engine-duct systems AIAA Journal 13(2) (1975) 130-153

[40] A.D. Pierce, Acoustics: An introduction to its physical principles and applications, the Acoustical Society of America, 1989

[41] Lord Rayleigh, The Theory of Sound, Dover Publications, 1945

[42] S.W. Rienstra, Sound propagation in slowly varying lined flow ducts of arbitrary cross-section, J. Fluid Mech. 495 (2003) 157-173

[43] S.W. Rienstra, Sound transmission in slowly varying duct circular and annular lined ducts with flow, J. Fluid Mech. 380 (1999) 279-296

[44] M. Salikuddin, R. Ramakrishnana, Acoustic power measurement for single and annular stream duct-nozzle system utilizing a modal decomposition scheme, J. Sound Vib. 113(3) (1987) 441-472

[45] H. Salwen, C.E. Grosch, The continuous spectrum of the Orr-Sommerfeld equation. Part 2. Eigenfunction expansions, J. Fluid Mech. 104 (1981) 445-465

[46] T. Schultz, L.N. Cattafesta III, M. Sheplakb, Modal decomposition method for acoustic impedance testing in square ducts, J. Acoust. Soc. Am. 120(6) (2006)

[47] C.K.W. Tam, L. Auriault, Mean flow refraction effects on sound radiated from localized sources in a jet, J. Fluid Mech. 370 (1992) 145-174

[48] C.K.W. Tam, J.C. Webb, Dispersion relation preserving finite difference schemes for computational acoustics, J. Comput. Phys. 107 (1993) 262-281

[49] C.A. Wagner, T. Hüttl, P. Sagaut , Large-Eddy Simulation for Acoustics, Cambridge University Press, 2007

[50] G.B. Whitman, Linear and Nonlinear Waves, Wiley-Interscience, 1974

VITA

Ibrahim Kocaogul
Department of Computational and Applied Mathematics
Old Dominion University
Norfolk, VA 23529

Education

- Ph.D. in Computational and Applied Mathematics, Old Dominion University, Norfolk, VA (May 2014)
- M.S. in Mathematics, Fatih University, Istanbul, Turkey (June 2005)
- B.S. in Mathematics, Fatih University, Istanbul, Turkey (June 2002)

Publications and Published Abstracts

- **Ibrahim Kocaogul** & Fang Q. Hu, Adjoint problem in duct acoustics and its reciprocity to forward problem by the Time Domain Wave Packet method, APS March Meeting, 2014
- Fang Q. Hu, **Ibrahim Kocaogul** and Xiaodong Li, On the adjoint problem in duct acoustics and its solution by the Time Domain Wave Packet method, AIAA paper 2012-2247, 2012.

Experience and Awards

- Graduate Research Assistantship, Old Dominion University, Norfolk, VA (2011-2014)
- Graduate Teaching Assistantship, Old Dominion University, Norfolk, VA (2008-2011)
- Treasurer of the Math/Stat Club, Department of Mathematics and Statistics, Old Dominion University, Norfolk, VA (2011-2012)

Typeset using LaTeX.